Université catholique de Louvain
Secteur des Sciences et Technologies
Institut de Recherche en Mathtématique et Physique
Centre for Cosmology, Particle Physics and Phenomenology

The Matrix Element Method at the LHC: A Search for the Associated Production of Higgs and Z Bosons.

Doctoral dissertation presented by

Arnaud Pin

in fulfillment of the requirement for the degree of Doctor in Sciences

Jury de thes̀e:

Pr. Vincent Lemaître (*Advisor*)	UCL, Belgium
Pr. Jean-Marc Gérard (*Chairman*)	UCL, Belgium
Pr. Andrea Rizzi	Università di Pisa, Italy
Pr. Nick Van Remortel	U.A., Belgium
Pr. Fabio Maltoni	UCL, Belgium
Pr. Giacomo Bruno	UCL, Belgium

October 7th, 2013

Learn from yesterday, live for today, hope for tomorrow.
The important thing is to not stop questioning.

Albert Einstein

Remerciements

Cette recherche doctorale effectuée tout au long de ces cinq dernières années, et dont ce document est l'aboutissement, n'aurait pu être possible sans la collaboration de personnes extérieures et le soutien permanent de mon entourage. Je tiens à tous les remercier ici.

En premier lieu, je remercie mon promoteur, le Professeur Vincent Lemaître, de m'avoir donné l'opportunité de commencer et de mener à bien ce projet. Je remercie également les Professeurs Jean-Marc Gérard, Fabio Maltoni, Andrea Rizzi, Nick van Remortel et Giacomo Bruno pour avoir accepté de faire partie de mon jury de thèse.

Je tiens également à saluer les nombreuses personnes, expérimentateurs et théoriciens, avec lesquelles il m'a été donné l'opportunité de travailler durant ces cinq dernières années. Je tiens à remercier, entre autre Olivier Mattelaer et Pierre Artoisenet, les developpeurs de MadWeight. La collaboration avec Olivier m'a permis de me familiariser avec la méthode des éléments de matrices. Merci également à Andrea Giammanco et Julien Caudron avec lesquels j'ai commencé mes études sur la physique du quark top à CMS. Et enfin, je tiens particulièrement à remercier mes principaux collaborateurs durant ces trois dernières années, les membres du groupe llbb, Christophe, Roberto, Camille, Ludivine, Adrien, Jesus et Tristan notre organisateur de réunions H(b)(b).

Je ne peux les citer tous, mais en plus de mes collaborateurs, je tiens à remercier aussi tous les membres de CP3, pour l'atmosphère de travail conviviale et stimulante qu'ils contribuent à entretenir ainsi que pour tous les à-cotés.

Je tiens également à souligner l'important travail du secrétariat de CP3 qui nous rend les procédures administratives plus simples entre autre dans l'organisation de nos fréquents déplacements. Merci à Ginette, Carine, Luc et Christine.

De plus, ce travail a été rendu possible grâce au travail quotidien de l'équipe informatique qui maintient à disposition un outil performant. Merci à Pavel, Jerôme, Vincent et Juan pour le support qu'ils fournissent afin de résoudre nos problèmes toujours dans les délais les plus courts.

Et bien évidement, Merci à ma famille pour le soutien quotidien qu'elle m'a apporté tout au long de mes études et sans qui je n'aurais pu achever ce travail, cela a été une réelle source de motivation et je leur en suis extrêmement reconnaissant. La présence des amis, anciens colocataires et autres, a également été un appui conséquent et je les en remercie.

Contents

Appendix

Introduction

What is the smallest piece of matter? This is a question people have been asking since the time they first began to wonder about the structure and origins of the world around them. Over the past century, particle physicists have used tools of ever and ever more powerful to look deep into the very heart of matter in the continuing quest to find nature's basic building blocks and to discover the simple physical laws that make our universe more understandable. All these developments make what is called the Standard Model of particle physics. For the past 30 years, its predictions have matched with the experimental data like the confirmation of the existence of the weak currents at CERN and the discovery of the top quark in 1995 at the Tevatron. However, some questions are left opened like the explanation of the origin of the mass of particles or the mass hierarchy of the fermions, the asymmetry between matter and anti-matter. As far as the mass origin is concerned, the common consideration assumes a solution based on the Brout-Englert-Higgs mechanism developed in the 60's. It is based on the spontaneous symmetry breaking principle and it predicts the existence of an additional particle to the Standard Model, the so-called Higgs-boson.

When this thesis began, the Higgs Boson was the missing piece of the Standard Model of particle Physics. Experiments at the LEP or at the Tevatron did not find it but restricted the mass region of existence of such a particle. The Large Hadron Collider, LHC, at CERN have been designed with as one of its main purpose to prove the (non-)existence of a Higgs boson.

Since 2012 July, we are about to claim the presence of the missing Higgs boson. The Large Hadron Collider, LHC, at CERN allows physicist to discover a new resonance which is compatible with the Standard Model Higgs boson. The observation of this new particle in specific final state is not sufficient to claim that it is the Higgs boson. Precise measurement of the mass and other properties as the spin must be performed as well and all the theoretical predictions, about the coupling to the different particles have to be confirmed. Eventual observation of the Higgs boson in the various possible decay channel is necessary. This thesis will focus on one of them where the Higgs boson decays in pair of bottom quark. As this observation is very challenging an advance technique based on the Matrix Element method (developed at Tevatron for Top quark Physics) has been setup.

The first chapter introduces the motivations and the theoretical context of the Higgs boson search analysis presented in this thesis. It includes a discussion on the electroweak sector of the Standard model and the introduction to the Brout-Englert-Higgs mechanism that leads to the Higgs boson particle. The strong interaction will also be briefly reviewed and the experimental setup described. Then the analysis technique, the Matrix Element Method used all along this presentation is introduced as well.

The second chapter focus on top quark physics studies bases on the Matrix Element Method. Indeed, a preliminary top quark mass estimation performed with the first 36 pb^{-1} of 2010 CMS data is presented. The purpose of this analysis is to improved our expertise and to test the use of the method, at the LHC, before applying it to Higgs search. Then a second application for search for new physics for $t\bar{t}$ dileptonic processes based on the reconstruction of differential cross section performed with the Matrix Element method will be presented.

The third chapter presents a first search analysis based on the Matrix Element for Higgs boson decaying in $b\bar{b}$ analysis. Considering an associate production with a Z^0 boson decaying into two leptons. The methodology consists to use the Matrix Element method in association with another multivariate analysis. It is first validated in the context of a Standard Model analysis, the estimation of the $t\bar{t}$ background fraction in order to perform a $Z(ll)bb$ cross section measurement. The analysis procedure is then generalized in order to discriminate the Higgs signal and the different backgrounds. The multivariate analysis provides discriminant quantities that have been used to estimate a 95% upper limits on the ratio of Standard Model production of $Z(ll)Hb\bar{b}$.

Chapter 1

Physics at LHC.

Proton-proton collisions at high center of mass energy allow the production of rare processes such as the production of top quark or more recently the discovery of a new scalar particle with a mass of 126 GeV/c^2 which is compatible with the predicted Standard Model Higgs boson. The top quark was discovered and its properties already well measured at Tevatron [1, 2]. Although the higher luminosity and the higher center of mass energy reached at the LHC allow a high rate production of top quark. The top quark was re-discovered quickly at LHC either with the top anti-top quark pair production or with the single top production [3]. The high rate production allows precise measurements of this particle especially about its mass.

The concept design of the LHC machine contributed to the recent discovery of a Standard Model Higgs boson. According to the theoretical description [4] this new particle is produced according to a variety of processes and decays in several final state. The observation of each of these decay processes brings informations to confirm that this discovery is compatible with a Higgs boson. Among all of them, the channels in which the Higgs decays into a pair of b and anti-b quark are the most challenging due to the high level of processes with a similar final state.

This thesis will focus on the search for a Higgs boson decaying in a pair of b's and produced in association with a Z^0 boson decaying into two leptons. Experimentally it provides a final state composed of two b-quark, two leptons. It is similar to one of the decay mode of top quark pair production. The processes with a final state corresponding to this specific topology will be discussed in this presentation. However the production rate of processes with the same final state is large.

In order to overcome this difficulty, many analysis techniques can be used,i.e. cut and count analysis or more advanced multivariate shape analysis. All of these approaches assume a correct theoretical description either the predicted yields or the shape description of some kinematic variables. This work will focus on another technique using an analysis model dependent method that makes use of the maximal amount of information available for a specific process, considering the theoretical description in addition to the observation at detector level.

This first chapter introduces first the Large hadron collider and the Physics that occurs at high energy proton proton collisions and described by the Standard Model of particles Physics. Then it focus on the production and decay of an hypothetical light Higgs boson, the status of searches and measurement is briefly reviewed as well. Thereafter, as it is not the purpose of this thesis, motivations for top quark mass measurement are introduced. Indeed, a preliminary study presenting such measurement and done to improve our expertise in the Matrix Element method, will be discussed in the next of this work. The experimental set-up, the CMS experiment, and the analysis technique called Matrix element method [5] used all along this thesis will be introduced as well in this chapter.

1.1 The Large hadron Collider

The Large Hadron Collider (LHC) was built to study particle interactions at a new energy frontier. To do this a proton-proton collider has been chosen and it is running for physics since 2010. It is a 26.7 km circular collider, located approximately 100 meters under the border between France and Switzerland. The LHC strikes protons together at a center of mass energy of a few TeV. During the last campaign of run, the center of mass energy of the two proton beams was $\sqrt{s} = 8$ TeV. Although, this thesis presents analysis with the data recorded during the two first years of run (2010 and 2011) where $\sqrt{s}$ was at 7 TeV.

Such a high energy is needed to increase the production probability of the rare processes of interest and to perform analysis sensitive to them. For example, the previous hadron collider, the Tevatron located at Fermilab produced and discovered the top quark striking proton anti-proton at a center of mass energy of 1.96 TeV.

The Large Hadron Collider is the final piece of the CERN complex accelerator, illustrated in Fig. 1.1. The protons are extracted by ionization of hydrogen then accelerated by a linear accelerator (Linac 2). They are injected in the Proton Synchrotron Booster and then into the Proton synchrotron to get an energy around 26 GeV. Afterwards the beam is injected to the SPS which accelerates the proton up to an energy of 450 GeV. This beam is finally injected in the LHC.

The LHC is composed of resonant cavities (for the particles acceleration) and magnetic multipoles (for the beam curvature and collimation) producing magnetic field up to 8.3 Tesla. The two beams are, composed of bunches of protons, accelerated in opposite direction, in vacuum chamber at a low temperature (1.9 K), and they cross in four points where collisions occur.

The ring was equipped with four experimental interaction points where are located: The Compact Muon Solenoid (CMS) [6], the ATLAS [7] experiment, LHCb [8], and ALICE [9]. CMS and ATLAS are all purpose detectors designed for full luminosity. LHCB was built primarily for B-Physics aiming for a reduced peak luminosity. Lastly the LHC is also designed for operation with ion beams, ALICE was designed primarily for this LHC operating mode. ATLAS, LHCB and ALICE will not be discussed further in this thesis.

Figure 1.1 – Illustration of the full accelerator complex at CERN where the Large Hadron Collider, is the final component of the chain.

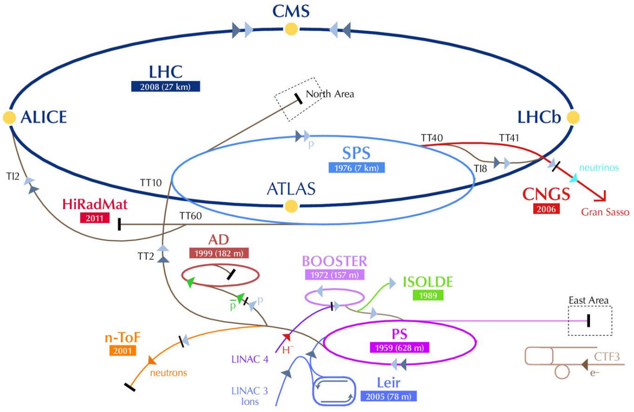

The most important parameter for a such collider is the luminosity, $\mathcal{L}$. Luminosity in high energy particle physics is a measure of the number of particles per unit area per unit time available for collisions. It depends on the beam properties and it is directly a function of the number of protons in each bunch (N_1, N_2), the collision frequency(f), and the effective area of the beams (σ_x, σ_y).

$$\mathcal{L} = f \frac{N_1 N_2}{4\pi\sigma_x\sigma_y}. \qquad (1.1)$$

The LHC delivered to the CMS experiment an integrated luminosity of 44.22 pb^{-1} during the 2010 data taking period and 6.13 fb^{-1} in 2011. The collisions occur as small crossing angle and this effect is neglected. The expected number of events for a specific process can be obtained by the product of the luminosity with the cross-section of the related process, $N = \mathcal{L} \times \sigma$.

A disadvantage of such a collider is due to large number of proton per bunch, a significant number of inelastic collisions are expected to occur at each crossing. This effect called pile-up is considered and is kept under control since it produces additional background in the detector. Therefore, to distinguish such events from one another, a high granularity is mandatory, which implies a large number of detector channels.

1.2 Standard model of particle physics

The high energy physics phenomena occurring at the LHC and currently observed are explained in a theoretical frame developed during the past 40 years. This description so-called, the Standard Model (SM) of particle physics [10] is the mathematical description, based on the quantum fields theory, of the elementary constituents of matter and their interactions via three among the four fundamental interactions.

The SM particle content consists of a total of 61 distinct elementary particles or anti-particles [11]. The anti-particles have opposite units of charge and lepton flavor number. There are 12 leptons, 36 quarks, 12 force mediators, and the theorized Higgs boson. The leptons listed in Table 1.1 come in three generations and consist of the familiar electron, its heavier relatives, the muon and the tau along with corresponding neutrinos and all of their anti-particles.

The quarks presented in Table 1.2 also come in three generations and a total of six varieties: up, down, charm, strange, top and bottom along with their antiparticles coming each in one of three colors (red, green, or blue). The up, charm and top quarks are said to be up type quarks and all have $\frac{2}{3}$ units of

Table 1.1 – List of the Standard Model lepton with their respective masses [11]. Three of them carry an electric charge while the three neutrinos are neutral particles.

	Mass $[MeV/c^2]$	electric charge
e	$0,511$	-1
ν_e	$< 3 \times 10^{-6}$	0
μ	$105,6$	-1
ν_μ	< 0.17	0
τ	1777	-1
ν_τ	< 15.5	0

electron charge, while the down, strange and bottom quarks are down type quarks and carry $\frac{-1}{3}$ units of electron charge.

Table 1.2 – List of the quarks in the Standard Model [11]. Three of them carry a positive electric charge of $+\frac{2}{3}$ while the other a negative charge of $-\frac{1}{3}$.

	Mass $(\times c^2)$	electric charge
up	$1.7 - 3.3$ MeV	2/3
down	$4.1 - 5.8$ MeV	-1/3
charm	1270 MeV	2/3
strange	101 MeV	-1/3
top	173.3 GeV	2/3
bottom	4.3 GeV	-1/3

Exchange of force mediator particles are responsible for the interactions between particles. These interactions are described by renormalizable gauge theories, the EM interaction is an abelian theory while the other two are Yang-Mills theories. The three interactions considered by the Standard Model of particle physics are :

The electromagnetism: Interaction acting between electrically charged particles. Charged particle interact together by the exchange of photon (γ) which is a bosonic particle. It's an infinite range interaction that implies a massless photon.

The weak interaction: Interaction describing the nuclear β decay. It is a limited range interaction due to the massive gauge bosons ($W^+W^-Z^0$) which are the mediators of the interaction.

The strong interaction: describing how quarks interact by exchange of massless gauge bosons, the gluons. Quarks are the basic building blocks of all the hadronic state as the protons (uud) or the neutrons (udd). Their cohesion is insured by the strong interactions. The corresponding mediator particles are 8 gluons, one with each color permutation.

At particle collider the rate of transition between an initial state, P_i defined by the incoming particles P_A and P_Bx, to an observed final state P_f composed of n particles is provided by the process cross section which is expressed as

$$d\sigma = (2\pi)^4\delta^4(P_f - P_i)\frac{1}{4\sqrt{(P_A.P_B)^2 - m_A^2 m_B^2}}|\mathcal{M}_{fi}|^2\prod_{i=1}^{n}\frac{d^3p_i}{(2\pi)^3 2E_i}. \quad (1.2)$$

In this equation, the term $|\mathcal{M}_{fi}|^2$ which is the square of the Feynman amplitude represents the probability density function of occurrence of a specific high energy process. In the following of this section, the strong interaction is first introduced then I focus on the he electroweak sector introducing the Higgs boson by the spontaneous symmetry breaking mechanism. I will also discuss the top quark physics, which is the heaviest particle in the standard model.

1.2.1 The strong interaction

The strong force is responsible for the interactions between colored particles, quarks and gluons and is modeled by the QCD (Quantum ChromoDynamic) theory [12]. This interaction is responsible for the nucleus binding of the atoms. The quantum number related to this interaction is the color which can be red, green, or blue. Free quarks have not been observed, indeed the theory of the strong interaction states that all particles in nature should be 'colorless'. Quarks then can combine in one of two ways to produce particles. Mixing these color states with their corresponding anti-color states ($q\bar{q}$), "white" particles are built. These combinations correspond to the Meson particles. Combinations of three quarks (qqq), one of each color, define the Baryons which include the neutron and the proton.

The strong interaction description is a renormalizable Yang-Mills theory based on a gauge group, which is in this case $SU(3)$. There are eights generators for this symmetry group, the 3×3 Gell-Mann matrices. These generators are associated to the massless gauge bosons that can mix the color, the gluons vector

Figure 1.2 – Representation of the different QCD coupling, between quarks and gluons and between gluons themselves.

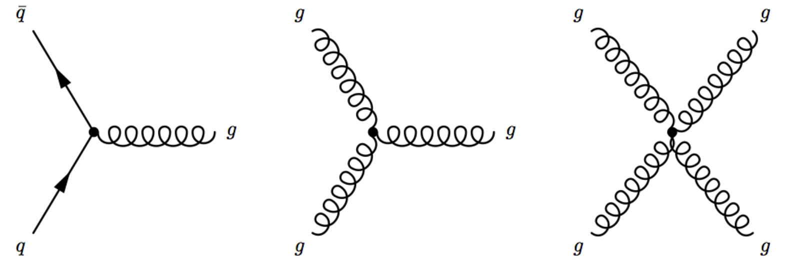

field G^a_μ. The quark flavor is not affected by these processes. The Feynman diagrams which illustrate the strong interaction are presented in Fig 1.2.

Compared to the other interactions, the strong force is relatively large but acts only at very short range 10^{-15} meter, that correspond approximately to the size of a nucleus.

The strong interaction coupling constant; α_s ranges over several orders of magnitude when moving from hard, i.e. large momentum transfer processes, to soft processes. The free parameter of QCD, Λ_{QCD} is defined as the energy scale (μ) at which the strong interaction cannot be described by a perturbative theory, its value is extracted to fit to experimental data and its value is $\Lambda_{QCD} \approx 200$ MeV.

At high energy, $\mu \gg \Lambda_{QCD}$, it is equivalent to short distance interactions, the quarks and gluons behave as free particles. This effect is known as “asymptotic freedom”. It allows treatment of QCD interactions in high energy physics using perturbative methods to calculate cross sections. It also provides an important physical feature preventing the unbinding of protons and neutrons that make up all the matter around us.

By opposition the coupling is stronger at lower energy, it corresponds to large distance interactions, where only ’colorless’ bound states of quarks and gluons can be observed. This phenomena is called the confinement.

When there is a transfer of energy to a $q_i\bar{q}_i$ system, for example by a collision, their distance increase but this makes their coupling stronger, and therefore the energy density of the vacuum between them increases, and if this reaches the point where a new $q_j\bar{q}_j$ pair appears, one can get the formation of $q_i\bar{q}_j$ and $q_j\bar{q}_i$

mesons. For high energy process, when the energy of quarks, produced by this cascade phenomena, are low enough, the confinement implies the hadronization effect. The shower of baryons and mesons produces what is called a hadronic jet.

The factorization principle [13] at hadron collider is illustrated in Fig. 1.3, that shows the evolution from the free parton involved in the hard scattering to the hadronization phenomena at lower energy scale. It also shows that the other parton of the colliding protons will interact, this is called the multiple parton interaction (MPI).

Figure 1.3 – Illustration of the QCD factorization principle [13]. From the asymptotic freedon of the proton constituents (at high energy), their hard interaction (red Dot) to the confinement that produce hadronization (green dot) of colored particles (at lower energy). It also shows that other partons from the same or other proton in the bunch can interact (blue point).

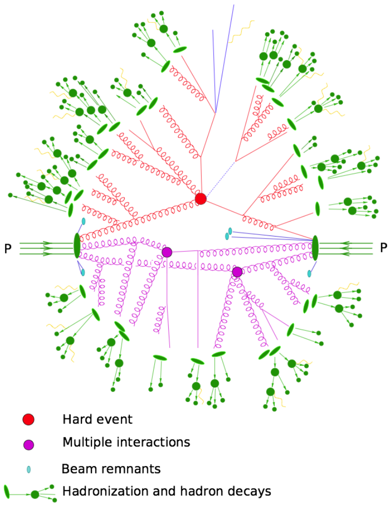

In the parton model approximation, the process can be factorized between the hard process and the free evolution of the partons. At hadron collider it is the partons, inside the proton, that interact and the cross section for process initiated by two hadrons with four momenta p_1 and p_2 is conveniently described by Eq. 1.3,

$$d\sigma_{p_1p_2} = \sum_{ij} \int dq_1 dq_2 f(q_1, \mu_F^2) f(q_2, \mu_F^2) \sigma_(ij)(p_1, p_2, \alpha_s(\mu_F^2), \frac{Q^2}{\mu_F^2}) \quad (1.3)$$

where Q is the energy scale of the hard scattering, typically m_Z for Z boson production. $\sigma_{(ij)}$ represents the cross section for hard scattering of partons i and j that will be calculated by perturbative QCD. The arbitrary parameter μ_F represent the factorization scale [14] that separated the long distance interaction and the short distance one. This scale is at the same order as the hard scale Q. The sum is performed on all the possible parton combinations.

In this framework, partons carry a fraction of the total longitudinal momentum of the proton, described by $f(q_i)$. The parton distribution function (*pdf*) [15], decribes the probability that a parton carries a momentum fraction q_i. These *pdf*, for quarks and gluons, have been estimated by fitting in particular the HERA [16] and [17] and TEVATRON [18] and [19] data. The `CTEQ6L1` *pdf* [20] are represented in Fig. 1.4 at the electroweak scale.

Figure 1.4 – Overview of the CTEQ6M parton distribution functions at Q = 100 GeV [20]

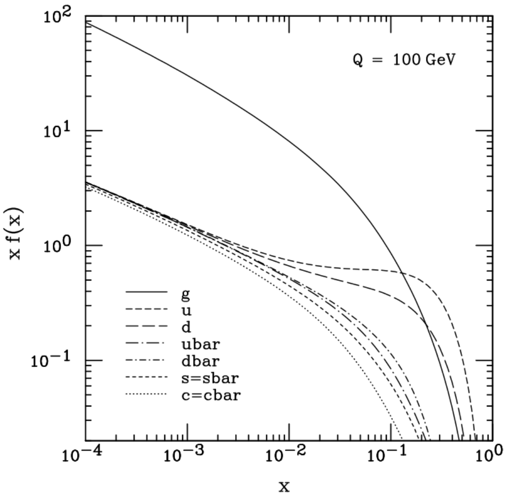

The production cross section calculation as expressed by Eq 1.3, the freedom due to the *pdf* are taken into account by integrating them for both incoming parton, as illustrated by the $f(q_i)$ terms.

1.2.2 Electroweak sector

In 1961 Glashow, Weinberg and Salam (GWS) [21, 22, 23] proposed an unified theory of electromagnetism and weak interactions, based on the fact that the coupling constant "g" to the weak boson Z^0 is similar in magnitude to the electromagnetic coupling "e". It leads to the possibility that these two interactions can be unified with a same coupling strength. The so-called electroweak theory is based on the existence of charged and neutral intermediate vector bosons. The discovery of neutral-current, at CERN in 1973 by an experiment using the large bubble chamber "Gargamelle" [24], was important since providing clear evidence in favor of this unified model.

On the one hand there is the electromagnetic interaction between charged particle that is well describe by the QED theory. It is a gauge theory based on the local invariance under the $U(1)_Q$ transformation. The group generator A_μ is associated with the vector boson of the interaction, the photon.

On the other hand the non observation of right-handed neutrino leads to a weak interaction theory that does not respect the parity. The weak interaction description implies both charged and neutral current interactions. The coupling to the fermions are restricted as follow: on the one hand the $W^\pm$ bosons couple exclusively to the left-handed fermions, whereas, on the other hand, the Z^0 bosons couple to both left and right handed fermions. The weak interaction description is then based on the $SU(2)_L$ symmetry group. It suggests to organize the left-handed fermions as weak isospin doublet, q_L and l_L and right-handed fermions as weak isospin singlet, d_R and e_R.

$$q'_L = \begin{pmatrix} u'_L \\ d'_L \end{pmatrix}, \qquad u'_R, \qquad d'_R, \qquad l_L = \begin{pmatrix} \nu_L \\ e_L \end{pmatrix}, \qquad e_R,$$

The Lagrangian density of the electroweak sector is build to be invariant under transformations of the gauge group $SU(2)_L \times U(1)_Y$, where $U(1)_Y$ represents the QED component.This structure goes along with four massless gauge bosons associated to the group generators. Three coming from $SU(2)_L$, the W^i_μ which are related to the Pauli matrices ($T^i \equiv \frac{\tau^i}{2}$) and the one from $U(1)$, called B_μ, is related to the hypercharge Y defined as combination of the electric charge (involved in QED) and the weak isospin (involved in weak interaction). The associated fields tensor are then defined as

$$B_{\mu\nu} = \partial_\mu B_\nu - \partial_\nu B_\mu \tag{1.4}$$

$$W^i_{\mu\nu} = \partial_\mu W^i_\nu - \partial_\nu W^i_\mu + g\epsilon_{ijk} W^j_\nu W^k_\nu \tag{1.5}$$

For such a group the covariant derivatives required to insure the local gauge invariance is given by

$$D_\mu = \partial^\mu - igT^i W^\mu_i - ig'\frac{Y}{2}B_\mu \tag{1.6}$$

where g and g' are the coupling constants for the weak isospin and hypercharge currents respectively . The corresponding gauge Lagrangian ($\mathcal{L}_\mathcal{G}$) reads:

$$\mathcal{L}_\mathcal{G} = -\frac{1}{4}\sum_{i=1}^{3} W^i_{\mu\nu} W^{i\mu\nu} - \frac{1}{4} B_{\mu\nu} B^{\mu\nu} \tag{1.7}$$

Moving to the basis of the physical fields, the vector bosons $W^\pm, Z^0, \gamma$ can be expressed from the four gauge fields introduced in this description. The W^1_μ and W^2_μ fields are electrically charged and according to the group algebra the $W^\pm$ fields can be defined as

$$W^+ = \frac{W^1_\mu - iW^2_\mu}{\sqrt{2}} \quad \text{and} \quad W^- = \frac{W^1_\mu + iW^2_\mu}{\sqrt{2}} \tag{1.8}$$

These fields are responsible of the charged current interactions that mix up and down fermion type. While the two other fields, W^3_μ and B_μ do not. Still, the charged and neutral currents described by the GWS theory require to introduce a new physical observable. This free parameter is the mixing angle called the weak angle θ_W which enters in the definitions of the physical neutral currents Z^0 and A (photon) as

$$A_\mu = -sin\theta_W W^3_\mu + cos\theta_W B_\mu \tag{1.9}$$
$$Z_\mu = cos\theta_W W^3_\mu + sin\theta_W B_\mu \tag{1.10}$$

The g and g' coupling constant present in the Eq. 1.6 are related to the electromagnetic coupling constant e as $e = g \sin\theta_W = g' \cos\theta_W$ with $\cos\theta_W = \frac{M_W}{M_Z}$.

The short range nature of the weak force led to the prediction of the masses of the $(W^+; W^-; Z^0)$ bosons mediating the weak interaction which required to include an additional theoretical principle. This principle has been introduced by Brout-Englert and Higgs through the spontaneous symmetry breaking [25] of the electroweak gauge group $SU(2)_L \times U(1)_Y$ to the remaining unbroken abelian group $U(1)_Q$ of electromagnetism.

This theory has been confirmed with the discovery of the vector boson $W^\pm$ and Z^0 in 1983 at UA1 and UA2 experiments [26] [27]. However, this description is not complete since nor gauge fields neither matter fields can have mass. No mass terms naturally appear in the Lagrangian. That implies an infinite range interaction which is in contradiction with the observations. Moreover, we know that some fermions are massive too. Including a mass term such as $m^2 W_\mu W^\mu$ would violate the gauge invariance. Since mass term mixes left and right-handed fermions, and since these have different gauge quantum numbers, the introduction of fermionic mass term, $m\Psi\bar{\Psi} = m(\bar{\Psi}_L\Psi_R + \bar{\Psi}_R\Psi_L)$, is not gauge invariant as well. A solution to that problem is the Brout-Englert-Higgs mechanism discussed in the next section.

1.2.3 The Brout-Englert-Higgs mechanism

In the SM the $W^\pm$ and Z^0 bosons acquire mass via a broken symmetry called the Brout, Englert and Higgs Mechanism [28] [29] [30] which as a consequence predicts an additional massive scalar particle called the Higgs boson. In addition to giving mass to the W± and Z0 bosons the mass of the fermions can be explained by their coupling to the Higgs field. This section will present the mechanism and will then focus on the production mode of this new boson at LHC.

The main idea is that an additional scalar field is introduced in the theory in such a way that the Lagrangian still respects the $SU(2)_L \times U(1)_Y$ symmetry, but the vacuum state does not.

Starting from a gauge invariant theory, the Brout-Englert-Higgs mechanism allows to have massive gauge bosons and fermions via spontaneously breaking of the gauge symmetry. It implies to include a complex scalar field which is an $SU(2)_L$ doublet. This new field parametrized as

$$\Phi = \frac{1}{\sqrt{2}} \begin{pmatrix} \Phi_1 + i\Phi_2 \\ \Phi_3 + i\Phi_4 \end{pmatrix}, \tag{1.11}$$

$$\tag{1.12}$$

has four degrees of freedom. The corresponding Lagrangian is written as

$$\mathcal{L}_S = (D_\mu \Phi)^\dagger (D^\mu \Phi) - V(\Phi^\dagger \Phi), \tag{1.13}$$

$$V(\Phi) = \mu^2 \Phi^\dagger \Phi + \frac{1}{2}\lambda(\Phi^\dagger \Phi)^2 \tag{1.14}$$

where $V(\Phi)$ represents the Higgs potential. The presence of a minimum requires $\lambda > 0$ while the parameter μ is choosen such that the field Φ acquires a vacuum expectation value different from zero, $< \Phi >= v \equiv \frac{\mu}{\sqrt{(\lambda}}$. The projection in 1-dimensional space of this potential is illustrated in Fig. 1.5

Figure 1.5 – Representation of the shape for a 1-D projection of the Higgs potential where $\mu^2 < 0$.

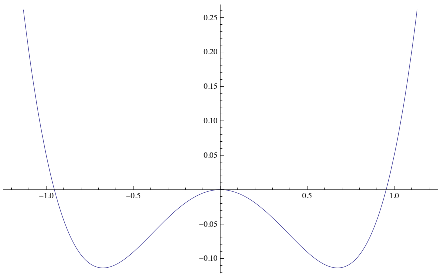

There is a gauge transformation such that the field Φ components in the vacuum state are expressed as $\Phi_1 = \Phi_2 = \Phi_4 = 0$ and the $\Phi_3 = v$.

This particular gauge choice breaks the $SU(2) \times U(1)_Y$ gauge symmetry to the $U(1)_{em}$ that ensures a massless gauge boson (γ) for the electromagnetism.

According to perturbative theory, the variations along the Φ_3 component called the excited state of Φ, generate the Higgs boson field ($h(x)$),

$$\Phi = \begin{pmatrix} 0 \\ (v + h(x))/\sqrt{2} \end{pmatrix} \tag{1.15}$$

The substitution of the scalar field ϕ, in the Eq. 1.14, by its expression (Eq. 1.15), makes appear an explicit mass term for the Higgs field, $m_h^2 = 2v^2\lambda$ which is expressed as

$$V = \frac{1}{2}(2\lambda v^2)h^2 + \lambda v h^3 + \frac{1}{4}\lambda h^4 \tag{1.16}$$

Gauge boson masses: The interaction between the scalar field Φ and the gauge boson fields of electroweak theory, makes appear mass terms. Looking at Eq. 1.13 and using the covariant derivative defined at Eq. 1.6, it turns out that the vacuum expectation values of Φ provides masses to the gauge bosons following Eq. 1.17.

$$m_W^2 W_\mu^+ W^{+\mu} + \frac{1}{2}(m_Z^2 Z_\mu Z^\mu) \quad \text{where:} \tag{1.17}$$

$$m_W^2 = \frac{1}{4}g^2v^2 \ , \ m_Z^2 = \tfrac{1}{4}(g^2 + g'^2)v^2. \tag{1.18}$$

while the photon remains massless assuming that the weak mixing angle satisfy $\tan\theta_W = \frac{g'}{g}$. Experimentally the measurements of the vector boson mass provide $m_{W^\pm} = 80.04$ GeV/c^2 and $m_{Z^0} = 91.017$ GeV/c^2 [11].

The Yukawa sector

The presence of the Higgs field in the SM theory allows also massive fermions. Interaction terms between the Higgs field and the fermions, the so called Yukawa interaction term may be added to the Lagrangian:

$$\mathcal{L}_{Yukawa} = -\lambda_\psi[\bar{\psi}_L \Phi \psi_R + \bar{\psi}_R \tilde{\Phi} \psi_L], \tag{1.19}$$

where $\tilde{\Phi} = i\tau_2 \Phi$. The consequence is the apparition of mass term for the fermions.

Quark masses: The Yukawa Lagrangian Eq. (1.19) is expressed in term of the flavor eigenstate (q'_L, u'_R and d'_R) as

$$\mathcal{L}^{quark}_{Yukawa} = Y^d_{ij} \bar{d_{Li}}' \Phi d'_{Rj} + Y^u_{ij} \bar{u_{Li}}' \Phi u'_{Rj} + h.c. \tag{1.20}$$

where Y^d_{ij} and Y^u_{ij} are the Yukawa matrices, for up and down quark type respectively. These are arbitrary matrices which mix flavor eigenstates i and j. It implies that the flavor eigenstates are not necessarily the same as mass eigenstates (q_L, u_R and d_R). Substituting Φ by the vacuum state makes the following mass matrices appear for the flavor eigenstates,

$$M^u_{ij} = Y^u_{ij} \frac{v}{\sqrt{2}} \quad \text{and} \quad M^d_{ij} = Y^d_{ij} \frac{v}{\sqrt{2}}, \tag{1.21}$$

which are not automatically diagonal. These mass matrices are diagonalized by using unitarity transformations, $V^u_{L/R}$ and $V^d_{L/R}$ which are respectively acting on up or down, left-handed or right handed quark type respectively. It allows to change from the flavor eigenstate basis to the mass eigenstate basis. In this latter one, the diagonal mass matrices for up and dow quark are expressed as

$$\text{for type up:} \quad M^u = V^u_L Y^u \tfrac{v}{\sqrt{2}} V^{u\dagger}_R \tag{1.22}$$

$$\text{for type down:} \quad M^d = V^d_L Y^d \tfrac{v}{\sqrt{2}} V^{d\dagger}_R . \tag{1.23}$$

According to these transformations, the charge current interactions will involve a combination of matrices ($V^d_L V^{u\dagger}_L$). By convention, the flavor eigenstate and the mass eigenstate are choosen to be the same for the up-type ($V^u_L = V^u_R = \mathbb{I}$).

The down type quarks are therefore rotated from the flavor basis to the mass basis by the Cabbibo-Kobayashi-Maskawa (CKM) matrix written as

$$\begin{pmatrix} d' \\ s' \\ b' \end{pmatrix} = \begin{pmatrix} V_{ud} & V_{us} & V_{ub} \\ V_{cd} & V_{cs} & V_{cb} \\ V_{td} & V_{ts} & V_{tb} \end{pmatrix} \cdot \begin{pmatrix} d \\ s \\ b \end{pmatrix} \tag{1.24}$$

Because of this rotation, the CKM matrix elements appear in the Lagrangian expression of the charged current interaction with the quark sector. This Lagrangian is then written as

$$\mathcal{L}_{cc}^{int} = -\frac{g}{\sqrt{2}} V_{ij} \bar{u}_{Li} \gamma^{\mu} d_{Lj} W_{\mu}^{+} + h.c., \tag{1.25}$$

where V_{ij} represents the CKM matrix element of the transition between an up-type quark of flavor i and a down-type quark of flavor j.

Lepton mass: Concerning the leptons, substituting the field ϕ by its vacuum state, in Yukawa Lagrangian (Eq.1.19), makes appear a mass term associated to the leptons, Eq. 1.26. It shows also that the coupling between the leptons and the Higgs boson is proportional to the lepton mass.

$$m_e = \frac{v\lambda_e}{\sqrt{2}} \tag{1.26}$$

The same procedure as for the quark sector can be used. It gives mass to the down type fermions while the neutrinos remain massless. That is in agreement with the non observation of right handed neutrino.

To summarize, GWS with the Brout-Englert-Higgs mechanism provides a model that contains two charged gauge bosons $W^{\pm}$ degenerated in mass. It contains also two neutral gauge boson, one massless coupling only to the charge particle, the photon γ and a massive one Z^0 . However, the striking point is that the introduction of a scalar field with a non vanishing vacuum expectation value that spontaneously breaks the gauge symmetry implies a new massive and neutral particle, the Higgs boson.

1.2.4 Production and decay of a Standard Model Higgs boson.

There are several Standard Model Higgs production processes which occur at the LHC. The dominating Higgs production mode at high energy colliders is through gluon-gluon fusion, $gg \rightarrow H + X$. Following gluon-gluon fusion the other production modes include vector boson fusion, $q\bar{q} \rightarrow qqH + X$, and associated production, $q\bar{q} \rightarrow VH + X$ where V is a $W^{\pm}$ or Z^0 boson. Lastly with a greatly reduced production rate you have a Higgs produced in association with a top quark pair.

Since the Higgs boson couples to massive particle, the gluon-gluon production mode is achieved through top quark loop. This loop dominates because the coupling between top quark and Higgs is dominating. The evolution of the cross section with respect to the Higgs boson mass has been calculated at NLO in electroweak and in NNLO in QCD, for the the various production modes. It is shown in Fig 1.6(a) for proton-proton collision with a center of mass energy of 7 TeV.

The Vector boson fusion (VBF) production is the second most common production mode at the LHC. It is achieved through a pair of quarks radiating a $W^{\pm}$ or Z^0 boson which combine to produce a Higgs Boson.

Figure 1.6 – a- Evolution of the standard Higgs boson cross section of production with respect to the Higgs mass. This is for proton-proton collision at $\sqrt{s} = 7$ TeV at LHC. b- Evolution of the standard Higgs boson cross section of production with respect to the Higgs mass.

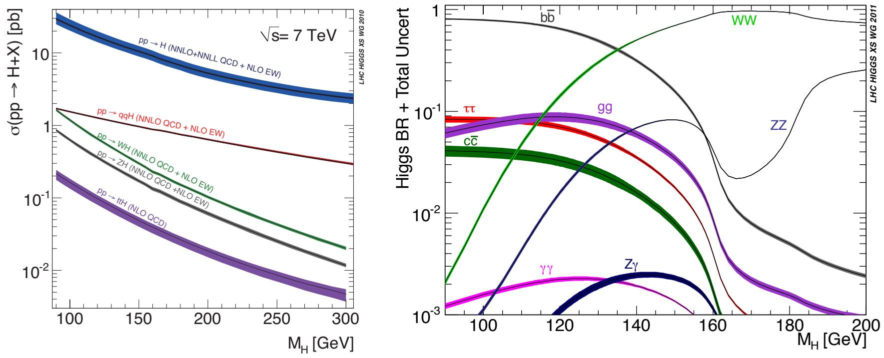

(a) (b)

Another channel is the associated production (VH) mode, it is the smallest production mode at the LHC. The Higgs is produced when it is radiated from a $W^{\pm}/Z^{0}$ boson. VH events have a remaining $W^{\pm}/Z^{0}$ in the event.

The Higgs boson is not directly observable in a detector, it decays instantaneously according to several possibilities. The branching ratios for the different decay channels of a Standard Model Higgs boson depend strongly on the Higgs mass. For a Higgs boson with a relatively low mass, below 135 GeV, decays to fermions dominate, specifically to $b\bar{b}$ and $\tau\tau$. At higher mass, the Higgs decays to WW and ZZ dominate. The branching ratio for the Higgs boson decay in the different channels is displayed in Fig 1.6(b) as a function of its mass.

In the low mass region the decays to leptons and quarks are involved in the majority of Higgs decays. Firstly $b\bar{b}$ comes with a branching ratio starting at 80% at 90 GeV and then slowly going down as mass increases and WW and ZZ decays are increasing. After $b\bar{b}$ you have the $\tau\tau$ decays at about 1 order of magnitude lower.

Searches at the LHC are particularly reliant on ZZ and $\gamma\gamma$ due to the good separation of the signal from the irreducible backgrounds in these channels. Concerning the $\gamma\gamma$ and the ZZ search channels, it is possible to reconstruct the full energy of the decay products resulting in a high resolution mass peak compared to backgrounds that are non-resonant. However, the $b\bar{b}$ and $\tau\tau$ modes remain important channels for verifying the coupling to leptons. They have much larger backgrounds but also have a considerably higher cross section times branching ratio.

During the past, the experimental non observation of a Standard Model Higgs bosons allowed to restrict the phase space region allowed for such a particle. At the LEP collider (Large Electron Positron collider) searches for the Higgs boson have been done by the OPAL, L3, DELPHI, and ALEPH collaborations. The main production mode came with a Higgs boson in association with a Z boson. The search channels included; $H \to b\bar{b} + Z \to q\bar{q}/ll/\nu\bar{\nu}$ and $H \to \tau\tau + Z \to q\bar{q}$. A combination was done from all experiments resulting in a Standard Model Higgs excluded [31] for masses $m_H < 114.4$ GeV/c^2 with 95% confidence level.

Direct searches have also been performed at Tevatron and exclude at 95% confidence level the presence of a Standard Model Higgs boson in the two mass ranges $100 < M_H < 103$ GeV and $147 < M_H < 180$ GeV [32].

In addition to these direct constraints, a fit of the Standard Model parameters, based on the electroweak precision measurements [33], implies a Higgs boson mass lighter than 152 GeV/c^2.

In summer 2012, both ATLAS and CMS collaboration announced the observation of a new resonance compatible with the Standard Model Higgs boson [34]. The discovery has been claimed combining results of the searches performed in the different decay channel. That includes results from the $H \to \gamma\gamma$, $H \to W^+W^-$, $H \to ZZ$, $H \to \tau\tau$, and $H \to b\bar{b}$, analysis. The most significant contributions among these analysis come from the two decay modes with the best mass resolution, the $\gamma\gamma$ and $ZZ \to 4$ leptons decay channels. Indeed an excess of events is observed in the diphoton and in the four leptons invariant mass spectrum as illustrated in Fig 1.7(a) and in Fig 1.7(b) respectively.

Figure 1.7 – Observation of a new boson by the CMS experiment. (a) Di-Photon invariant mass distribution the bump in the distribution at 125 GeV indicates the presence of a new particle, (b) 4 lepton invariant mass from the ZZ search channel the peak of events at 125 GeV represents a new particle. [35]

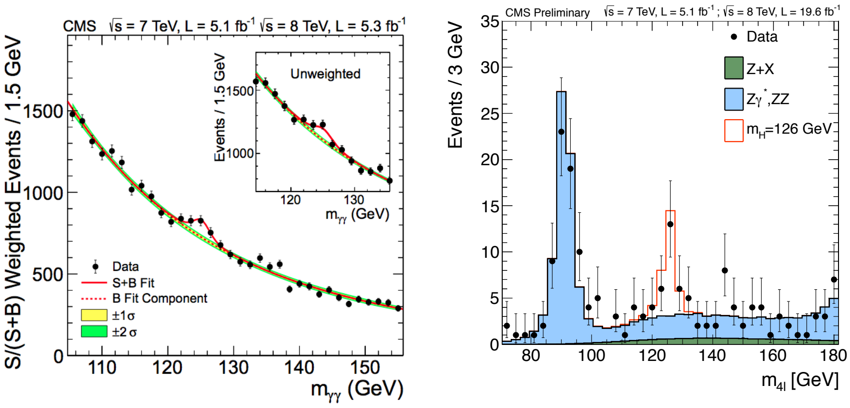

(a) (b)

Studies measuring some properties of the new resonance, as its mass or its parity, have been performed. Considering the $H \to ZZ \to 4$ leptons (electron or muon) decay channel, the CMS collaboration measures a mass of 126.2 ± 0.6 (stat) ± 0.2 (syst) GeV$/c^2$ and shows that the spin parity of this new particle is consistent with a pure scalar hypothesis [36].

The observation of Standard Model Higgs boson in the mass region around 126 GeV$/c^2$ is very challenging at hadron colliders. At such a mass value, the dominant decay channel is the $b\bar{b}$ pair production as shown in Fig 1.6(b), indeed the $b\bar{b}$ pair production constitutes the highest massive state among those kinematically allowed, while WW, ZZ and $t\bar{t}$ cannot be produced onshell by the decay of a so light particle. However, considering the gluon-fusion production mode, the QCD background is so huge implying no hope to see the $H \rightarrow b\bar{b}$ signal.

It motivates to focus on the associated production of standard model Higgs with a vector boson Z^0 or $W^{\pm}$. Among the latter two options, the case of the associated production with a Z^0 boson is the one studied in this thesis, while the CMS collaboration considers five different channels: $W_{l\nu}H$, $Z_{ll}H$, and $Z_{\nu\nu}H$). The search analysis, for these five particular channels, performed by the CMS collaboration measures an upper limit at 95% confidence level of 1.89 times the standard model prediction for a Higgs boson mass of 125 GeV while the expected limit is 0.95 [37].

The process of interest in this thesis is represented at the leading order by the $Z(ll)Hb\bar{b}$ diagram in Fig 1.8. The total cross section has been computed at NLO for the electroweak accuracy and at NNLO for the QCD accuracy. In the hypothesis of a Higgs boson with a mass of 125 GeV, proton proton collisions at $\sqrt{s} = 7$ TeV lead to a total cross section of 0.3158 pb.

Figure 1.8 – Leading order diagram illustrating at hadron collider the associated production of Higgs boson decaying in $b\bar{b}$ with a Z^0 boson decaying into two leptons.

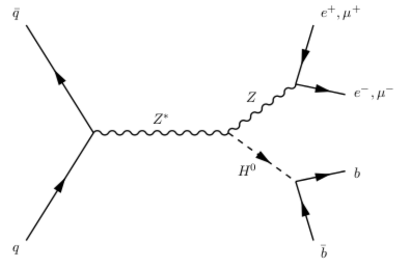

Fig. 1.9(a) shows the common signal strength (σ/σ_{SM}) values obtained in different sub-combinations of search channels for $m_H = 125.7$ GeV, organized by decay mode. The plot shows a satisfactory level of compatibility between all the channels contributing to the combination. However it also shows that the decay channel to vector boson has a higher sensitivity than analysis looking for Higgs decaying to fermions.

Studies looking for $Z(ll)Hb\bar{b}$, performed at the LHC by ATLAS and CMS as well, are interesting because this process involves the coupling between the fermion and the Higgs boson. Indeed the measurement of $H \rightarrow b\bar{b}$ will be the first direct test on the coupling between the Higgs field and the quark sector. Up to now, these couplings have only been tested through loop interactions which allow the gluon fusion production. The Standard Model predicted couplings [38] have already beeen tested as illustrated in Fig. 1.9(b). The consistency of the couplings of the observed boson with those predicted for the SM Higgs boson is tested in various ways, and no significant deviations are found, so far.

Figure 1.9 – (a): Values of production cross section times the relevant branching fractions σ/σ_{SM} for the combination (solid vertical line). The vertical band shows the overall uncertainty. The horizontal bars indicate the ±1 standard deviation uncertainties for the individual modes. [39]. - (b) Fits for the deviation to the Standard Model prediction of the coupling between Higgs boson and fermions/vector bosons. For the fermions it is the values of the fitted Yukawa couplings while for vector bosons it is the square-root of the coupling divided by twice the vacuum expectation value [39].

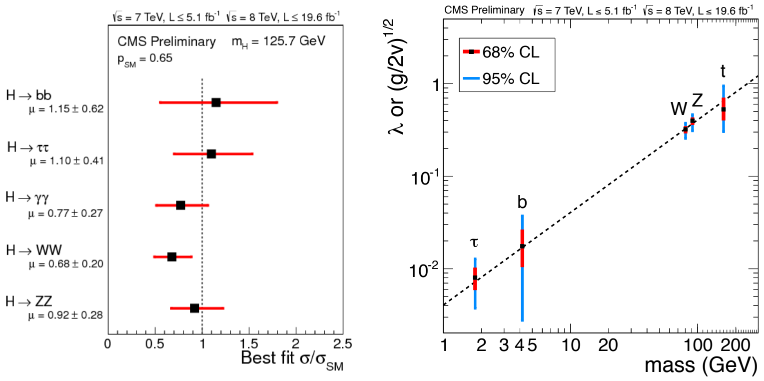

(a) (b)

The search for associated production of Higgs boson with a vector boson is not the only study looking for evidences of the new particle decay in $b\bar{b}$. Indeed, there are also studies performed by CMS and searching for Standard Model Higgs boson produced in association with a $t\bar{t}$ pair or produced by vector boson fusion. In these two analysis the observed upper limits are 3.6 and 5.2 while the expected limit are 3.0 and 5.8 times the standard model prediction [40] and [41] respectively.

1.2.5 Top quark Physics

The top quark is the heaviest elementary particle of the Standard Model of particle Physics, in the theoretical description it is the $SU(2)$ partner of the b quark. Its discovery, at Tevatron, in 1995 [42][43] by both CDF and D0 experiment completes the classification of the fermions in three families.

Physics of the top quark involves both strong and electroweak interactions, indeed, the production of top quark pair is described by QCD processes while its decay and the single top production are driven by electroweak phenomena. At hadron collider, the top quark production is dominated by the top anti-top quark ($t\bar{t}$) pair creation, either by quark anti-quark annihilation or by gluon fusion. These processes are illustrated in Fig. 1.10 at leading order. At the LHC, the dominant production mode is the gluon fusion, approximately 90%.

Figure 1.10 – Leading order diagram illustrating at hadron collider the production of top quark pairs either by $q\bar{q}$ (10%) or by gluon fusion (90%).

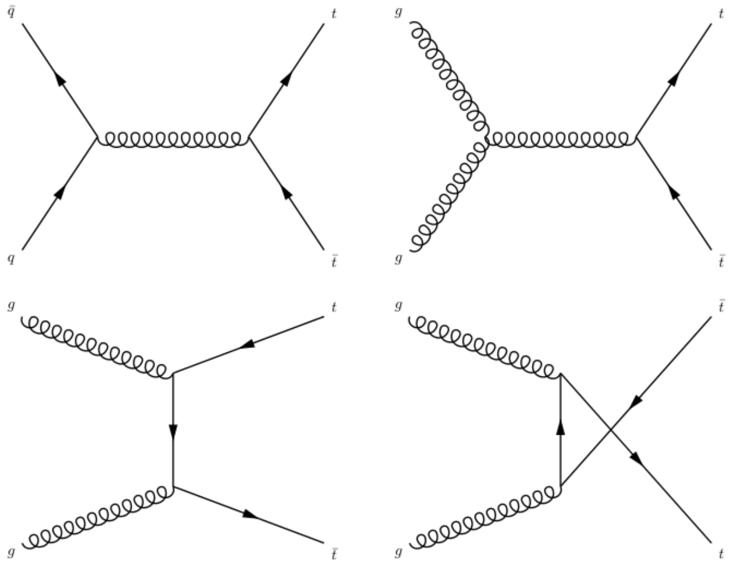

The $t\bar{t}$ production cross section is theoretically obtained by perturbative QCD calculation. This measurement at LHC, for proton proton collision with a center of mass energy of 7 TeV [44], combines CMS and ATLAS results and measure a production cross section of 173.3 ± 10.1 pb

The top quark decay is driven by the weak interaction which does not conserve the flavor. The decay coupling involved CKM matrix element as illustrated by Eq. 1.27. The main the decay mode is almost exclusively $t \to Wb$, as the CKM matrix element V_{tb} is theoretically close to 1. This is confirmed by CMS measurement of the branching ration of $R = B(t \to Wb)/B(t \to Wq)$ [45] which provides $R = 0.98 \pm 0.04$ and is consistent with the Standard Model prediction.

$$-i\frac{g}{\sqrt{2}}V_{tb}\gamma^{\mu}\frac{1}{2}(i-\gamma^{5}) \tag{1.27}$$

Concerning the $t\bar{t}$ processes, the branching ratios (BR) of the different decay processes are proportional to the product of the related BR of the W boson decay. This vector boson has nine possible decay modes: two quarks with 3 colors provide six of them and the others are due to the decay in lepton pairs for the three families. Because of that, the $t\bar{t}$ decay processes lead to three categories of final states which are:

The fully hadronic: Both W decay hadronically. This decay mode represents the highest branching ratio ($\approx 45\%$). However, the main difficulty is the large amount of background from high multiplicity QCD process.

The lepton + jet: One of the W decay hadronically while the other decay leptonically. One missing particle appears in the final state. The branching ratio represents $\approx 30\%$. The amount of background is still more important than for the dilpetonic channel.

The dileptonic: It's a symmetric decay chain terminating with two quarks and two $W^{(\pm)}$ boson where both of them leptonically. These boson decays provide two charged leptons, two neutrinos. The branching ratio is smaller than the two other decay modes $\approx 5\%$. Due to the presence of two neutrinos this decay channel is very challenging to perform precision measurement despite the fact that backgrounds are limited.

The $t\bar{t}$ process decaying fully leptonically constitutes the most challenging channel to perform a top quark mass measurement due to the presence of two neutrinos in the two branches of the process. The full decay is represented in 1.11.

The top-quark mass (m_{top}) is an essential parameter of the standard model. It affects predictions of SM observables via radiative corrections. A precise

Figure 1.11 – Diagram illustrating the top decay $t \to wb$ according to the coupling 1.27.

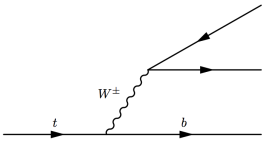

measurement of the top quark mass is one of the most important inputs to the global electroweak fits [46] [47] which provide constraints on the properties of hypothetical particles, including the Higgs boson. Precise measurement of the top quark mass has been used to put stronger constraint on the Standard Model Higgs mass which also depends on top mass in the corrections terms. Now with the observation of the Higgs bosons the direct measurement of the three masses (t, W and H) tests on the consistency of the SM can be performed. The Fig. 1.12 illustrates the constraints on the Standard Model by the top quark mass and the Higgs boson mass direct measurement [46].

Figure 1.12 – The 68% confidence level contour in m_{top} and m_{Higgs} for the fit to all data except the direct measurement of m_{top}, indicated by the shaded horizontal band of ±1 sigma width. The vertical bands show the 95% CL exclusion ranges on m_{Higgs} from the direct searches. [46].

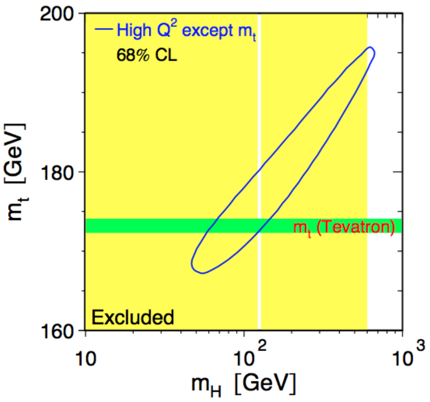

The quark masses are complicated to measure given that quarks are a colored particles. Confinement in QCD implies that there are no asymptotic states. However the top quark has the property to decay before hadronizing ($\Gamma_{top} \gg \Lambda_{QCD}$). Due to this particularity, the pole mass of the top quark can be measured directly. The pole mass represents the real part of the propagator: $\sqrt{p^2} = m_{pole} - \frac{i}{2}\Gamma$.

The top quark mass measurement performed by the CMS collaboration is $173.49 \pm 0.43_{(stat+JES)} \pm 0.98_{(syst)}$ GeV/c^2 and has been achieved using a kinematical fit method [48].A study of the difference between M_t and $M_{\bar{t}}$ has also been performed by CMS collaboration which is
$\Delta(M_{\bar{t}}, M_t) 272 \pm 196$(stat) ±122 (syst) MeV [49].

However, the Tevatron combined top mass measurement is still the most accurate value of 173.2 ± 0.87 GeV/c^2 [50].

1.3 The compact muon solenoid

The Compact Muon solenoid detector (CMS) [6] is one among the four experiment at the LHC. It is a cylindrical general purpose detector of 21.5 meters long and 15 meters of diameters. It is the heaviest detector with a weight of 12500 tons. The detector is centered on one of the four interaction point of the LHC. Some of the main goals of the CMS experiment are the observation of the Higgs boson and the measurements of its properties.

In order to identify the position and the direction of each particle in the detector, a specific coordinate system is defined as follow:

- The cartesian description is such as the Y axis is oriented to the top, the X axis point to the center of the circular collider and the Z axis is align with the beam line with a direction chosen to ensure the right-handed coordinate system.
- This coordinate system is not the most convenient to do physics. In the X, Y plan the ϕ angle is defined from the X axis. The Y axis corresponds to $\phi = \frac{\pi}{2}$. The pseudo-rapidity η is then defined as $\eta = -ln[tan\frac{\theta}{2}]$, where θ is the angle with respect to the Z axis, in the Y, Z plan. Physically, the difference of pseudo-rapidity between two particle, $\Delta(\eta)$, is invariant under boost along the Z axis.

The CMS detector is composed of various subdetectors which are organized in different layers as illustrated in Fig. 1.13. Two main parts can be distinguish, the barrel region which consists into the the cylindrical central part of the detector. And the endcaps region, it consists of disks located at the two extremities of the barrel.

From inside to outside, the CMS detector is composed by the tracker detector (cf sec. 1.3.1), the electromagnetic calorimeter system (cf sec. 1.3.2), the hadronic calorimeter subdetector (cf sec. 1.3.3) and finally the muon identification system (cf 1.3.4). Additional calorimeters are located close to the beam pipe in the forward region in order to increase the detector acceptance up to $|\eta| < 5$.

There is also a solenoid superconducting magnet [51] located between the hadronic calorimeter and the muon system. It produces a 3.8 T magnetic field, parallel to the beam axis, in region of 6 meters of diameters and 12.5 meters long. Outside of the magnet, the magnetic flux is returned through a 10000 tons yoke structure. The purpose of the magnetic field is to curve in the

Figure 1.13 – Schematic repersenation of the CMS detector []. Starting from the interaction point, the detector is composed of; the pixel tracker system, the silicon strip tracker, the electromagnetic calorimeter, the hadronic calorimeter, the magent solenoid and then in the magnet yoke structure, the muon chamber.

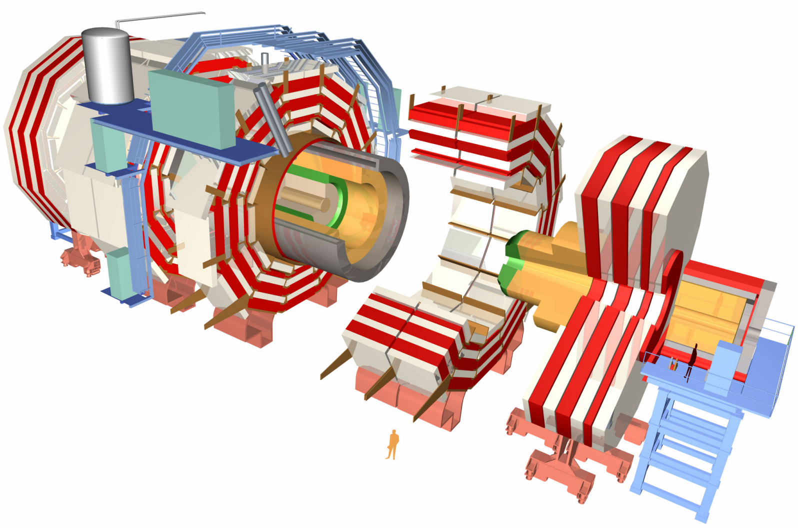

transverse plan the trajectory of charged particles. The transverse momenta of charge particle is computed by the measurement of the Sagitta of the trajectory.

When particles are created they have to pass through the different detector layers to be identified and also to measure their kinematic properties. Each subdetector, detailed in the following sections, provide a fraction of information in order to reconstruct the particles candidate objects. These measurements are not perfect, a degradation of the information due to detector resolution and efficiency occurs.

1.3.1 The tracking system

The inner tracker system of CMS has been designed to provide precise measurement of trajectories of charges particles and precise identification of vertices. The tracker detector observes the charged particles emission. These particles are detected by micro sensor detectors, the set of hits recorded is then used to reconstruct the trajectory of particle. This section describes the tracking system and the tracks reconstruction.

The Tracker is centrally located around the interaction point. It is 5.8 meters long and 2.5 meters of diameters. High precision on the hit position is required for precise reconstruction of trajectories and transverse momentum measurement. It requires a high granularity detector. It also requires to have a fast response detector to avoid overlap between consecutive events.

Figure 1.14 – Structure of the CMS tracker system. View in one quadrant of the $z - r$ plane. From inside to outside, the pixel detector (barrel and end-cap), the TIB and TID the the TOB in the barrel region while the TEC compose the endcap region.

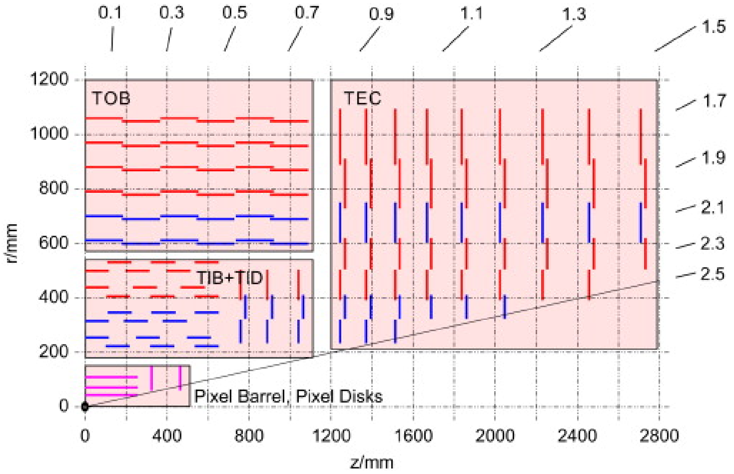

Two different subdetector systems has been choosen to perform the tracking in CMS [52]. A pixel detector and a silicon strip detector. Fig. 1.14 represents the structure of the tracker with all its constituents.

The pixel detector: This subdetector system is composed of three cylindrical layers of 98 *cm* long in the barrel region at radii of 4.4, 7.3 and 10.2 *cm*. There are also two complementary layers in the forwards disks. These disk are located at ±34.5 cm and ±46.5 cm along the Z axis. It is the part the closest to the interaction region. Its acceptance cover $-2.5 < |\eta| < 2.5$ pseudo-rapidity region. The pixel detector delivers three high precision space points on each charged particle trajectory. The pixel detector is important for the secondary vertex reconstruction, which is used for the b-jet identification.

The silicon-strip detector is in the radial region between 20 and 116 cm. It is composed of three different subsystems. The TIB and TID are the tracker inner barrel and disk, the TOB is the tracker outer barrel and the TEC is the tracker endcap.

- The TIB is radially extended from 20 to 55 cm. It is composed of four layers of silicon micro-strip sensors that allow trajectory measurements up to 4 $(r-\Phi)$. The micro-strip sensor are 320 μm and their strip are aligned along the z axis. The two first layer are double sided with sensors, that allows a resolution in the z direction of 230 μm. The $(r-\Phi)$ resolution varies between 23 μm for the two first layers to 35 μm for the two second layers.

- The TID detector is composed of three disks that close the TIB. As for the TIB, the two first layer are double sided with sensors. It's extended between 80 and 90 cm along the z axis. It ensures a pseudo-rapidity coverage up to $|eta| < 2.5$.

- The TOB surround the TIB/TID subsystem. The outer radius of TOB is 116 cm. It is composed of six layers with silicon micro-strip sensors parallel to the z axis. The sensors are 500 μm thick. The TOB detector is 2.18 meters long. The $(r-\Phi)$ resolution is 35 μm for the two external layers and 53 μm for the fourth first layers. As for the TIB and TID, the two first layers are double sided with sensors.

- The TEC subdetector system is composed of nine disks which close the tracker system on both side. Each disks is built with 16 petals. It extends from 124 to 282 cm along the z axis. The radial coverage region is extended from 22.5 cm for the first disks to 113.5 cm for the last disks, that corresponds to the coverage of $|\eta| < 2.5$. The 9 layers carry up to 7 rings of micro-strip sensor. This number goes to 6 from the fourth disk, then to 5 at the sixth disk and finaly the last disk contains 4 rings.

The double sided layer in the TIB and TID are such that the micro-strip are mounted back to back but with and angle of 100 $mrad$ in order to perform a measurement of the second coordinate, z for the barrel detector, and $(r-\Phi)$ for the TID.

Each charged particles produce a signal crossing the tracker layers. This recorded signal called hit contains informations about the position and the charge of the particle. The trajectory of the particle is reconstructed using the set of recorded hits. Based on these tracks the primary vertex is reconstructed as well.

The track reconstruction is an iterative process [53]. It is based on the hits recorded by the Tracker system. The default track reconstruction is performed by the combinatorial track finder algorithm (CTF) [54], starting with the seed finding and then using the capability of the Kalman Filter for simultaneous pattern recognition and track fitting. Starting from an initial estimation of the track parameters, the algorithm iterates through the layers of the tracker and builds a combinatorial tree of track candidates. The seeds are created in the innermost layers of the tracking system. A seed is made out of a hit pair and a loose beamspot constraint or out of a hit triplet. The starting parameters of the trajectory are calculated from a helix passing through the three points. The selected hits must be pointing towards the interaction point and a minimum transverse momentum cut is applied. From each seed a propagation to the next surface is attempted. Hits are identified in a window whose width is related to the precision of the track parameters. If a hit is found within the window, it is added to the candidate trajectory and the track parameters are updated. Candidates are sorted according to their quality (based on the χ^2 and the number of hits) and the best ones are retained for further propagation. The presence of the magnetic field allows to measure the particle transverse momentum and charge via the reconstructed curvature of the track.

The primary vertex reconstruction starts from the tracks collection using the vertex finding. According to the normalized χ^2, the impact parameters and the number of hits, a set of tracks are selected. These tracks are clustered according to their z coordinate of their point of closest approach to the beam line. Vertex candidates are build for each cluster separated by Δz. The primary vertex in then fit from this cluster, with an adaptive vertex fit [55], in which each track is weighted between 0 and 1 according to their compatibility with the common vertex. The resolution on the reconstructed primary vertices depends strongly on the quality and the transverse impulsion and the number of the tracks used to fit them.

1.3.2 Electromagnetic calorimeter and electron reconstruction

Surrounding the tracker, the electromagnetic calorimeters [56] of CMS is an hermitic scintillator detector made of lead tungstate ($PbWO_4$) crystals. This subdetector is the principal system used for the identification and reconstruction of photons and electrons. There are 61200 crystals mounted the barrel region while 7324 from the endcap region which close the subdetector. The light collection is performed by Avalanche Photodiodes (AVDs) in the barrel and vaccum phototriodes in the endcaps (APDs). The use of high density crystals allows a fast response detector with a high granularity and resistant to radiation. One of the main condition for that design is the observability of a Higgs boson decaying into two photons, that was in fact the first discovery channel.

Figure 1.15 – Representative view of a quadrant of the electromagnetic calorimeter. in the $z - y$ plan.

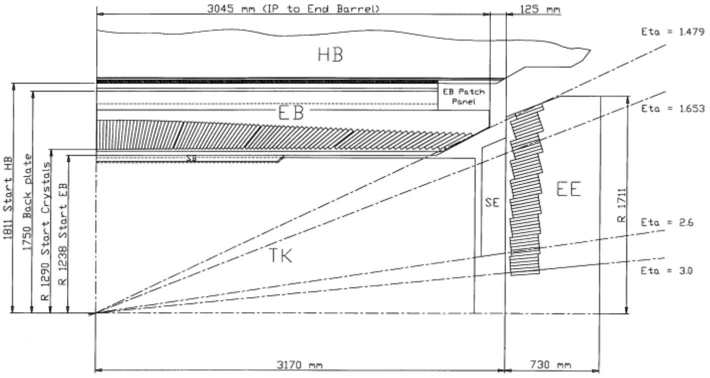

The ECAL barrel detector cover a pseudo-rapidity region up to $|\eta| < 1.479$. The granularity is of 360 elements in Φ and 85 elements in both positive and negative η region. The endcap part of the ECAL is located at 3.17 meters from the interaction point. It covers a pseudo-rapidity range from $|\eta| > 1.479$ to $|\eta| < 3.0$. In the barrel region, the crystals are oriented in direction of the interaction point, with an angle of 3 degrees in Φ and η, as illustrated in Fig. 1.15. The scintillation decay time of these production crystals is of the same order of magnitude as the LHC bunch crossing time.

There is an additional component at this system, the preshower detector which is located between the TEC and the endcap calorimeter. The tickness of this subdetector is of 20 cm. The principal aim of the preshower detector is the neutral pion identification in a fiducial region $1.6 < |\eta| < 2.6$. It also helps for the identification and position determination of the electron. This subdetector is a sampling calorimeter composed of two layers. A lead component initiate the electromagnetic shower, from the incoming photons and electrons, while a layer of silicon strip sensor measure the energy deposit.

At high energy (above 100 MeV), the electrons loose their energy by bremsstrahlung emission of photon. In the matter, the photon at high energy create pair of electron-positron. These two phenomena are repeated and create the electromagnetic shower. At each step of the shower the energy per particle decrease until a critical energy E_c. The material is such as the whole shower is contained in the detector. Electron, positron with an energy below E_c interact inelastically with the electron of the detector matter. The amount of light produced is related to the total energy of the incoming particle $(e^{\pm}, \gamma)$.

The electron reconstruction used information recorded by the electromagnetic calorimeter in addition to tracker measurements. The electron reconstruction start by clustering the the ECAL energy of the electron. The starting point consist to the search of crystals in wich the transverse energy deposit is above a given threshold. A single particle produce a shower affecting several crystals. Around the seed, the energy deposit are grouped by using the Hybrid algorithmin the barrel and the Multi $5x5$ algorithmin the endcap region. After supercluster determination the electron track is identified by matching the ECAL supercluster with triplet of pairs of hits in the inner tracker part, PIXEL or TIB/TID. The supercluster position have to be on the helix of the initial electron trajectory. Then, backpropagating, according to the magnetic field effect, the helix parameters, it is possible to predict the hit position towards the innermost part of tracker to define a track seed. Of course both charge hypothesis are considered to define the windows of search in the tracker. Once a track seed is defined, the full track reconstruction is performed using the GSF (gaussian sum filter) algorithm [57]. This algorithm is an extension of the Kalman filter developed in order to take into account the effect on bremsstrahlung that occurs in the tracker. This effect strongly affect the momentum and energy measurements. This method, providing the ECAL driven GSF electron collection, is very efficient for identification and isolation of electron with a $Pt > 10$ GeV.

The electromagnetic calorimeter resolution on the energy measurement [58] can be parametrized as Eq. 1.28.

$$\left(\tfrac{\sigma}{E}\right)^2 = \left(\tfrac{S}{\sqrt{E}}\right)^2 + \left(\tfrac{N}{E}\right)^2 + C^2 \tag{1.28}$$

where C is a constant term that includes effect from the non-uniformity of longitudinal light collection, the calibration uncertainty and the leakage of energy from the back of the crystal. The noise term, N, groups the electronic noise, the digitization and the pile-up noise effects. There are three contributions to the stochastic term, S: the event to event fluctuation in the lateral shower containment, the photostatistics contribution and the fluctuation of energy deposit in the preshower absorber with respect to what is measured by the preshower silicon detector.

1.3.3 The hadronic calorimeter and jet reconstruction

The hadronic calorimeter, HCAL [56] [59], is important for hadron jet measurement. And it provides indirect measurement of the presence of non-interacting, uncharged particles such as the neutrinos. Surrounding ECAL, the barrel region extend from $R > 1.77$ to $R < 2.95$ and 8.6 meters long. While the endcap parts are located between 300 and 500 cm from the interaction point, along the z axis. The barrel acceptance is extended up to $|\eta| < 1.3$. Endacp parts of HCAL extend it up to $|\eta| < 3$. It is an sampling calorimeter where both barrel and encap subsystem are made of repeating layers of dense absorder and active material. The absorber is made of steel or brass depending of the layer. The active material consist into tile of plastic fluorescent scintillator. Structure of the HCAL is illustrated in Fig. 1.16. Radially, there are 16 layers of absorber and 17 of scintilators.

Figure 1.16 – Representative view of a quadrant of the hadronic calorimeter [59]. in the $z - y$ plan.

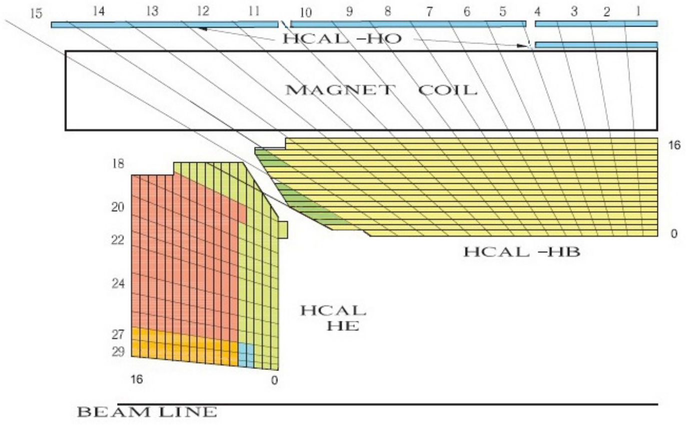

This subdetector system resolution is degraded by the pile-up effect and the hadronization and showering of the hadrons. However the design of the hadron calorimeter impliesa good hermiticity, and a good transverse granularity. The hadronic calorimeter is built in towers oriented to the interaction point. The plastic scintillator is divided into 29 η sectors, resulting in a segmentation $(\Delta\Phi, \Delta\eta) = (0.087, 0.087)$ for the region $|\eta| < 1.6$ $(\Delta\Phi, \Delta\eta) = (0.17, 0.17)$ for the region $1.6 < |\eta| < 3$. The energy resolution is different in the geometrical region of HCAL and can be expressed as:

$$forward: \quad \frac{\sigma_E}{E} = \frac{0.9}{\sqrt{E}} + 0.045 \tag{1.29}$$

$$Barrel/Endcap: \quad \frac{\sigma_E}{E} = \frac{1.72}{\sqrt{E}} + 0.09 \tag{1.30}$$

In addition, two hadronic forward calorimeters (HF) are positioned at each extremity of the CMS detector, close to the beam pipe.

In the central pseudorapidity region, the combined stopping power of EB plus HB does not provide sufficient containment for hadron showers. To ensure adequate sampling depth for $|\eta| < 1.3$, the hadron calorimeter is extended outside the solenoid with a tail catcher called the HO or outer calorimeter. The HO uses the solenoid coil as an additional absorber and is used to identify late starting showers and to measure the shower energy deposited after HB.

The incoming particles interact with the absorber material producing a shower of other particles. The passage of some of these resulting particles in the scintillator layer produce a blue-violet light emission related to the energy of the particle. Light is collected for each scintillating tile.

Due to confinement principle colored particle are not directly observed. The reconstructed objects are jets. It consists to clusters of energy deposits which are supposed to be the result of the parton hadronization. If all the clustered deposits are due to the particles coming from the initial parton, the measurement on the reconstructed jet correspond to the physical one. Resolution on the initial parton kinematic is strongly dependent of the energy-deposit resolution, see Eq 1.29.

These jets are reconstructed by the use of "Jet Algorithms" implemented in the `FASTJET` package [60]. The studies presented in this thesis are based on the use of the anti-k_t algortihm [61].

The anti-Kt jet algorithm is a sequential recombination algorithm. It is a infrared and colinear safe procedure. This algorithm use the distance between elements (energy deposit, particles, pseudojet), d_{ij} and the distance between the beam and the element i, d_{iB}.

$$d_{ij} = min({k_t}_i^{-2}; {k_t}_j^{-2})\frac{\Delta_{ij}}{R^2} \quad (1.31)$$

$$d_{iB} = {k_t}_i^{-2} \quad (1.32)$$

where Δ_{ij} represents the distance in the $\eta - \phi$ plan between the element i and j. Both distances for each element are calculated, and the minimal ones identified. If $d_{ij} < d_{iB}$, the elements i and j are recombined in pseudo-jet. If $d_{ij} > d_{iB}$ i is considered as a jets and removed from the object list. This iterative procedure is repeated until no elements left.

The anti-k_t algorithm is more robust than the other ones with respect to non-perturbative effects like hadronization and underlying event contamination, improving in this way the momentum resolution and therefore the calorimeter performance. Analysis presented in this thesis are based on anti-k_t jets with parameter $R = 0.5$. Due to the dependency in $1/{k_t}_i^2$, the distance d_{ij} between similarly separated soft elements will be much larger. Therefore soft particles will tend to cluster with hard ones long before they cluster among themselves.

Jets energy measured in the detector is typically different from the corresponding particle jet energy. The main sources of these differences are the non uniform and non linear response of the CMS calorimeter to the jet showers. There are also effects due to the electronic noise and the pile-up contamination.

Jet corrections procedure consists to a set of corrections [62] used to take into account some discrepancies between the raw jets (output of the jet algorithm) and generator jets. The first level corrects for the electronic noise effects, and pile-up events. The second correction step, the ”L2” is a relative correction applied in the two jets events. Thats correct jet energy, in function of the pseudo-rapidity and transverse momentum of the jet, with respect to a control region (the barrel region). There is a third level of correction, the ”L3” that is the absolute correction applied to adjust the mean reconstructed energy to the same quantity at generator level.

1.3.4 The muon system

CMS detector includes a dedicated subsystem for muon detection [63]. It has been designed to reconstruct the charge and momentum of muons for a large energy spectrum. The system is composed of three different technologies of gas chamber detector. As the other subdetector, the muon system is naturally divided into a barrel detector and two planar endcap components. The system is located outside of the magnetic coil and is composed by 25000 m^2 of detection planes located inside the free space of the magnetic flux-return iron yoke structure as illustrated in Fig. 1.17. This disposition allows to fully exploit the 1.8 Tesla return flux of the magnetic field.

Figure 1.17 – Structure of the muon system represented in one quadrant of the $z-r$ plane. It is composed of Drift chamber (green), the resistive plate chamber,RPC (red) and the Cathode strip chamber, CSC, (bleu). [63]

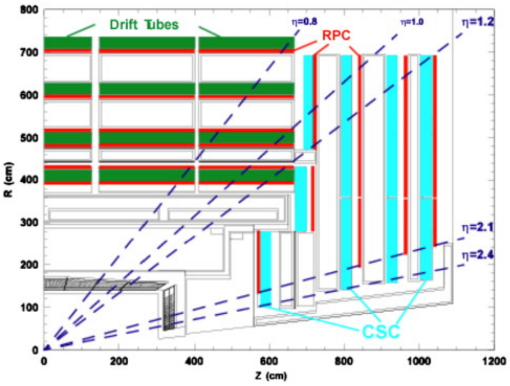

The barrel region system, covering a pseudo-rapidity region up to $|\eta| < 1.2$, is based on the use of drift chamber. Radially four detection stations are disposed in 5 wheels of 12 sectors. There are 60 chambers in each of the three first layers and 70 in the fourth one. The first three stations are composed of 8 chambers providing a measurement of the coordinate in the $(r - \Phi)$ bending plane and a measurement of the z coordinate. The fourth layers does not contain z coordinate measuring plane.

The endcap region of the muon subdetector is composed of CSC (Cathode strip chamber). The CSCs are fast response time detectors and have a fine segmentation, and are radiation resistant. The CSCs identify muons between $0.9 < |\eta| < 2.4$. There are 4 stations of CSCs in each endcap, with chambers positioned perpendicular to the beam line and interspersed between the flux return plates.

Both of the DT and the CSC can trigger on muon transverse momentum with a good efficiency and high background rejection. However a complementary system mainly dedicated to the trigger system is included. It is composed of resistive plate chambers (RPC) and it improves the P_t resolution. A total of 6 layers of RPCs are embedded in the barrel muon system, 2 in each of the first 2 stations, and 1 in each of the last 2 stations.

The muon reconstruction is performed by several ways [64] . The use of muons chambers informations only lead to the "StandAlone Muon". Muons are also reconstructed using the tracker information only, "Tracker Muon". The third algorithm uses information from both and it provides the "Global Muon" collection [65].

- **Tracker muon:** It consists in an inside-outside technique. All tracker reconstructed tracks with a transverse momentum above p_T > 0.5 GeV and a total momentum p_T > 2.5 GeV are considered. These tracks are extrapolated up to the muon system taking into account the trajectory bending due to magnetic field, the average energy losses and the multiple scattering with the material. If an extrapolated track trajectory is compatible with at least one hit in the first station of the muon chamber system, this track is qualified as tracker muon.
- **Global muon:** This outside to inside method is the opposite approach to the tracker muon algorithm. The initial point or the reconstruction is the localization of track segment in the DT, or three measurements in the RPC. Then based on a Kalman filter algorithm the track reconstruction starts. This iterative procedure update the trajectory parameters at each step in order to reduce the bias of the seed. At each of these standalone muon candidate a tracker track is associated by comparing the parameters of the extrapolated two tracks. Combining all the hits, from tracker and muon system, a global muon track in then fitted.

The reconstruction of low P_t muons is better with the tracker muon algorithm while the high transverse momentum muons reach more easily the muon chamber so the global muon algorithm is more appropriated. However to ensure a tighter muon selection candidates must satisfy both tracker and global muon reconstruction criteria. This allows a reduction of the rate of muons from flight decay (muons produced from hadronic decay). This selection is used in many of the CMS analysis.

1.3.5 Particle-flow reconstruction

In addition to the reconstructed objects discussed in the previous sections, CMS analysis are based on a more complete way to reconstruct these objects, the particle flow algorithm, PF [66]. The aim of PF is to identify and reconstruct individually all particle candidate coming from LHC collisions, *i.e.* charged hadrons, neutral hadrons, electrons, muons and photons. It is performed combining information of all different sub-detectors avoiding to use twice the same information, i.e, hit or energy deposit, to reconstruct different particle. The Fig. 1.18 illustrates the particle-flow view.

The particle-flow algorithm works with basic element reconstructed from the different sub-detector. A given particle is, in general, expected to give several particle-flow elements in the various CMS sub-detectors: one charged-particle track, and/or several calorimeter clusters, and/or one muon track. These elements must therefore be somehow connected to each other by a link algorithm to fully reconstruct each single particle. The algorithm produces “blocks” of linked elements, tracks, calorimeter cluster. Due to the CMS detector granularity, these blocks generally group between one and three elements. That constitute the input for particle reconstruction.

Figure 1.18 – Schematic representaion of the Particle flow object by comparison to the detector level. Particle flow particle candidates are constructed using information of several subdetector systems. [66]

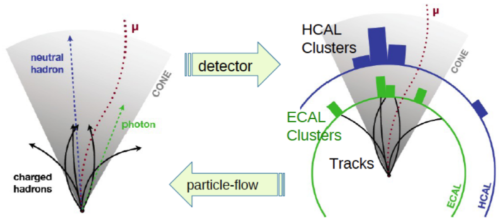

Firstly, each global muon candidate rise to a PF muon and the corresponding track is removed from the block collection. Electron reconstruction and identification follows. Assuming the tracker as a pre-shower system, the electron will produce short tracks and will lost its energy by bremsstrahlung in the tracker layer on their way to the ECAL. These electron candidates are then re-fitted with the GSF algorithm. The identified electrons are qualified of PF electron and the associated tracks and energy deposits are removed from the block. Linked tracks and calorimeter cluster provide charge hadrons candidates,”PF charged hadron”. Several tracks can be associated to a same cluster as one track can be linked to several cluster of ECAL/HCAL. It is performed in a such way that we avoid double counting of energy deposit. The neutral particles are based on the calorimetric energy clusters: clusters separated from the extrapolated position of tracks constitute a clear signature of these neutral particles, photon for ECAL energy deposit and neutral hadron for HCAL energy deposit; neutral particles overlapping with charged particles in the calorimeters can be detected as calorimeter energy excesses with respect to the sum of the associated track momenta.

The PF jets are constructed by the use of jet algorithm, on the particle collection. The anti-k_t PF jets are then considered in the studies presented in this thesis.

This algorithm leads to an improved reconstruction of physical object such as the jet and the transverse missing energy. The transverse missing energy, denoted PF-MeT, is then computed as $E_T^{miss} = -\sum_i \vec{E_t^i}$, where the sum if performed on all the particle i reconstructed by the PF algorithm. In addition to the E_T^{miss} itself its significance is also used.

The E_T^{miss} significance is a likelihood estimator built to quantify the possibility that the reconstructed value of the E_T^{miss} is consistent with fluctuation around zero amplified by finite measurement resolution of the detector [67].

1.3.6 b-jet identification

Among the reconstructed hadron jet, some are coming from B hadron containing b-quark, and are identified. Due to the b quark mass (4.5 GeV) the B-hadron survive during a short time, so it courses a small distance before decaying. Identifying b-jets relies on the properties of the production and the weak decay of B-hadrons. These B-hadron have a lifetime of $\approx$ 1.6 ps, that correspond to an observable flight distance with high resolution tracking detectors. There are different techniques, to perform this b-tag identification, available in CMS [68]. Three of them have been applied in the presented analysis, the track counting (TC), the search for secondary vertex and the combine secondary vertex method. They are briefly described in this section.

- **The track counting algorithm**: The TC approach identifies a jet as a b-jet if it contains at least a minimal number of tracks (N) each with a significance of the impact parameter exceeding a given threshold. B-hadrons present on average 5 charged particles per decay [69]. The discriminator is the value of the significance of the impact parameter for the N-th track, the tracks being ordered in decreasing significance. The discriminators associated with $N = 2$ and N = 3 are called "track counting high efficiency" (TCHE) and "track counting high purity" (TCHP), respectively.

- **The search for secondary vertex tagger (SSV)**: The not negligible lifetime of B-hadron leads to secondary vertices displaced from the primary vertex and charged particle tracks incompatible with the primary vertex. The secondary vertices are reconstructed in an inclusive way, using tracks, inside the jet using the Trimmed Kalman Vertex Finder [70]. The Simple Secondary Vertex (SSV) algorithms use the significance of the flight distance as the discriminating variable. Two working point have been defined, the High efficiency working point, HE, version uses vertices with at least two associated tracks, while the High purity working point, HP, version require at least three tracks.

- **Combine secondary vertex tagger (CSV)**: This algorithm combine the secondary vertex reconstruction and related variables with other kinematical and topological variables as the track impact parameter, to define a b-tag discriminant. Jets are categorized according to the secondary vertex reconstruction. There is first the "reco vertex" category if at least a secondary vertex is correctly identified. The second category called "pseudo vertex" includes events where no secondary vertex are reconstructed and in which tracks not compatible with primary vertex are used to define the pseudo vertex. The last category is called NoVertex, and contains the remaining events. Depending of the category, several variable are used in a multivariate analysis to define the b-tag discriminant. The considered quantities are: the invariant mass, energy and pseudo-rapidity of charged particle associated to the secondary vertex, the distance between primary and secondary vertex, the track impact parameter significance of the first track exceeding the charm threshold. The multiplicity of track associated to the secondary vertex is used as well. Two likelihood ratios are built from these variables. They are used to discriminate between b and c jets and between b and light-parton jets. They are combined with prior weights of 0.25 and 0.75, respectively.

The performances of these b-tag algorithm are available in [68] [71] [72] for the three considered b-tag discriminant.

1.3.7 The CMS trigger system

The LHC produces interactions at high rates 40 MHz frequency, however only a small fraction of these interactions produce interesting events for physics analysis. The purpose of the trigger system is to select the subset of event that are interesting.

A two level trigger system has bee adopted by CMS. The level 1 trigger [73] (L1-trigger) is made of custom designed programmable electronics and is designed to reduce the 40 MHz input rate to a manageable 100 kHz. This hardware system runs on calorimeters and muon system information ,L1 Calorimeter trigger and L1 Muon trigger. These regional trigger search for isolated electron, photon muon or jet and use them to evaluated the MeT. The L1 global trigger combine informations of the two sub-systems in order to take the decision. This decision has to be taken for each bunch crossing.

The second level is the high level trigger [74] (HLT trigger) which feeds the 100 kHz output from the L1 and has access to complete readout of the collision event and reduces the data rate to what is stored, which has to be less then 1 kHz. The HLT code performs reconstruction from all detector system recorded information, using the full granularity. The reliability of HLT algorithms is of capital importance, because events not selected by the HLT are lost. Selected event are then fully reconstructed by the official framework of CMS collaboration, `CMSSW.`[75]

1.4 Monte Carlo simulation

Accurate simulations of CMS events are essential in order to characterize the details of the events observed in the data and to identify interesting events. The simulation is done is several steps of a chain from the event generation to the detector reconstruction. This section briefly describe the events generation and the detector simulation.

Events generation: The event generation step includes hadronization, underlying event, and event pileup. Event generation is done using Monte Carlo (MC) [76] event generators as Pythia [77], MadGraph [78] [79], AlpGen [80], Sherpa [81] or Powheg [82]. The MC generators use Parton Distribution Functions (PDFs) and Feynman calculus to designate the momentum and decay of various particles produced in the hard scattering process.

Concerning the events generation, one approach relies on the factorization principle (sec. 1.2.1) where the event generation starts with a matrix element calculation to give a differential cross section for the hard scattering process. It takes into account the possible interference between all the Feynman diagram due to processes that have the same initial and final states. The integration over the phase space provides an estimation of the cross-section at a fixed order and allows event generation, by Monte-Carlo technique. In addition to the hard scatter interaction the decay of short lived particles is also handled at this stage. The most considered matrix element event generator in this thesis is MadGraph/MadEvent [78] [79], which are leading order matrix element generator.

However the matrix element approach alone is not sufficient to provide realistic simulation. This is due to infrared and collinear divergences that appear when a parton splitting occur, e.i. soft gluon emission. Therefore, a further step deals with the colored partons produced in the previous step and describes the hadronization process in which they are turned into colorless particles. This is referred to as parton showering which include as well the initial and final state radiations (ISR/FSR). ISR/FSR refer to photons radiated from charged particles or gluons radiated from quarks or other gluons before/after the primary hard scatter interaction. Then as last step a program deals with the underlying event, or the soft interactions of the partons present in the proton that are not involved in the hard scatter process. The matrix element generators are interfaced with parton-shower simulation tools as Pythia [77] which handles these two last step. Pythia handles as well the hadronization of the quarks

As matrix element generator and parton shower run independently, the multi-jets events generations suffer from double counting between different multiplicities samples. This problem will affect the cross section estimation as well as the kinematic distributions. The way to handle this problem consists to split the phase space into two regions according an energy scale of QCD emission, Q_{cut}. The soft radiation, below the cut, are generated by the parton shower while the hard radiation by the matrix element generator. This technique is called the jet matching/merging method [83].

The Q_{cut} is expressed in term of P_t and Δ_R between the radiation. It allows to define some jets, called in this context generated jets. The transition between matrix element and parton shower generation have to be smooth with respect to the Q_{cut} variations and the cross-section must be stable as well. This is control looking at the differential jet rate variable.

The energy scale at which an event pass from the $N + 1$ jets configuration to the N jet configuration is used to defined the differential jet rate variable shown in Fig. 1.19. It presents the $1 \to 0$ and $2 \to 1$ differential jet rates assuming a $t\bar{t}$ $+0, 1, 2$ jets sample. As the additional parton multiplicity is 2, it is not require to look at higher orders so the transition $3 \to 2$ is given entirely by the parton shower.

In this example, the Q_{cut} has been chosen at 30 GeV, looking at the differential jet rate distribution, below the matching scale, the shape of the curve is given

Figure 1.19 – Differential jet rate 1 → 0 jet, 2 → 1 jet and 3 → 2 jets from QCD radiation for a $t\bar{t}$ +0, 1, 2 jets production at LHC.

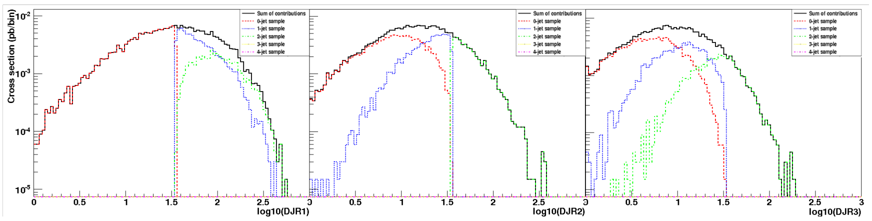

completely by the shower while above the matching scale the shape is mainly given by the matrix element.

Detector simulation: In addition to the event generation, simulation of the event is needed to model the interaction with the detector and the response of the electronics to the final state particles. The CMS detector simulation official software framework (CMSSW) uses the GEANT4 [75] (Geometry ANd Tracking) package. This framework considers a detailed description of the detector materials including sensitive detector, detector parts with sensor readout, and dead materials such as cabling and cooling components. In order to perform studies based on Monte-Carlo simulated events, it takes as input the parton-shower output.

So, the particle interaction with the material is accurately modeled taking into account energy loss and secondary particles produced in the interaction. Moreover information about the magnetic field is used to calculate particle trajectories. The resulting final set of particles is then considered as input of the software component which estimate the response of the detector. The detector noise and other factors are included at this stage. Finally the information is output in the same format as that produced by the actual detector data to be used in such a way the processing of data and simulation is nearly identical during the following stages of analysis.

1.5 The Matrix Element Method

Studies in high energy Particle Physics require to be able to distinguish between the different processes which provide similar final state signature at detector level. The simplest case consists to built a discriminator on one reconstructed observable, i.e. the invariant mass of two leptons to emphasize resonances like J/ψ, υ, or Z^0 boson.

The discriminant power can be enhanced by using a sophisticated algorithm such as Neural Network (NN) [84] or Boosted Decision Tree (BDT) [85] which analyses the distribution of MC events with respect to a large number of observables.

The Matrix Element Method (MEM) is a more advanced technique which is a semi-analytic approach. By opposition to the standard methods which assume the theory information only through the shape of the kinematic variables of the Monte-Carlo simulated events, the Matrix Element method uses an analytic probability density function described by the Feynman amplitude $\mathcal{M}$ of a considered process. So this model dependent approach maximizes the use of theoretical information and estimates the probability that an observed event, denoted p^{vis}, is compatible with a given process describes in a well defined theoretical frame characterized by its parametrization ($\vec{\alpha}$).

This method provides an event by event analysis method which is used for Standard Model precision measurement or for searches. The probability is obtained directly from the theory prediction for the differential cross-sections of the relevant processes and the detector resolution. This probability is then use to do physics measurements. So the mathematical expression for the Matrix Element probability relies on on the description of high energy processes at hadron collider assuming a correct description of the shapes for all the kinematic quantities.

This description assumes the QCD factorization theorem between the hard scattering between the proton constituents which are short distance interactions and their evolution as free particle inside the protons. Considering a case, called ideal situation, in which the kinematic of the particles produced by the hard interaction is perfectly measured, the probability, $P(p_{vis}|\vec{\alpha})$ is expressed by Eq. 1.33.

$$P_{ideal}(p^{vis}|\vec{\alpha}) = \frac{1}{\sigma_{\vec{\alpha}}} \int dq_1 dq_2 f(q_1) f(q_2) \int d\Phi |\mathcal{M}_{\vec{\alpha}}(p)|^2 \delta(p, p^{vis}) \tag{1.33}$$

In this equation, the first integral is done over the parton distribution function, $f(q_1)$ and $f(q_2)$, describing the energy spectrum of the two incoming partons. The second integral evaluates the probability amplitude $|\mathcal{M}_{\vec{\alpha}}(p)|$ of the hard scattering for a specific process between these partons. The associated partonic state to the considered process, p is a configuration of the infinitesimal parton level phase space measure $d\Phi$. The Feynman amplitude contains parton level informations about coupling between particles, intermediates resonances (Breit-Wigner) present in the considered process and the spin correlations as well. This last term gives its name to the technique, the Matrix Element Method [5]. Both of these two theoretical aspects are described by the Standard Model of particle physics. In this presentation the hard scattering probability amplitude is considered at tree-level. The effects due to higher order processes which present extra-radiation will also be discussed.

The normalization factor in Eq. 1.33 is chosen such that the overall expression can be interpreted as a probability density function over the phase space spanned by the reconstructed events satisfying the analysis selection requirements:

$$\int dp^{vis} P_{ideal}(p^{vis}|\vec{\alpha}) = 1. \tag{1.34}$$

This phase space is defined by the detector geometric acceptance efficiency, the detection and reconstruction efficiency, and the analysis event selection efficiency. Because of that the normalization factor becomes $\sigma_\alpha \to \sigma_\alpha^{vis} = \sigma_\alpha \times$ efficiencies factors.

Looking further to a more realistic case, the QCD long distance interactions occurring at lower energy have to be considered. It includes phenomena which occur when colored particles produced by the hard interaction radiate and hadronize, producing jets. Effects due to this evolution from parton level to jet level has to be considered. Moreover the detector resolution on particle observation, briefly discussed in the previous section, induces effects which cannot be neglected. Therefore, in order to deal with these aspects an additional term called the transfer function and denoted $W(p, p_{vis})$ is introduced. The transfer function is defined as a conditional probability, which translates the transition between a final state at generator level characterized by its kinematic and the associated reconstructed final state at detector level. In principle the set of transfer function has to be extracted for each considered processes at a given energy and depends on the detector.

According to that description, a way to define the probability $P(p^{vis}|\vec{\alpha})$ consist to assume a factorization of the processes according to the engaged energy of the phenomena that follow a collision at hadron collider. This approach can be written as Eq.1.35.

$$P(p^{vis}|\vec{\alpha}) = \frac{1}{\sigma_{\vec{\alpha}}} \int dq_1 dq_2 f(q_1) f(q_2) dp |\mathcal{M}_{\vec{\alpha}}(p)|^2 W(p, p_{vis}) \tag{1.35}$$

Moreover there are some ambiguities due to the different object assignment between reconstructed and generated level. This difficulties is handled by the evaluation of the integral of Eq. 1.35 for all the possible configurations, then the different results are combined and normalized to provide the Matrix Element probability. The impact of the consideration of both correct and wrong permutation is discussed in next chapter.

Historically, the prescription Eq. 1.35 on the Matrix Element probability formulation at hadron collider has been introduced in 2000 to perform top quark mass measurement at Tevatron. The goal of the MEM analysis was to use more information with less dependence on the MC. In 2004, the first complete measurement of the top quark mass by the D0 experiment was published [86]. This study has considered all detector effects, i.e. reconstruction efficiencies, cuts, trigger, correct normalization, background probabilities, MC tests of linearity, pull calculations and estimation of systematic effects. The method has been use as well to measure the W boson helicity from top quark decay [87]. A similar Matrix Element method is currently used by CMS collaboration to perform the measurement of the parity of the new Higgs boson candidate [88].

Different studies based on the Matrix Element method are presented in the following of this thesis. Various aspects about the Matrix element method related to the process of interest ($t\bar{t}$, ZH) are presented like the transfer function estimation, the effects due to the L.O. matrix element approximation and the possibility to apply the method for over-constrained processes.

1.5.1 MadWeight

Practically, the integral of Eq. 1.35, is numerically estimated by Monte-Carlo technique using a dedicated tool called MadWeight [89]. This generic and automatic event reweighting software is based on MadGraph which provide the leading order Feynman amplitude $\mathcal{M}$, while the transfer function for the various particle in the final state are user-defined analytical function. MadWeight is able to estimate the Matrix Element weight whatever is the experience process.

The integrator on which MadWeight relies on is VEGAS [90] algorithm. The Monte-Carlo integration procedure generates points in the available phase space according to the structure of a multi-dimensional integration grid which is automatically generated. Due to the complexity of Eq 1.35, there is no simple phase-space parameterization that maps all the peaks in the integrand

It implies that the numerical integration requires to generate a large number of phase space point, this is highly time consuming. In order to handle this difficulty, MadWeight is optimized to perform some change of variable such as the most constrained quantities in the integrant are align with the integration grid. So theses quantities peak along one direction of the grid.

The purpose of MadWeight is to perform automatically the adapted change of variable in order to improve the numerical integration. This transformation is process dependent and is decomposed in a set of change of variable, each of them corresponding to one part of the full decay chain. MadWeight includes generic transformations which correspond to the changes of variable needed for typical subprocesses, these are called blocks. The choice of the blocks to use is driven by the process and also by the choice of the transfer function, δ function will not leads to the same use of block as a more complex TF. The set of block allows to define an optimal change of variable for a large number of process.

There are some processes for which several change of variables are possible. In this case, in order to improve the precision, the computed weight is then given by the weighted sum of the integral estimated with different changes of variable. This is called multi-channel method.

Chapter 2

Matrix Element Method for top quark physics

The Matrix Element Method has already been used at Tevatron in CDF [91] and $D0$ [92] collaborations, for a precise measurement of the top quark mass. However, the performances of this advanced and elegant analysis method have not been studied in the context of physics analyses at the LHC. In order to gain experience with this method this section presents various studies involving top quark pairs produced at LHC energies. We also concentrated on the fully leptonic final states where the MEM is expected to be particularly relevant given the lack of reconstructed information due to the presence of neutrinos.

The first study is probing the possibility to extract the top quark mass with this method. It has been performed with the first 36 pb^{-1} of integrated luminosity recorded by the CMS experiment in 2010, as illustrated in Fig. 2.1. The analysis has been done only with $t\bar{t}$ events decaying in the dimuon channel while the dielectron and electron-muon final states have not been considered. The dileptonic final state is challenging since it does not provide enough observables to kinematically reconstruct the mass of the t and $\bar{t}$ quarks.

The goal of this study is to show that the MEM can be used for a topology where other methods, such as kinematical fitting [93], are expected to show limitations. Effects of wrong pairing and initial state radiations are also briefly discussed.

Figure 2.1 – Evolution of the LHC delivered and the CMS recorded luminosity during the 2010 proton-proton collision campaign.

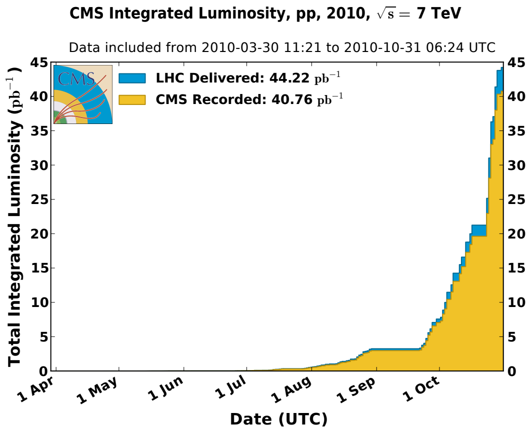

Then an original approach for performing a model independent search of heavy resonances decaying into a top quark pair is addressed by using a variant of the usual MEM.

Both studies are based on the the top quark pair production and decay probability amplitude, $|\mathcal{M}_{pp\to tt\to bl\nu bl\nu}|^2$. The integration has been performed for both jet permutations and results are then combined.

2.1 $t\bar{t}$ dileptonic selection

The dileptonic $t\bar{t}$ events are characterized by the presence of two reconstructed leptons of opposite charge, two reconstructed b-jets and a large transverse missing energy. The main background to $t\bar{t}$ dileptonic events are the diboson (WW) plus jets production, the Drell-Yan plus jets processes and QCD production. Since the goal of these studies is to evaluate the potential of the MEM for top quark physiques without going into a level required for a final analysis, the background contamination effects have not been considered for both studies presented in this chapter. However a reduced background region is defined according to requirements on the reconstructed objects. The selection criteria are based on a reference selection [94] for 2010 data taking used for the first measurement of the top quark pair production cross section at LHC [95].

Due to changes in instantaneous luminosity, the trigger rates and trigger prescales evolve with run number. For this reason, a run dependent trigger selection is applied to the data. The trigger selection is based on single muon HLT triggers, `Mu9`, `Mu11` or `Mu15v1` in function of the run-number.

The purpose of the leptonic selection is to identify the muons coming from a W decay. However, events containing τ decaying to a muon will be automatically selected as well. The selected muon must satisfy the following requirements:

- Be flagged as GlobalMuon and as TrackerMuon, as defined in sec(1.3.4)
- Have a $Pt > 20$ GeV, a pseudorapidity,$|\eta| < 2.4$ and at least one muon with $|\eta| < 2.1$
- The global muon fit has to be perfomed with a number of valid tracker hits (> 10) and a number of valid hits in the muon chamber (> 0) and muon track reconstruction have to satisfy $\chi^2/ndof < 10$ for the global muon fit.
- The muon impact parameter with respect to the beam spot has to be lower than 0.02 cm.

It is also required that muons are isolated with respect to other particles. This isolation can be quantified by evaluating the deposits in the calorimeter and in the tracker systems in a cone around the considered muon. The isolation variable is defined as:

$$I_\mu = \frac{\sum_i^{tracks} Pt_i + \sum_j^{ECAL} Et_j + \sum_k^{HCAL} Et_k}{Pt_\mu} < 0.15 \tag{2.1}$$

The geometrical cone on which this quantity is evaluated has an angle of aperture of $\Delta R = 0.3$.

To avoid pile-up effects, a primary vertex constraint is applied. The two selected muons must be associated to the same primary vertex. The dilepton channel is affected by an important background which is the Z + jets production. This process is strongly reduced by putting a veto on events where the invariant mass of the dimuon pairs is between 76 GeV and 106 GeV. The dilepton invariant mass is also required to be higher than 12 GeV. That allows to reduce the contribution of resonances at lower mass such Upsilons production,$m_\Upsilon = 9$ GeV.

Moreover selection requirement have been applied on the hadronic part of the process. The reconstructed b-jet candidates have to satisfy:

- two particle flow jets, describe in Sec.(1.3.5), reconstructed with the anti$_{kt}$ algorithm, describe in Sec.(1.3.3) with $Pt > 30$ GeV and $|Eta| < 2.4$.
- The Jet overlapping with selected muons candidates are rejected. The overlap region is defined by a cone of $\Delta R > 0.4$ centered on the jet. PFJetID

Due to the presence of two neutrinos in the considered topology, some transverse missing energy is expected. Selected event must have a transverse missing energy above 30 GeV. At this level of the selection the expected yields for the various process are detailed in Table 2.1, and compared to the data. These number have been estimated according to the prescription of the the top-quark mass measurement in the fully-leptonic channel with the 2010 dataset analysis [94].

It is also required that one of the two selected jets is identified as a b-jets. The b-tag algorithm used for this analysis is the `TrackCountingHighEffBJetTags` presented in Sec.(1.3.6) at low working point. The b-jet identification reduces the selected data yields to 24 events.

Table 2.1 – Event yields for the $\mu\mu$ channel in data and MC after the event selection, before the b-tag requirement. MC samples are rescaled to luminosity of 36 pb^{-1}.

Dataset	Lepton sel.	+ Z mass	+ PF jet	+ Met
Z+jets	15479	1239	32.2	3.6
$t\bar{t}$ background	2	1	1	0.8
$t\bar{t}$ dimuon	42	32	23.8	20.3
Single top	3	2	0.8	0.7
Total MC	15525	1275	57.7	25.3
Data	15301	1505	86	28

2.2 Matrix element method for top quark mass measurement

The use of the Matrix Element method for $t\bar{t}$ fully-leptonic studies is not obvious because of missing reconstructed information associated to neutrinos.

On one hand this topology presents, at detector level, eight unknown quantities (dof). Two of them are the *pdf* (fq_1, fq_2) and the other six are due to the non observation of the two neutrinos $(P_t,\ \eta,\ \Phi)_\nu$. On the other hand the Matrix Element method expressed by Eq. 1.35 assumes the conservation of the total energy and the momentum of the system in addition to the presence of the four resonances, two times M_W and M_{top}. Therefore, the number of constraint is equal to the number of dof.

It allows to define a phase space point at generator level that matches with the observed event. However as the relation between constraints and dof is not a linear system, it is possible that different partonic states satisfy the constraints. The Matrix Element integration considers all these possibilities in order to evaluate a probability that the observed event is compatible with a production of top quark pair decaying fully-leptonically.

The first part of this chapter presents the use of Matrix Element method with the goal of estimating some of the $\vec{\alpha}$ parameters. The probabilities, $P(p^{vis}|\vec{\alpha})$ have been estimated for several values of α. Then a discrete likelihood function is defined by the product of the probabilities as expressed by Eq. 2.2.

$$L(\vec{\alpha}) = \prod_{events} P(p^{vis}|\vec{\alpha}). \tag{2.2}$$

The set of parameters $\vec{\alpha}$ that provides the maximum value of the likelihood function is the most probable set of parameters of the considered model. In order to perform a top quark mass measurement, the $\vec{\alpha}$ is the standard model parametrization, where we will vary the m_{top}.

This kind of analysis requires that the transfer function term, $W(p, p^{vis})$ has to be estimated. The next section describes the transfer function estimation for b-jets. The effect of selection efficiency is also discussed.

2.2.1 Transfer Function

The transfer function, $W(p, p^{vis})$, as described in Eq. 1.35 can in principle depends on the studied topology as well as on the event reconstruction.

The transfer function can depend on Pt, η and ϕ for all final state objects and it can therefore be a complicated function. However, in good approximation, it can be drastically simplified by assuming factorization on the different particles in the final state and on the kinematic variables. As already mentioned in chapter 1 the jet energy transfer function takes into account hadronization, showering and detector resolution effects. With these assumptions, the jet to parton transfer function takes the form:

$$W(p, p^{vis}) = \prod_i W_i(p_i, p_i^{vis}) \tag{2.3}$$

$$W_i(p_i, p_i^{vis}) = W_i(E_i, E_i^{vis}) W_i(Eta_i, Eta_i^{vis}) W_i(\phi_i, \phi_i^{vis}) \tag{2.4}$$

Assuming further that for the leptons, energy and direction are well reconstructed, the corresponding transfer functions are three-dimensional δ-function. Finally a perfect measurement of the directions of the jets is also assumed such that only the transfer function for jet energy to parton energy remains non trivial. Furthermore only jets with an energy from 30 GeV are considered. The number of pairs, jet-parton, with jet energy between E^{vis} and $E^{vis} + \delta E^{vis}$ and with parton energy between E and $E + \delta E$ is represented by $n(E^{vis}, E_p)\delta E^{vis}\delta E$. it can be written as:

$$n(E^{vis}, E)\delta E^{vis}\delta E = n(E)\delta E \times W^E(E, E^{vis}) \tag{2.5}$$

where $n(E)\delta E$ represents the number of partons with energy between E and $E+\delta E$. In order to reproduce the peak, the tails and possible bias, the transfer function $W^E(E, E^{vis})$ on jet energy is parametrized as the sum of two gaussians not centered on the same value,

$$W^E(E, E^{vis}) = \frac{1}{\sqrt{2\pi}(a_2 + a_3 a_5)}[e^{-\frac{(E-E^{vis}-a1)^2}{2a_2^2}} + a_3 e^{\frac{(E-E^{vis}-a4)^2}{2a_5^2}}]. \tag{2.6}$$

The parameter a_i depends on the parton energy according to $a_i = a_{i,0} + a_{i,1}E$ [96]. This choice is motivated by the parametrization of the energy resolution of a calorimeter Sec.(1.3.3). It results ten parameters that are extracted by maximizing an unbinned maximum likelihood [97] using a large number of pairs, jet-parton. The matching between generator and reconstructed levels is performed for events selected according to Sec.(2.1) from a specific sample of simulated events generated with $M_{top} = 175\text{GeV}$. The matching criteria between the b-parton and the selected b-jet is the min(ΔR(quark,jets)), with $= \sqrt{(\Delta\eta)^2 + (\Delta\phi)^2} < 0.5$. The likelihood is build as expressed by Eq. 2.7.

$$-\ln L = -\sum_{jets} \ln n(E_j^{vis}, E_j) \tag{2.7}$$

$$= -\sum_{jets} n(E_j) - \sum_{jets} E \times W_j^E(E_j, E_j^{vis}) \tag{2.8}$$

The first term does not depend on the a_i parameters and can be ignored. The transfer function parameters are then fitted using MINUIT [98], by performing a minimization of

$$-\ln L = -\sum_{jets} W^E(E_j, E_j^{vis}) \tag{2.9}$$

The extracted values of the ten parameters and their correlations are presented in the Table 2.2.

The transfer function estimation has been done for b-jets only. A quality check of the parameters is done comparing the two dimensional distributions of parton energy, E, and jet energy, E^{vis} with the prediction of the transfer function, as shown by the Fig. 2.2. As it is not easy to compare two dimensional distributions, projections of $\delta E = E - E^{vis}$ are shown at the Fig. 2.3 for four different ranges of energy. A reasonable level of agreement is obtained.

Table 2.2 – Top: Parameters of the jet energy transfer function extracted by maximizing an unbinned likelihood over pairs associated, by a matching in DR, jet-parton. Jets are the anti-K_t 5 PF-jets. Bottom: correlations between the ten parameters of the transfer function.

Type	independent term	E
Bias first gaussian	$a_{10} = 8.0083 \pm 0.024$	$a_{11} = -0.04874 \pm 0.0013$
Sigma first gaussian	$a_{20} = 6.29 \pm 0.02$	$a_{21} = 0.059 \pm 0.003$
ratio	$a_{30} = -0.01821 \pm 0.0007$	$a_{31} = 0.0011 \pm 0.00002$
Bias second gaussian	$a_{40} = 10.03 \pm 0.34$	$a_{41} = 0.0389 \pm 0.0009$
Sigma second gaussian	$a_{50} = 33.1 \pm 1.2$	$a_{51} = 0.09 \pm 0.0065$

Correlation factors

	a_{10}	a_{11}	a_{20}	a_{21}	a_{30}	a_{31}	a_{40}	a_{41}	a_{50}	a_{51}
a_{10}	1.000	−0.855	0.267	−0.180	−0.236	0.089	0.001	0.066	0.065	0.001
a_{11}	−0.855	1.000	−0.159	0.228	0.2	−0.241	0.00	−0.092	0.164	0.00
a_{20}	0.267	−0.159	1.00	−0.822	−0.288	0.063	0.001	−0.092	0.16	0.002
a_{21}	−0.180	0.228	−0.822	1.00	0.26	−0.31	0.001	0.178	0.188	−0.001
a_{30}	−0.236	0.2	−0.288	0.26	1.00	−0.696	0.0	0.16	0.026	0.003
a_{31}	0.089	−0.241	0.063	−0.31	−0.696	1.00	−0.003	−0.267	−0.618	−0.001
a_{40}	0.001	0.00	0.001	0.001	0.0	−0.003	1.00	0.014	0.004	0.0
a_{41}	0.066	−0.092	−0.092	0.178	0.16	−0.267	0.014	1.00	0.144	−0.00
a_{50}	0.065	0.164	0.16	0.188	0.026	−0.618	0.004	0.144	1.00	0.010
a_{51}	0.001	0.00	0.002	−0.001	0.003	−0.001	0.0	−0.00	0.010	1.00

Figure 2.2 – a) 3D-plot of parton energy vs jet energy for a sample of partons associated to jets. b) 3D-plot of parton energy vs jet energy using a transfer function with double gaussian parametrization and parameters of Table 2.2

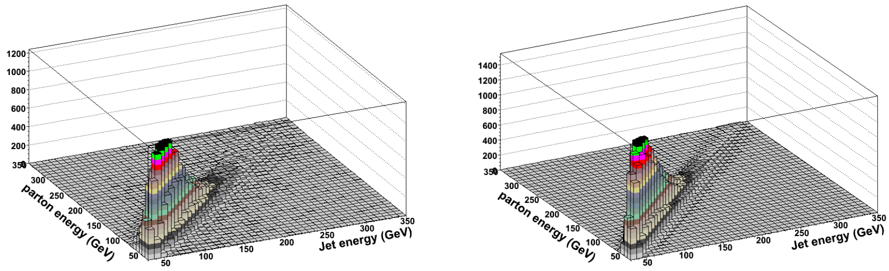

Figure 2.3 – Projection of $\delta E = E - E^{vis}$ for different range in energy to show evolution with energy of the transfer function. The black distribution is obtained by jet-parton association. The blue distribution is built by adding up the fitted transfer function (normalized to unity) for each event.

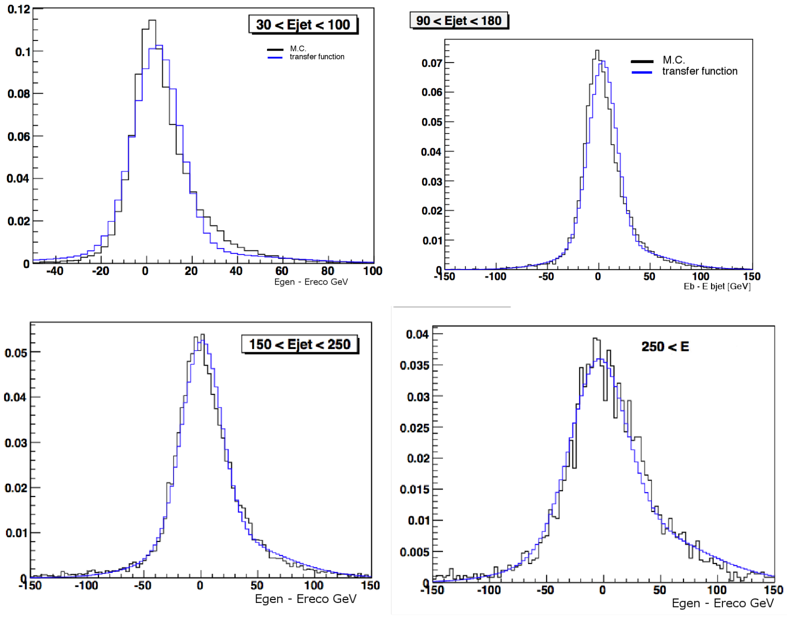

2.2.2 Acceptance term

In a realistic analysis, the phase space on which a measurement is performed is reduced due to different factors, such as the geometrical acceptance of the detector, the trigger, the reconstruction and the selection and reconstruction efficiencies. In order to ensure that the Matrix Element method still provides a probability, the normalization factor is adjusted to this visible phase space, $\frac{1}{\sigma} \rightarrow \frac{1}{\sigma_{vis}}$.

The Matrix Element probability from Eq. 1.35, has to be modified as follows:

$$\bar{P}(p^{vis}|\vec{\alpha}) = \frac{1}{Eff(\alpha)} Acc(p) P(p^{vis}|\vec{\alpha}) \tag{2.10}$$

With $Acc(p)$ equals to one for events passing the event selection. In order to ensure the normalization of $\bar{P}$ as a probability density function,

$$\prod_{events} \int d^3 p_i^{vis} \bar{P}(p^{vis}|\vec{\alpha}) = 1, \tag{2.11}$$

the acceptance correction term $Eff(\alpha)$ is simply related to the event selection efficiency Eff as follows:

$$Eff = \int Acc(p) P(p|\vec{\alpha}) = \frac{\#SelectedEvents}{\#ProducedEvents} \tag{2.12}$$

The corrections associated to the acceptance are corrected on an event by event basis. However as the correction factors are the same for all events the acceptance effect can be considered as a global correction. It implies that the correction can be include at the likelihood computation level such that the function to be minimizes with respect to $\vec{\alpha}$ parameters can be written as Eq. 2.13.

$$-\ln L(\vec{\alpha}) = -\sum_{events} \ln P(p^{vis}|\vec{\alpha}) + N ln(\frac{\#SelectedEvents}{\#ProducedEvents}) \tag{2.13}$$

Where N is the number of selected events.

As far as $t\bar{t}$ events are concerned, the acceptance term has to be computed in the dimuon channel. Based on the selection criteria described in Sec. (2.1), the efficiency term $Eff(\alpha)$ depending of M_{top} has been estimated from simulated events sample with eleven different values for the top quark mass. Then the acceptance term has been fitted by a sigmoid function (Eq. 2.14) as represented in Fig. 2.4

$$Eff(m_{top}) = \frac{P_0}{1 + e^{-P_1(P_2 - m_{top})}} \tag{2.14}$$

Figure 2.4 – Evolution of the selection efficiency, with the top quark mass in the $\mu\mu$ channel, described by a sigmoid function.

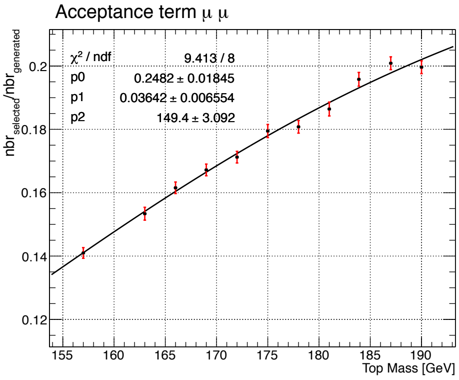

2.3 Top quark mass estimation

The goal of this study is to demonstrate that the Matrix Element method can be used at LHC for precise measurement rather than providing a complete analysis taking into account all the systematic uncertainties. This analysis is based on the transfer function estimated at Sec. (2.2). Results obtained from Monte-carlo simulation at partonic and reconstructed levels are first presented, using the standard $t\bar{t}$ selection defined at Sec. (2.1). Then a more exclusive analysis is presented, that prevents next to leading order effects to be too dominant. For the later analysis, the dataset will be splitted into two samples. The first one contains the events with exactly two jets, the second one contains event with at least three jets.

2.3.1 Determination of the top quark mass at partonic level.

A first analysis is performed at generator level, with a leading order event generator, in order to validate the method. At this level, all transfer functions are assumed to be well modeled by δ-functions. Moreover, it is the same leading order generator (MadGraph) that is use for the event generation, that provides the probability amplitude, $\mathcal{M}$, which is integrated in Eq. 1.35. The unmeasured quantities are the initial parton momentum and the neutrino kinematic variables.

The association of the b-jet between reconstructed and generated level is not unique. Indeed, two possible permutations exist: P_1 (b-jet$_1$ b-quark ; b-jet$_2$ $\bar{b}$-quark) or P_2 (b-jet$_2$ b-quark ; b-jet$_1$ $\bar{b}$-quark). The Matrix Element probabilities are estimated for both of them and then combined. At partonic level it is possible to identify the correct from the wrong permutation and to look at their probabilities separately. The Matrix Element probabilities of both permutations have been estimated with one thousand of $t\bar{t}$ dileptonic events. The variable of interest is the ratio of the wrong permutation probability value by the correct one (P_2/P_1). This quantity is represented in Fig 2.5.

Figure 2.5 – Ratio between the two possible jet permutations of the Matrix Element probabilities estimated for $t\bar{t}$ dilpetonic event at generator level.

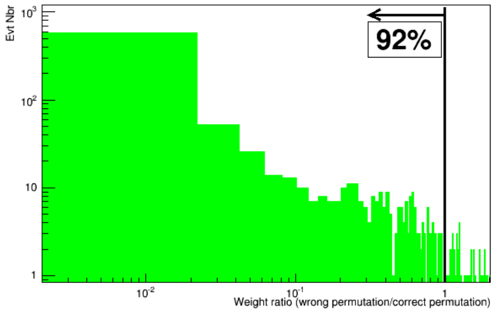

The result shows that for 92% of the events the correct permutation is a larger than the wrong one. The remaining 8% of events can be understood by the fact that the freedom on the kinematic of the two neutrinos allows generator level configuration for which the wrong jet permutation has a larger probability. An analysis of $t\bar{t}$ events decaying in the semi-leptonic channel [99] did a similar study. In what Fellows, the final Matrix Element probability is the result of the combination of both permutation, $P = \frac{P_1+P_2}{2}$.

To perform a top quark mass estimation, the conditional probability $P(p_{vis}|m_{top})$ has been estimated according to twelve top quark mass (m_{top}) hypothesis. These working values have been chosen to be around the true mass. The estimated top quark mass has been extracted using a likelihood function as Eq. 2.13.

Following the $t\bar{t}$ dileptonic selection requirement at Sec.(2.1), 500 $t\bar{t}$ events generated with a top quark mass at 175 GeV have been considered. The selection cuts have been applied at reconstructed level, then the partonic information of the selected event has been used. The Matrix Element method provides an estimation of the top mass of 175.7 ± 0.6 GeV as represented in Fig. 2.6(left). This result includes the statistical uncertainty only. It also illustrates the importance of including the acceptance term correction. Indeed the minimum of the *log* likelihood illustrated in Fig. 2.6(left) presents a shift to upper values for the top quark mass estimation performed without the acceptance correction.

This measurement at parton level has been repeated for eleven samples generated with different top quark mass. Each of these measurement has been performed with the same number of events. The obtained results have been used to estimate a calibration curve that represents the reconstructed value as a function of the true one. A linear fit as been performed according to the parametrization

$$M_{rec} = a \times M_{Gen} + b, \tag{2.15}$$

At partonic level the calibration curve is represented by the Fig. 2.6(right) while the fit parameters are in Table 2.3 and no significant bias on the observed top quark mass appears. That shows a control of the method at generator level. However, the calibration is not perfectly diagonal. Indeed, the slope parameter of the calibration curve is not compatible with 1 within its uncertainty.

A working hypothesis that can explain this effect is the use of the wrong permutation in the Matrix Element probability estimation. Among the eleven different values of the top quark mass measured at partonic level, three have been considered for a more advanced study. Indeed, the top quark mass has been estimated for each of these samples respectively, considering only the Matrix Element probability computed considering the correct permutation only. The resulting calibration curve is shown in Fig. 2.7.

It shows that the slope of the calibration curve is compatible with 1. However, the same comparison assuming only the wrong jet assignment is not possi-

Figure 2.6 – Left: Log likelihood for top mass estimation with $t\bar{t}$ simulated by Monte-Carlo events. Theoretical top quark mass is 175 GeV at partonic level (with and without acceptance term). Right: Calibration curve estimated at generator level.

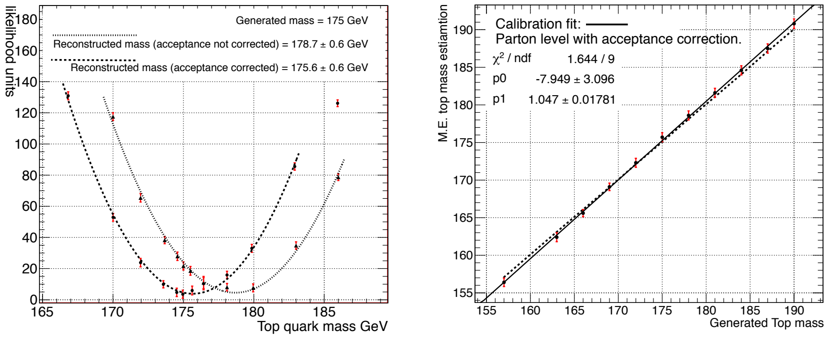

Figure 2.7 – Calibration curve estimated at generator level obtained assuming the Matrix Element probability estimated considering the correct jet assignment only.

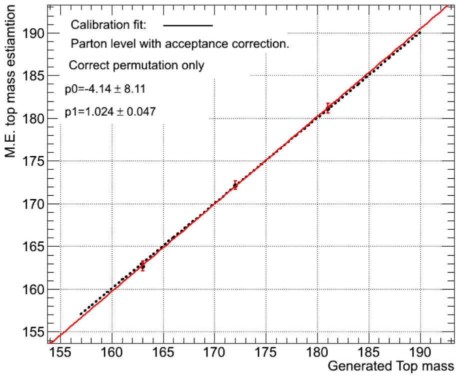

ble, due to the not negligible fraction of event for which the Matrix Element Probability estimation failed assuming only the wrong permutation.

2.3.2 Determination of the top quark mass at reconstructed level.

This second analysis is performed on the same events but the parton shower is initiated as well as the full simulation of the CMS detector response and event reconstruction. Therefore, the transfer function on b-jet energy defined at Sec (2.2.1) is considered. Again a LO Matrix Element assuming generator level final state composed of two muons of opposite sign, two b-quark and two neutrinos is used. At detector reconstructed level, the two most energetic jets (amongst which one must be b-tagged) are considered as the"two" selected b-jets. No corrections related to the amount of initial state radiations have been applied.

Calibration

In order to estimated if any significant bias impact the top quark mass estimation, the measurement has been repeated for several samples of simulated events generated with different top quark mass (163 GeV, 169 GeV, 172 GeV, 175 GeV, 181 GeV,187 GeV) as illustrated in Fig.2.8.

The corresponding calibration curve specific to this selection at reconstructed level is presented in Fig. 2.9. A small deviation with the perfect diagonal is observed. It can be due to the efficiency of the b-jet selection and their assignment and/or due to the approximation of a L.O. Matrix Element for events with extra radiation. The fit parameters related to this curve are listed in Table 2.3.

Expected accuracy on the top quark mass measurement.

A $t\bar{t}$ sample independent to the one used to obtain the calibration curve has been considered. Among this dataset, 500 $t\bar{t}$ events generated with a top quark mass at 172 GeV have been selected. At reconstructed level, the top quark mass has been estimated and corrected according to the calibration curve. The expected top quark mass obtained is

$$M_{top} = 170.75 \text{ GeV} \pm 1.13 \text{ GeV} \pm 0.3 \text{ GeV}_{acc} \pm 0.2 \text{ GeV}_{cali},$$

where the uncertainty related to the acceptance and to the calibration have been clearly separated, on top of the expected statistical error. The error

Figure 2.8 – Representation of the log likelihood for top quark mass estimation with different simulated by Monte-Carlo dataset (full reconstruction). Events are selected according to criteria section defined Sec.(2.1), an inclusive selection asking at least two jets with at least one b-tagged. The two most energetic jets are considered as the b-jets. a) with M_{top} = 163GeV, b) M_{top} = 169GeV , c) M_{top} = 181GeV and d) M_{top} = 187GeV

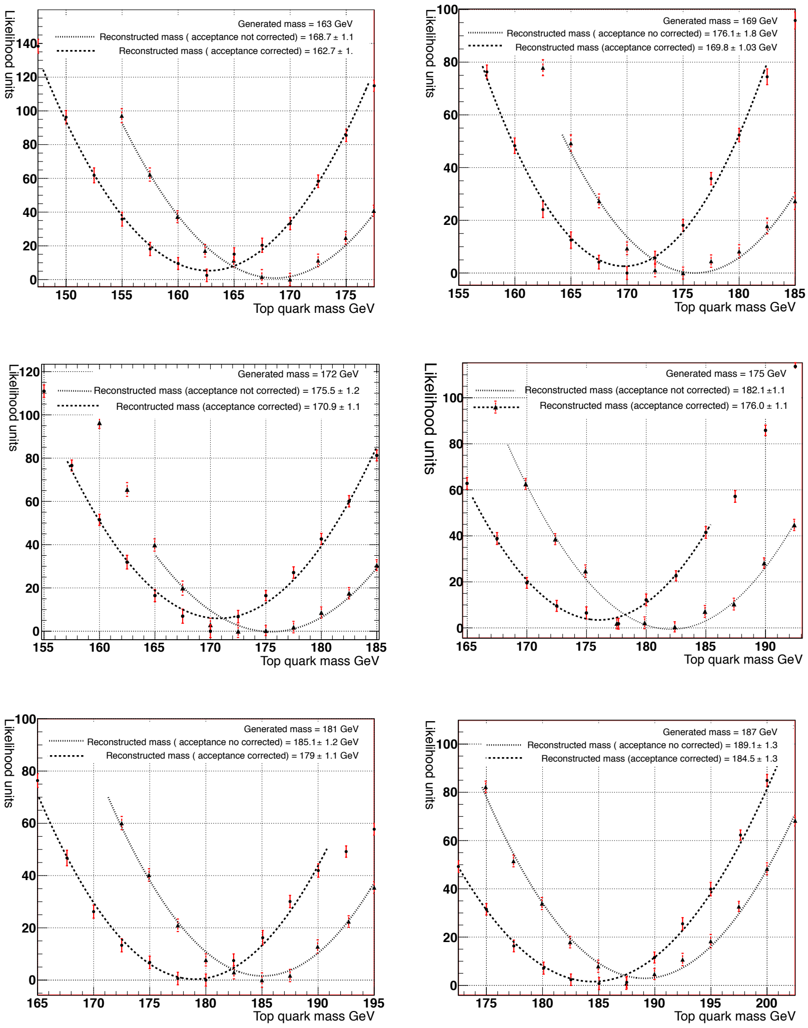

Figure 2.9 – Calibration curve obtained using the inclusive selection asking at least two jets with at least one b-tagged. The two most energetic jets are considered as the b-jets. For each top quark mass 500 events are used. The dotted line represent the perfect diagonal. The error are quadratic combination of the statistical uncertainty with the acceptance error.

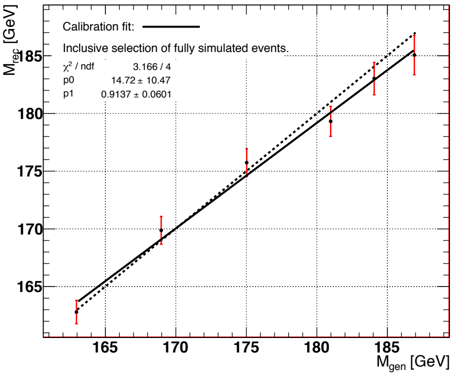

due to the calibration procedure is estimated by variating the parameters of the calibration curve within their uncertainties taking their correlation into account. A similar procedure is applied for evaluating the error related to the acceptance term. In both cases, the quoted error is estimated as the difference between the nominal top mass measurement and the various up and down fluctuations.

2.3.3 Determination of the top quark mass with 36.1 pb^{-1} of 2010 Data

According to what has been described in the previous section a top quark mass estimation based on the Matrix Element method has been performed with the data corresponding to the first 36.1 pb^{-1} recorded in 2010 by CMS where 24 $t\bar{t}$ dimuon candidates have been selected.

The calibration factor established previously has been applied. The measured top quark mass is

$$M_{top} = 173.14 \ \pm 5.8 \ _{stat} \pm 0.3 \ _{acc} \pm 0.3 \ _{cal} \text{ GeV}, \tag{2.16}$$

as represented in Fig. 2.10.

Figure 2.10 – Top quark mass estimation with 2010 CMS data (36.1 pb^{-1}). 24 events selected. The extracted top quark mass value is 172.4 GeV ± 5.8 GeV ± 0.3 GeV$_{acc}$. Using the calibration curve correction : 173.14 GeV ± 5.8 GeV ± 0.3 GeV$_{acc}$.

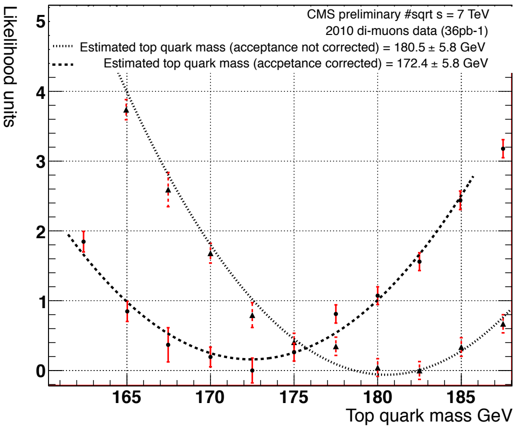

This measurement is in agreement with what was measured by the CMS collaboration with the 36.1 pb^{-1} integrated luminosity of the 2010 dataset in dilepton channel [94], $M_{top} = 172.9 \pm 4.9(stat)^{+3.5}_{-4.2}(syst)$, using both dimuon and dielectron final states. Independently to the systematic uncertainties, the use of the Matrix Element method allows to perform a precise measurement, with equivalent luminosity.

2.3.4 Impact of Extra-radiations

The calibration curves obtained previously seems too good given the difference that exist between the theoretical hypotheses used in the ME-weights and the reality.

Indeed, an important assumption is that the Matrix Element, $\mathcal{M}$, which is being used, considers the production of $t\bar{t}$ pair at leading order, this means without extra jets. It is therefore relevant to evaluate the effect of additional jets. In order to do this, two different selections based on the jets multiplicity have been considered. The first category considers events with exactly two jets with at least one of them being b-tagged. The second category selects events with at least three selected jets. For both selections the calibration procedure has been applied and the expected accuracy computed as in the previous section. Finally the results obtained by these two selections were combined to be compared with what is obtained with the inclusive selection.

Exclusive two jets selection

The measurements presented in this section have been based on events with exactly two jets among which at least one of them have to be identified as a b-jet. The goal is to illustrate the impact of the jet mis-assignement on the estimated top quark mass. First an ideal situation has been considered. It consists to a case in which the identification of a jet as a b-jet is perfect. It is obtained by requiring exactly two real b-jets. This criteria is ensured by using the Monte-Carlo information to do a perfect matching between the selected jets at reconstructed level with the two b-partons coming from the top decay. This matching must be satisfied in a cone of $\Delta R = 0.3$ around the reconstructed jet. According to this selection criteria the acceptance has been re-evaluated and top quark mass measurements have been performed in order to fit the calibration curve presented at the Fig. 2.11.

Figure 2.11 – Calibration curve obtained with a selection of events without extra jet with $p_T > 20$ GeV and with an ideal b-tag based on the Monte-Carlo truth.

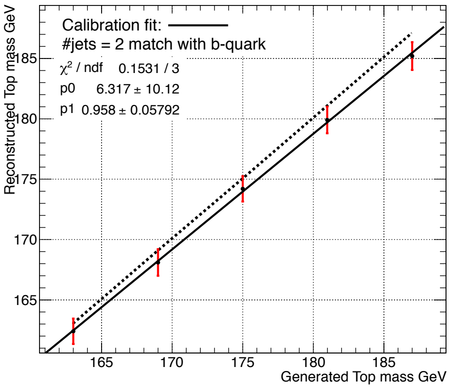

As expected, the calibration curve is compatible with the diagonal. It allows to conclude that the method works well in this ideal situation, it also means for instance that no bias is introduced by the use of a non trivial transfer function.

Then moving to a real b-tag selection, requiring at least one b among the two selected jets, a significant shift towards lower mass is observed on the calibration curve represented in Fig 2.12. The linear parametrization of this curve is shown in Table. 2.3. It illustrates a non negligible effect of b-jet mis-assignement on the m_{top} measurement.

Figure 2.12 – Selection efficiency depending on the top quark mass for the dimuon decay channel. Selection of events with exactly two jets passing the selection criteria, no MC-matching applied on these selections.

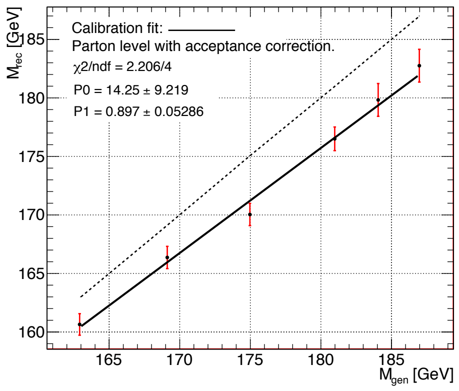

The expected accuracy for this exclusive selection has been estimated from a subset of 323 two-jets events selected from the independent sample generated with generated $m_t = 172$ GeV. After application of the calibration factor, the estimated top mass result is

$$M_{top}(njet = 2) = 171.5 \ \pm \ 1.13 \ _{stat} \ \pm \ 0.3 \ _{acc} \ \pm \ 0.3 \ _{cali} \text{ GeV}. \tag{2.17}$$

Exclusive more than two jets selection

The second category studied is based on a $t\bar{t}$+jet(s) selection. Still using the matrix element of $t\bar{t}$ decaying in the dimuon channel at leading order, this selection will be sensitive to the effect of the extra-radiation on the top quark mass measurement. The two most energetic jets are considered as the two b-jets, and at least one of them has to be b-tagged. So the extra-jets are not considered in by the Matrix Element method and the considered transfer function are still the one defined in Sec. (2.2.1).

The calibration curve (parameters are listed in Table 2.3) showed in Fig. 2.13 and corresponding to the selection of events containing at least three jets and analyzed with a Matrix Element of $t\bar{t}+0jets$, is this time shifted towards upper top mass values with respect to the generated ones. This is due to the presence of initial state radiation with jets of transverse momentum above 30 GeV. It is to be compared with the ideal case, without ISR (with $Pt > 20$ GeV) and with the correct jets selection [100].

Figure 2.13 – Calibration curve computed from top mass estimation using sample of events selected according to section [3] and containing three jets and more (with at least one b-tag requested).

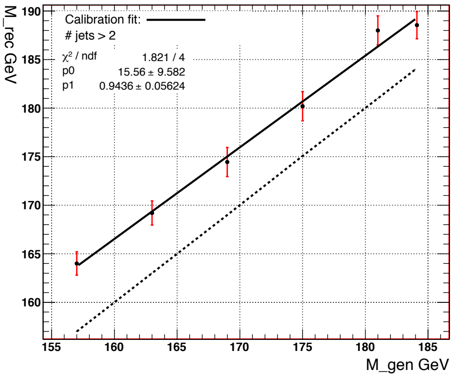

As for the previous selections, the accuracy in the measurement is evaluated using the independent samples generated with $M_{top} = 172$ GeV. The estimated top mass value is

$$M_{top}(njet > 2) = 169.5 \ \pm \ 2.06 \ _{stat} \ \pm \ 0.3 \ _{acc} \ \pm \ 0.4 \ _{cali} \ \text{GeV}. \quad (2.18)$$

The Table 2.4 summarizes, for the different selections presented, the impact of the acceptance and the calibration corrections on the top quark mass esti-

Table 2.3 – Parameter of the linear fit of the calibration curves for the inclusive and the two exclusives selection presented. The slope and the offset parameter are close to 100% anti-correlated.

	Slope	Offset
inclusive	0.91 ± 0.06	14.7 ± 8.5
exclusive 2 jets	0.90 ± 0.05	14.25 ± 9.2
exclusive > 2 jets	0.94 ± 0.06	15.6 ± 9.6

mated with the Matrix Element method from a sample generated with $m_{top} =$ 172 GeV. These measurements are all compatible with the generated values.

Table 2.4 – Estimated top quark mass according to the inclusive at the different step of the coreection procedure, the acceptance and the calibration. Only statistical uncertainties are presented in this Table.

	M.E. output	+ Acc	+ Cal
inclusive	175.25 ± 1.24 GeV	170.7 ± 1.14 GeV	170.75 ± 1.14 GeV
exclusive 2 jets	172.8 ± 1.32 GeV	168.1 ± 1.3 GeV	171.5 ± 1.4 GeV
exclusive > 2 jets	184.4 ± 2.4 GeV	173.6 ± 2.06 GeV	169.5 ± 2.08 GeV

Combination

For an analysis categorizing events as a function of the jet multiplicity, the final top quark mass can be obtained by the combination of the two exclusive measurements illustrated in Fig. 2.14.

There are different methods to combine these measurements. The first way consist to do a weighted sum of the two independent final results obtained in each channel. It is expressed by Eq. 2.19 [11].

$$\mu = \frac{1}{w}\sum_{i=1}^{N} w_i x_i \tag{2.19}$$

where $i = 2$, x_i are the two estimated values, w_i is defined as $\frac{1}{\sigma_i^2}$ and $w = \sum_i w_i$. This operation provides a reconstructed top quark mass value of 170.8 GeV ±1.15 GeV, statistical uncertainty only.

Figure 2.14 – Top quark mass estimation for a dataset with 500 event with $M_{top} =$ 172 GeV. LEFT : reconstruction using the exclusive two jets selection, on 323 events, the estimated value is 171.5 ± 1.13 $_{stat}$ ± 0.3 $_{acc}$ ± 0.3 $_{cali}$ GeV. RIGHT : reconstruction using the exclusive three jets and more selection, on 177 events, the estimated value is 169.5 ± 2.06 $_{stat}$ ± 0.3 $_{acc}$ ± 0.4 $_{cali}$ GeV.

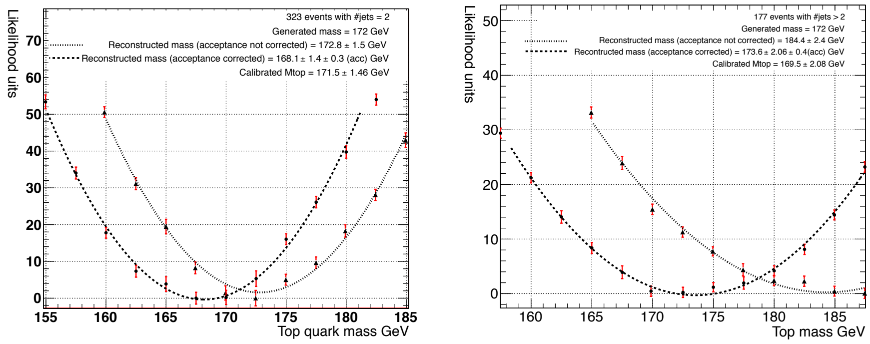

An other method to combine the two results obtained from the exclusive analysis consists into a combination of the two *log* likelihood corrected by the calibration. Applying this method the estimated top quark mass is evaluated at

$$M_{top}(comb) = 170.94 \ \pm 1.09 \ _{stat} \ {}^{+0.033}_{-0.35} \ _{acc+cali}\text{GeV}. \tag{2.20}$$

This way to combine both measurements is illustrated in Fig. 2.15.

This combination is in agreement with the measure performed with an inclusive selection. However, we have shown that the result, obtained with the inclusive selection, is affected by two effects shifting the observed value of the top mass in opposite direction. All these results are summarized in Table 2.5. Moreover it is observed a slightly lower uncertainty combining results from the two exclusive selections can be observed.

Figure 2.15 – Top quark mass estimation for a dataset with 500 events with $M_{top} = 172$ GeV. Combination of the $-Log$ likelihood used for top quark mass estimation for the two exclusive analysis.

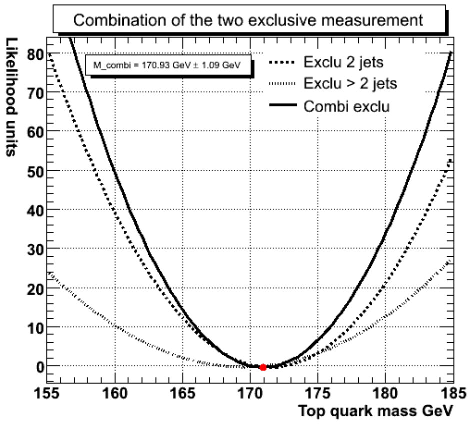

Table 2.5 – Top quark mass estimated according to the inclusive, the two exclusive selections separetely and the combination of the two exclusive measurements. The central value, statistical, acceptance and calibration uncertainties are presented.

	Top Mass	σ_{stat}	σ_{acc}	σ_{cal}		σ_{tot}
inclusive	170.75 GeV	1.14	0.32	0.19		1.19
exclusive 2 jets	171.50 GeV	1.40	0.37	0.23		1.46
exclusive > 2 jets	169.54 GeV	2.07	0.38	0.44		2.15
All exclusive	170.94 GeV	1.09		$^{+0.35}_{-0.33}$		$^{+1.15}_{-1.14}$

2.3.5 Effects of initial state radiations

The top-quark mass estimation shows that the use of a leading order matrix element, for $t\bar{t}$ dimuon event that presents additional jet is not a correct assumption. As presented in Fig. 2.13 the presence of extra-jet impacts the value of the estimated top quark mass. Indeed, this LO approximation implies that considering the $t\bar{t}$ dileptonic process ($\mu\mu bb\nu_\mu\nu_\mu$), the Matrix Element probability computation can be performed only on events with a final state that corresponds exactly to the leading-order one.

For any event with a jet multiplicity larger then the leading order jet number, the evaluation of the corresponding weight takes as input a reduced event. It is defined as the set of all the reconstructed objects that corresponds to the final state of the LO matrix element. In presence of jets from initial state radiation, the kinematic of the reduce event would violate the energy momentum conservation imposed as constraint to the partonic state generated for the integration.

According to that, the reduced event is recoiling against the momentum associated with the extra radiation in the primary events. In particular, the transverse momentum is not necessarily balanced among the final state particles in the reduced event. The Fig. 2.16 illustrates an example of $t\bar{t}$ event with one ISR.

Figure 2.16 – Example of a $t\bar{t}$ process with one initial state radiation. The reduced event is represented by the diagram inside the box. The ISR boost correction is equal to the P_t of the extra radiation or can be deduced from the reduced event.

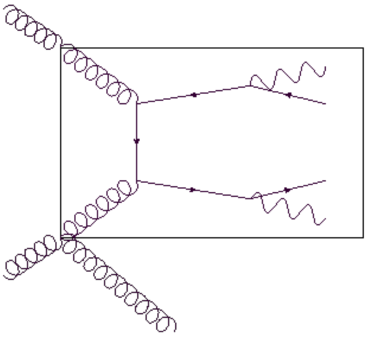

The Matrix Element method has been adapted in order to take into account these effects by modifying the standard definition of the Matrix Elements weights. In the center of mass (cms) frame, the incoming partons have no transverse momentum. However, the weights are evaluated in the laboratory frame which requires to boost the momenta of the initial partons, from the cms frame, to balance the recoil of the reduced event. As the integration is anyway performed on the longitudinal component on the incoming partons, the boost is performed only on the transverse plan.

The simple boost method has the advantage not to increase the computing time for weight evaluation. However, this correction method considers only the kinematic balance of the event and not the QCD effect that involves the coupling producing the extra jets. More details on the treatment of initial state radiation effects on matrix element methods are given in [100].

Different approaches to determine this boost can be applied. One solution consists to built a transverse boost correction using the kinematic of the reconstructed additional jets. So the determination of a transfer function on the extra-radiation is required. It implies a bias due to the threshold of jets selection. A second approach, that is the choice in the presented analysis evaluated the boost from the reduced event information.

A first one can be used for all kind of processes that presents neutrinos in the final state, i.e. $t\bar{t}$ production or single top in leptonic channels. The boost, given by Eq. 2.21, is computed from the visible final state of the reduced events and the E_t^{miss}.

$$\vec{P}t_{boost} = -\sum_{extra-jets} \vec{P}t = \sum_{reducedFinalState} \vec{P}t + \vec{E_t^{miss}}. \tag{2.21}$$

Where the sum is done over all the reconstructed objects that form the reduced final state. The p_T of the ISR system is then indirectly estimated.

The measurement of top quark mass from $t\bar{t}$ events with more than two jets, discussed in sec (2.3.3), has been reproduced with the ISR correction based on Eq. 2.21. The comparison with and without the correction is illustrated, in Fig. 2.17(left), for a Monte-Carlo study with a sample generated with M_{top} at 175 GeV. A shift of ≈ 4 GeV to lower mass is observable. The Fig. 2.17(right) represents the calibration curve obtained measuring the top quark mass on $t\bar{t}$ +jets events and applying the boost correction for extra-jet. The slope of this curve 1.08 ± 0.9 is compatible with 1.

Concerning processes with as property that the final state is composed only by visible particles, i.e. Z(ll)bb, or Z(ll)H(bb), the transverse boost can be expressed differently. For this category of processes, the prescription is that the P_t of the ISR system is completely balanced by the transverse momentum of reduced final state. In this approximation, the kinematic information of the initial state radiation are not used as well. In this case, the boost is defined by Eq. 3.2.

$$\vec{P}t_{boost} = -\sum_{ISR} \vec{P}t = \sum_{reducedFinalState} \vec{P}t. \tag{2.22}$$

Figure 2.17 – -a) Fit of top quark mass from M.C. sample (generated mass 175 GeV). The dotted line is obtained with matrix element weights without ISR correction. The dashed line represents the fit with from matrix element weight evaluate with ISR correction. -b) Callibration curve for event with more than two jets. Without ISR correction, dashed line. With the ISR correction, full line.

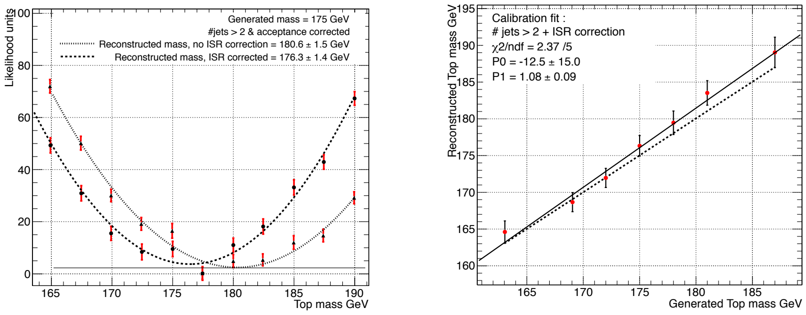

(a)

(b)

These corrections of ISR constitute an important aspect of the Matrix Element method, especially to estimate weights for over-constraints processes. For this kind of processes, a non application of the transverse boost correction would not allow to cover the phase space where the cross section is high, due to the presence of narrow resonances.

This method allows to consider ISR on large P_t spectrum. Anyway, a more realistic description of the kinematic of event with hard extra-radiations will be to include them in the matrix element computation.

2.4 Differential matrix element method

The Matrix Element reweighting is generally used for precision measurement (e.i. mass measurement, W polarization, ...). This analysis technique can be used to extract differential cross sections.

Evidences for new physics in top quark pair production are predicted in many theories and can be observed by estimating differential cross section with respect to arbitrary quantities. However, in high energy collider physics, some observables cannot be fully reconstructed using the detector information only. Techniques like kinematical fitting (KF) or matrix weighted template (MWT) [101] have been developed to handle this difficulty – see for example [93]. This is for instance the case for top quark pair production, where two leptons are present in the final state together with two neutrinos that cannot be detected.

In this section, i present an analysis technique named Differential Matrix Element Method (DMEM) [102] is presented. It estimates differential cross-section using for each event a density of probability.

2.4.1 The method

The matrix element method as described in the previous chapter has been slightly modified. The technique has been adapted to be able to estimate differential cross sections with respect to arbitrary variables X. It is done by estimating probability density functions (pdf) of arbitrary variables as $\frac{\partial \mathcal{P}}{\partial X}(p^{vis})$.

From the Eq. 1.35, the probability density function expression correspond to the relation:

$$\frac{\partial \mathcal{P}(p^{vis})}{\partial m(p^{vis})}|m_0 = \frac{1}{\sigma}\int dx_1 dx_2 f(x_1) f(x_2) d\Phi |\mathcal{M}_(p)|^2 W(p, p^{vis}) \times \delta(m_{(p^{vis})} - m_0). \tag{2.23}$$

Technically, this integration is too complex to be performed with the δ function. In order to handle this difficulty Eq. 2.23 is evaluated on small interval (m_0, m_{0+i}) as

$$\int_{m_0}^{m_{0+i}} dm^* \frac{\partial \mathcal{P}(p^{vis})}{\partial m(p^{vis})}|m^* \quad \text{with: } \delta(m_{(p^{vis})} - m_0) \rightarrow \chi(m_{(p^{vis})}, m_0, m_{0+i})$$

(2.24)

where χ is different from 0 in the considered interval. The integration is performed by MadWeight discussed at Sec. (1.4.1.), and all the requested differential quantities are evaluated at the same time. For each partonic state, generated for the Monte-Carlo integration, the quantities of interest, $m(p^{vis})$, have been estimated. This way to evaluate on small intervals introduces a binning of the differential variables. The number of bins used in this presentation is 50 whatever is the variable of interest.

It results, for each event, one *pdf* associated to the variable of interest, as illustrated in Fig 2.18 for the $t\bar{t}$ invariant mass. A double peak structure can be observe for some events, it results from the two possible jets permutations. Differential cross section estimator are built by combining all the normalized event *pdf's*, $\frac{1}{\mathcal{P}}\frac{d\mathcal{P}}{dm}$.

An analysis based on a similar method was performed at CDF II to search resonant productions of $t\bar{t}$ pairs decaying semi-leptonically with an integrated luminosity of 4.8 fb^{-1} [103].

2.4.2 Prospect at LHC with $\sqrt{s} = 14$TeV

In order to observe the feasibility of such a techniques MadGraph samples of $t\bar{t}$ events decaying in the dimuon channel have been generated ($\sqrt{s} = 14$ TeV). The variables of interest considered are the invariant mass of the $t\bar{t}$ system and the decay angle of the top quark, $\cos\theta^*$. Applying the method at parton level, the Fig. 2.19(a) and Fig. 2.19(b) illustrate the agreement between the theory (No ISR, No UE) with the DMEM reconstructed quantities for the two variables of interest.

In particular there is no bias, due to the lack of knowledge about neutrino kinematic, is introduce.

In order to do a more realistic study these events are passed through PYTHIA with ISR activated. However, the matrix element is still a LO matrix element without the ISR correction mentioned previously. Moreover a fast detector response simulation was performed with `Delphes` [104]. As for the top quark mass analysis, the transfer function on leptons energy and direction are set to δ

Figure 2.18 – Example with four single event of the differential distribution of the Matrix Element weight with respect to the invariant mass of the $t\bar{t}$ system.

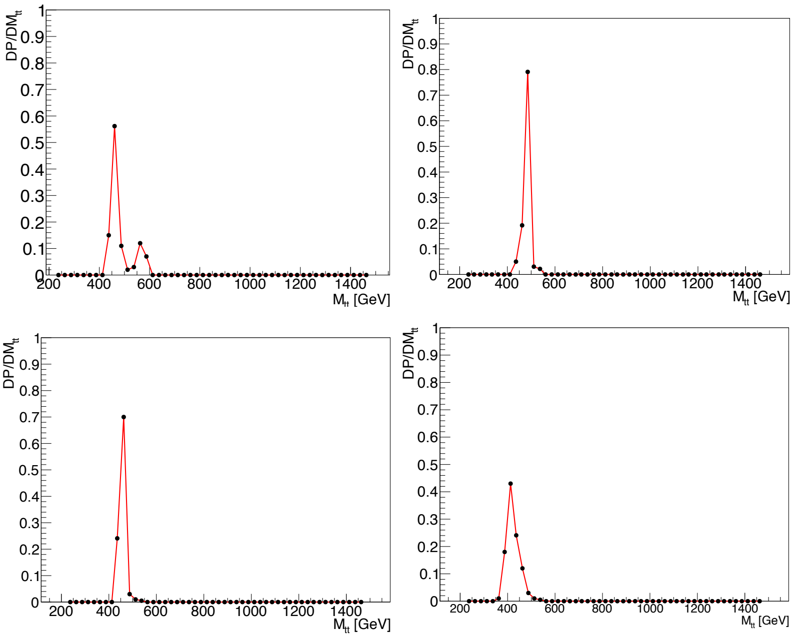

function as well for the transfer function on jets direction. Jets energy transfer function has been refitted [1].

Some selection criteria similar to those described in Sec.(2.1) are applied. Events are required to have exactly two jets with a transverse momentum larger than 30 GeV , and of two opposite sign leptons with $p_T > 20$ GeV . Additionally, a transverse missing energy larger than 30 GeV is required.

Even with the use of the transfer function and the fact that ISR contaminations. One observes that the differential curve, obtained with the DMEM, reproduces the theoretical curves without any significant bias as shown in Fig. 2.20(a) and Fig. 2.20(b).

A theoretical frame [105] with a spin 1 resonance decaying in $t\bar{t}$ ($Z' \rightarrow t\bar{t} \rightarrow l b \nu l b \nu$) has been chosen to illustrate the efficiency of the method by the reconstruction of the two differential cross-sections. The considered model includes a Z' with a mass of 1 TeV. Several configurations have been tested according to

---

[1] fit preformed for double gaussian parametrization as in Sec.(2.2.1)

Figure 2.19 – -a) $M_{t\bar{t}}$ normalised differential cross section.-b) $\cos\theta^*$ normalised differential cross section. Both are produced with 5000 top quark pair events decaying in fully leptonic channel. The theoretical curve (black) are the expected one at tree-level when neither ISR and UE are taken into account. The DMEM has been used on the partonic events (red) without considering the neutrinos.

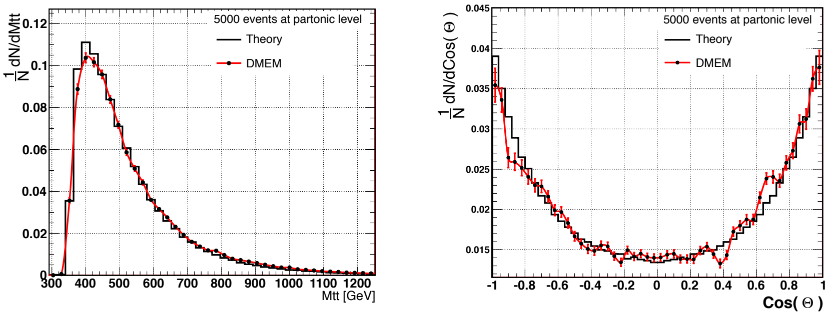

(a) (b)

Figure 2.20 – -a) $M_{t\bar{t}}$ normalized differential cross section.-b) $\cos\theta^*$ normalized differential cross section. Both are produced with 10000 top quark pair events decaying in fully leptonic channel. The theoretical curve are the expected one at tree-level when neither ISR and UE are taken into account. The DMEM is used on fully simulated events.

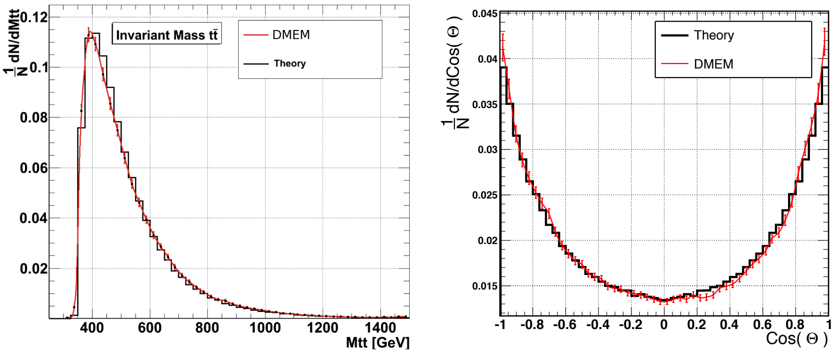

(a) (b)

different contaminations $\frac{N_{Z'}}{N_{tot}} = (2, 3, 5, 8, 10)\%$. It is important to stress that the square matrix element used in E. 2.23 is the standard model one. Samples of 5000 events have been analyzed, corresponding to an integrated luminosity of 5 fb^{-1}.

The $t\bar{t}$ invariant mass spectrum shows the presence of new resonances as illustrated in Fig. 2.21. Selecting the events contributing above 700 GeV in this spectrum, the angular distribution $\cos\theta^*$ was built, Fig. 2.22. This variable is sensitive to the spin of the new $t\bar{t}$ resonance decaying in top quark pairs [105].

Figure 2.21 – $t\bar{t}$ invariant mass spectrum recontructed with the differential matric element method. This variable is presented with the standard model expectation only and for several samples with various degree of contamination in $Z' \to t\bar{t}$. The Z' was generated with a mass of 1 TeV.

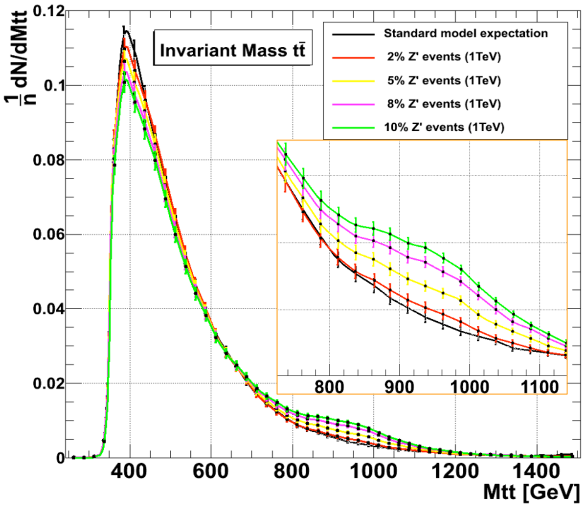

Deviations from the standard model are clearly visible, on both distributions, when the ratio of new physics increases. The shape of the $\cos\theta^*$ distribution is in agreement with what is expected for a spin 1 hypothesis.

To be able to claim any deviation from the standard model from these variables. A χ^2 estimator has been defined to quantify these tendencies. Since each event provides a binned *pdf* , all bins are correlated to each other. Using 100.000 $t\bar{t}$ fully leptonic events theses correlations have been computed, they are presented in Fig. 2.24(a), for M_{tt} and in Fig. 2.24(b) for $\cos\theta^*$.

A χ^2 estimator is constructed according to

Figure 2.22 – Distribution of the diffusion angle of the top quark, $\cos\theta^*$ emission reconstructed by the Differential Matrix Element method. Variable represented for events with DMEM reconstructed $M_{t\bar{t}}$ that peak above 700 GeV for several sample containing different fraction of new physics event ($Z' \to t\bar{t}$).

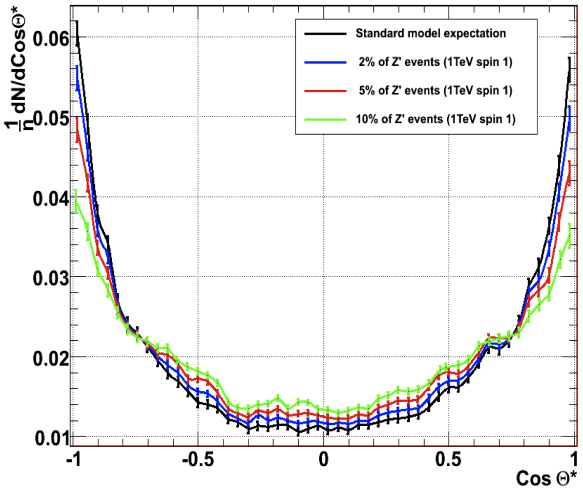

$$\sum_{ij} C^{-1}_{ij} \frac{(x_i - x_i^{th})}{\sigma_i} \frac{(x_j - x_j^{th})}{\sigma_j}, \tag{2.25}$$

where i and j are the bins, σ_i the variance of bin i and C_{ij} the covariance matrix element. This estimator is converted to a confidence level ($CL(\chi^2_0) = \mathcal{P}(\chi^2 \geq \chi^2_0)$) value of standard model exclusion, as shown in Table 2.6. With an integrated luminosity of 5 fb^{-1} looking at selected event samples, containing 2% of Z', the standard model is excluded at 72%. Increasing the new physics proportions in the samples, the standard model can be excluded at 99.998% above 5% of Z' events.

Table 2.6 – Confidence level for standard model exclusion computed on several samples for different contamination of Z' events.

$\frac{N_{Z'}}{N_{tot}}$	2%	3%	5%	8%	10%
C.L. for S.M. exclusion	72%	95.6%	> 99.998%		

2.5 Conclusion

This chapter presented that the use of the Matrix Element method at LHC could provides a top quark mass estimation compatible with the measurements performed by the CMS collaboration. Although the presented result seems is competitive in terms of statistical uncertainty with respect to the measurement done with other methods used so far in CMS. A full analysis requires to study the impacts of the systematics uncertainties and the background contamination effects which were not investigated in this work. However, the analysis presented in this chapter revealed important effects due to initial state radiations.

Indeed, it has been shown that the method is well understood at generator level as well as at reconstructed level, considering the use of non trivial transfer function. Moreover, the top quark mass measurement illustrates the sensitivity of such a method to the impacts of the wrong jets assignment on a precision measurement. It also illustrates the limitation of the approximation of the method to the use of a leading order matrix element. Indeed, performing a measurement on a set of events that present extra jets, it introduces a bias on the observed top quark mass.

In order to handle this problem, this analysis presented a method that consist to estimate the transverse momentum of the extra radiation Pt_{isr} and to apply the Matrix Element method boosting the event in the transverse plane according to Pt_{isr}. The top quark measurements according to this recipe performed with $t\bar{t}$ +jets events illustrate that this correction works well since the measured values are in agreement with the generated one.

Finally, this chapter introduced an analysis technique based on the Matrix Element method with the purpose to search for new physics in the spectrum of differential cross section with respect to arbitrary variable, e.g. the $t\bar{t}$ invariant mass. It has been shown that this analysis technique called Differential Matrix

Figure 2.23 – Matrix representing correlation between bins for variables reconstructed with the differential matrix element method. These matrices have been estimated using exclusively 10000 standard model $t\bar{t}$ fully leptonic events. This results is obtaned after fast detector simulation. a- Correlation for the $t\bar{t}$ invariant mass spectrum reconstruction. b- Correlation for the $\cos\theta^*$ variable.

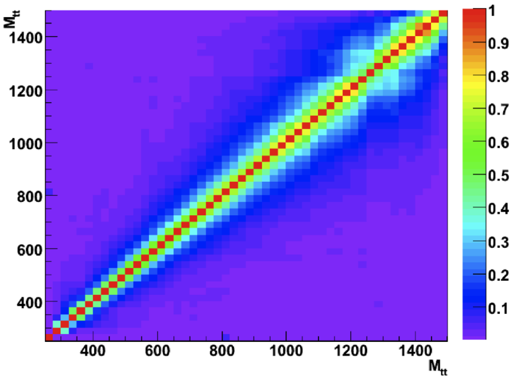

(a)

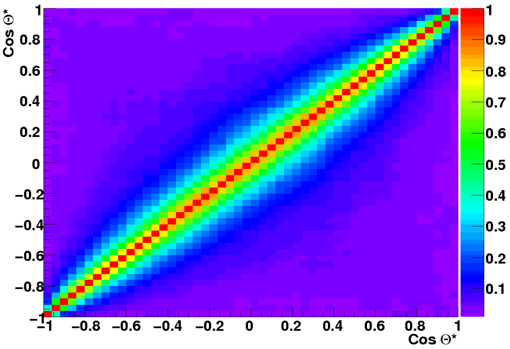

(b)

Element method is feasible at LHC to search for new resonances decaying in $t\bar{t}$.

Chapter 3

Search for a SM Higgs boson decaying to bottom quarks and produced in association with a Z^0.

The search for the 125 GeV SM scalar boson, decaying into b quarks, is of interest to test the consistency of the Brout-Englert-Higgs model of electroweak symmetry breaking. Currently, the newly discovered scalar is only found to decay at the LHC in final states with two bosons: 2 photons, 2 Z's, 2 W's. It is now crucial to see if the newly discovered boson also decays in a final state with fermions, e.g. $H \to bb$. Such a discovery would not only strengthen the consistency of the Brout-Englert-Higgs mechanism, but would also be a confirmation of the hypothesis that the newly discovered boson is not only responsible for the EW symmetry breaking mechanism, but also for the generation of the masses of elementary charged fermions.

The explored mass range covers $115 - 135$ GeV. The CMS collaboration performed these measurement in the channels $H \to \tau\tau$ [106] and $H \to b\bar{b}$ [37] [107]. At the LHC the main SM Higgs boson production mechanism is gluon fusion, as mentioned in Sec (1.2.4). However, in this production mode, the detection of the $H \to b\bar{b}$ decay is considered nearly impossible due to overwhelming dijet production expected from quantum-chromodynamic (QCD) interactions. Processes in which a low-mass Higgs boson is produced in association with a vector boson[108] have cross sections for proton proton collisions at a center of mass energy of 7 TeV of ≈ 0.57 pb and ≈ 0.31 pb computed at NNLO for WH and ZH, respectively [109]. Despite the low cross section they allow an easier identification of the signal.

The purpose of this work is to search for evidence of Standard Model Higgs boson decaying in $b\bar{b}$ using the Matrix Element Method (MEM). In order to study a clean channel the analysis focus on the associated Z^0 and H production discussed at sec.(1.2.2). So the topology of interest is then composed of two opposite charge and same flavor leptons and two b-jets in the final state.

This analysis has been performed with an integrated luminosity of 5.0 fb^{-1} of CMS certified data among the 5.55 fb^{-1} collected at center of mass energy of 7 TeV, during the 2011 proton-proton collision campaign as illustrated in Fig 3.1.

Figure 3.1 – Evolution of the LHC delivered and the CMS recorded luminosity during the 2011 proton-proton collision campaign.

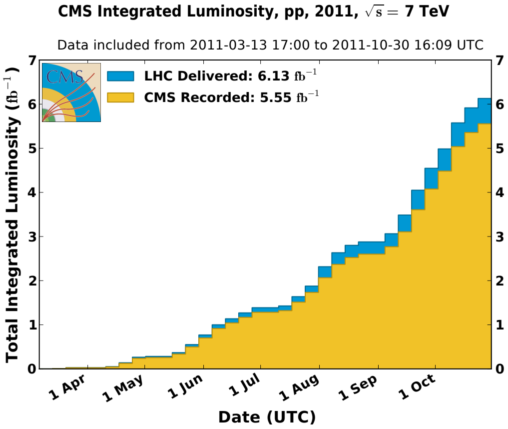

This analysis constitutes an independent cross-check of the main CMS analysis [37] and makes use of another methodology. The current CMS search analysis is based on a multivariate method. After a first level of selection, eleven kinematic variables are selected to train a Boosted Decision Tree using the TMVA framework [85].

The present analysis makes use of the Matrix Element Method The MEM used in this analysis will test hypotheses corresponding to all irreducible background and signal processes. [1]

As explained in Sec. (1.5), the MEM involves sophisticated integrals. These integrals will be evaluated by means of the MadWeight [89] software which provides a probability that a given event be produced according to a given hypothesis. This probability relies on the observed kinematics of the quasi stable particles of the event and the predictions from the MadGraph [79] event generatorSubsequently, the unnormalized probabilities (or so-called 'weights') are used in a multivariate analysis as discriminating observables. The shape of the discriminator between signal and background is finally used to estimate the significance of a (non-)discovery of a SM Higgs boson decaying into two b quarks in association with a Z^0 boson.

This chapter is organized as fellows. First, we present a measurement of the Z+bb cross section where our main contribution consisted to evaluate the $t\bar{t}$ background by means of the MEM. We present the various transfer functions used and the discriminative power of the method. The second section of this chapter is fully dedicated to the search for a Standard Model Higgs boson with an invariant mass around 125 GeV/c^2. The event selection is slightly modified but most of the material and expertise acquired for the cross section measurement is fully exploited. This is particularly relevant for critical systematical uncertainties such as those related to b-tagging, Jet energy scale and background estimate.

3.1 The Z(ll)bb final state

The main motivation to study the associated production of a Z vector boson decaying into two leptons and heavy flavor jets is to understand dominant process contributing to this final state. The Z+2b-jets process that is for example the main irreducible background for the searches for the associated production of a Z with a light Standard Model Higgs boson decaying to a pair of b-quarks.

Indeed, the measured production cross-section of Z bosons in association with two b-jets times the branching ratio of the Z decay to two leptons (electron or muon) is $\sigma_{Z(ll)bb}$ $0.36 \pm 0.01 \pm 0.07$ pb at 7 TeV at the LHC [110].

---

[1] The only irreducible background consists in the Z vector boson decaying into two leptons and produced in association with two b's. The Drell-Yan+jets where light flavor jets are mistag as b-jet are not considering as irreducible background.

while the predicted cross section for the associate H and Z production cross section times the branching ratio of the 125 GeV/c^2 Higgs boson decaying into a pair of b anti-b quark is of the order of 0.012 pb [38]

3.1.1 Event selection

The event selection criteria are based on the $Z(ll)bb$ cross-section measurement performed by CMS [110]. This dileptonic topology is characterized by the presence of b-jets, two oppositely charged leptons of the same flavor and no significant transverse missing energy. Signal events constitute a subset of a Drell-Yan sample simulated using MadGraph and Pythia. The various component of this sample are categorized according to the jet flavor at generator level as follow

- $Z+b$: Events with at least one b-quark produced at generator level inside acceptance.
- $Z+c$: Events that do not satisfy the $Z+b$ criteria but which contain at least one c-quark produced at generator level inside acceptance.
- $Z+l$: Events that do not satisfy $Z+b$ and $Z+c$ criteria inside acceptance.

A high purity $Z+b$ sample of events has been defined according to selection criteria presented in the following on the leptonic and the hadronic part of the event.

Lepton selection criteria

As previously said, events must contain two leptons either two electrons or two muons reconstructed using the particle flow algorithm. A minimal transverse momentum, $p_T > 20$ GeV is required on each of the two leptons in the event. In addition to that, the fiducial region is restricted to a pseudorapidity range $|\eta| < 2.4$. It is also required that the electrons in the gap region $1.442 < |\eta| < 1.566$, between ECAL barrel and ECAL endcap, are rejected. The two leptons coming from the decay of a Z boson can be identified by imposing isolation criteria. In order to ensure this the following requirement is applied on the muons (electrons); the ratio between the scalar sum of the transverse momentum of all the particle flow candidates within a cone of $\Delta R =< 0.4(0.3)$ and the p_T of the considered muon (electron) have to be lower than 0.2(0.15). The footprint of the lepton is removed from this sum.

The lepton isolation can be affected by multiple interactions per bunch-crossing (pile-up) producing extra energy deposit in the isolation cone. In order to deal with this, the leptons have to be associated to the same primary vertex. The charged particle entering in the computation of the isolation variable are filtered and rejected if they don't match the same primary vertex. The neutral contribution is instead extrapolated using the the charge hadron deposit or the information about the jet energy density and the number of primary vertices. [111].

The tables 3.2 summarizes the lepton selection criteria used in the analysis.

Table 3.1 – Selection requirements for particle-flow muons (electrons) [110].

Selection	requirement
p_T	> 20GeV
$\|\eta\|$	< 2.4
$\|\eta\|$ veto	$(1.442 < \|\eta\| < 1.566)$
PF$_{iso}$ $\Delta R < 0.4$ (0.3)	< 0.2 (0.15)
Trigger Matching	$\Delta R < 0.3$ and $\Delta P_t/P_t < 0.5$

In order to select events containing Z^0 candidate, the dileptonic invariant mass is required to be in the range of 76 GeV $< M_{l^+l^-} <$ 106 GeV. If more than two leptons satisfy this requirement the selected ones are those providing the best Z^0 candidate having the mass the closest to 91 GeV.

Jet and Missing Transverse Energy requirements

The hadronic component of the event has also to satisfy some criteria used to define the phase space of the cross-section measurment. The reconstructed jets are required to have a minimal transverse momentum of $p_T > 25$ GeV and have to be separated from each of the selected leptons by at least $\Delta R(l,j) > 0.5$. Furthermore, the selected jets are required to be inside the pseudorapidity region,$|\eta| < 2.1$, to ensure optimal b-tagging performance. The b-tagging technique exploits an algorithm based on the secondary vertex mass distribution, see Sec.(1.3.6) and the considered b-tagged jets have to satisfy the requirements of the High Efficiency working point.

Then in order to suppress the $t\bar{t}$ background, for the Z+2b-jets sample only, a cut on the significance of the missing transverse energy (E_T^{miss}) is applied.

Table 3.2 – Selection requirement for particle-flow Jets and E_T^{miss} [110].

Variable	requirement
p_T	> 25 GeV
$\|\eta\|$	< 2.1
Lepton isolation	$\Delta R(jet - lept) > 0.5$
B-tagging	SSV HE working point
E_T^{miss}	MeT significance< 10

Correction factors

In order to match the data, the simulated event sample has been rescaled according to the leptons and b-tagging efficiencies and reweighted according to the Pile-Up distribution. These scale factors have been estimated as detailed in [110]. All results presented in this chapter have been obtained after application of these corrections factors.

Pile-up reweighting: Pile-Up condition vary for each data taking period while simulated event samples are generated assuming a distribution of the number of Pile-Up events that approximately cover what is observed in the data.

Therefore, the simulated events are reweighted according to the Pile-Up distribution in order to match to the data. The correction reweighting adjusts the generated Pile-Up distribution of the simulated events to the equivalent quantity in the data. The number of Pile-Up event in the data sample is extracted using the proton proton inelastic scattering cross section combined with the instantaneous luminosity per bunch crossing for each luminosity section. The distribution of the number of Pile Up event corresponding to the data run considered in the analysis is showed in Fig 3.2, which present an agreement between data and reweighted simulated events. However, this distribution is not well modeled by the simulated events for the high number of Pile Up event.

Lepton scale factor: Physics object reconstruction is affected by its intrinsic efficiency that have to be carefully estimated. The efficiency to select a lepton, electron or muon, according to the selection criteria of the analysis has been estimated for simulated events and 2011 data. Leptons efficiencies has been estimated using a data-driven technique, the so called Tag and Probe method [112]. This method allows to obtain almost unbiased estimates of the efficiencies of the different steps of lepton offline reconstruction. According to the lepton momentum range considered by the analysis (here $p_T > 20$ GeV), a

Figure 3.2 – Vertex multiplicity after Pile-Up reweighting of the Monte-Carlo events compared to the data distribution. This comparison is done a Z+jet selection level.

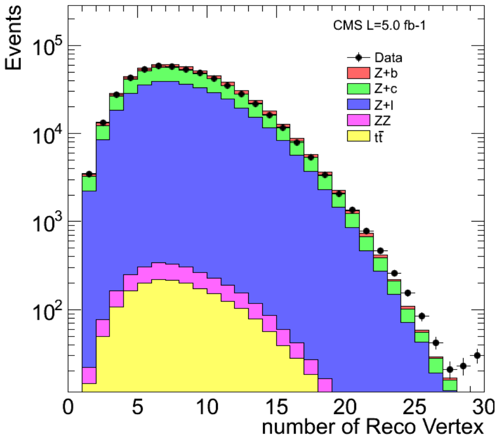

selection of events with two leptons peaking at the Z mass is performed. Tight requirement are applied on one of the lepton called *tag* while a loose selection on the second one called the *probe*. The efficiency is estimated by looking at the fraction of probe that satisfy the requirement of the offline selection performed in the analysis. The selection of the probe lepton has to be loose enough in order ton not bias the efficiency estimation.

The scale factor estimated by tag-and-probe for the reconstruction and isolation are convoluted with the trigger efficiency to obtain a "per-event" scale factor.

This is the probability that a lepton, selected with the analysis criteria fired one of the triggers applied in the analysis. The lepton efficiency for simulated event is assumed to be 100%, therefore the correction is performed by reweighting the simulated events for data efficiency only.

For muons, the efficiency for the unprescaled high level trigger used in this analysis have been estimated on the full 2011 dataset. The total efficiency for the various considered trigger has been computed and has been found to vary as a function of η of the muon, therefore efficiencies for distinct regions have been evaluated. For the 2011 period the unprescaled single muon trigger p_T threshold changes (from 7 and 8 GeV to 13 and 8 GeV). The estimated efficiency is above 90% whatever is the η region.

The HLT trigger efficiency for the electron channel has been also extracted from the full 2011 dataset. It has been found to be close to 100% for electrons with Pt larger than 20 GeV through the entire ECAL fiducial region. The trigger efficiency estimation have been done for the two 2011 data taking period separately as the HLT considered during the 2011A campaign has been prescaled for 2011B.

Simulated events are reweighted according to the per lepton scale factors defined as the ratio between data and simulation efficiency, as a function of their p_T and η. At this point a better agreement between data and Monte-Carlo is expected on the main lepton kinematic variables distributions. This is illustrated by the distribution of the reconstructed Z peak in both dielectron and dimuon channel shown in Fig. 3.3. The simulated events contribution have been normalized according to theory predictions, a small excess of data is observed in the dimuon channel.

Figure 3.3 – Dileptonic invariant mass distribution for CMS 2011 data ($5.0 fb^{-1}$) after requirement of all selection criteria and application of correction scale factor. Left: Dimuon channel. Right: Dielectron channel.

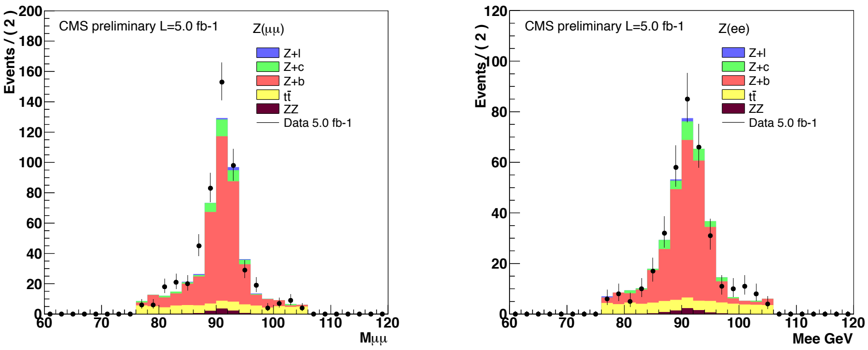

B-tag scale factor:

In addition to the Pile-Up reweighting and to the leptons selection efficiency correction, reweighting factor correcting for the b-jet identification efficiency are needed. These scale factors are applied to simulated events in order to account for the b-tagging or mistag efficiencies. The evolution of the b-tagging efficiencies with respect to the jet p_T are illustrated by the Fig 3.4 for two regions of pseudorapidity for the b-tagging algorithm used and the working point considered.

Figure 3.4 – SSVHE MC efficiencies. Top: ϵ_{MC} as a function of Pt of the jet in the central $|\eta| < 1.2$(left) and forward $1.2 < |\eta| < 2.4$ (right) regions. Markers denote the values computed using the Z+b/c Madgraph MC sample, overlaid is the line corresponding to the ϵ_{MC} of the QCD sample used [113]

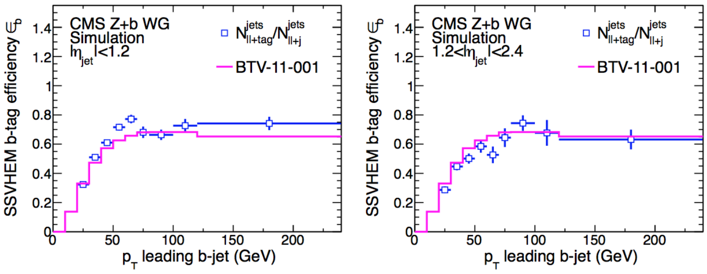

These scale factors can then be used to estimate the efficiency of a specific selection. Scale factors for c-jets, defined as the ratio of ϵdata/ϵMC, are assumed to be the same as for b-jets.

Data and Monte-Carlo yields and control plots.

The different simulated events samples, used to estimate the background, are normalized with respect to the cross sections expected from theory. The inclusive cross sections related to the considered simulated events which are used are: 3048 pb for the DY+jets sample and 157.5 pb for the $t\bar{t}$ +jets sample. The ZZ component has been normalized according to the corresponding production cross-section measured by the CMS collaboration,

$6.24^{+0.86}_{-0.80}$ pb$_{(stat.)}$ $^{+0.41}_{-0.32}$ pb$_{(syst.)}$ ± 0.14 pb$_{(lumi.)}$ [114]. As already said, all simulated sample have been reweighted to taken into account mismodelling of pile-up events, p tagging and lepton reconstruction efficiencies. The sets of data used in this analysis are listed in appendix (B.2). The data yields as well as the expected yields are summarized in Table 3.3.

These yields present a small excess in data in the dimuon channel. Despite the acceptable agreement between data and Monte-Carlo, to quantify properly the background fraction a data driven technique has been considered. Using the secondary vertex mass distribution [110] or the invariant mass spectrum of the dileptonic system, template fit of the simulated events to data have been performed to estimate the fraction of correctly tagged b jets are transformed into an event purity ($P_b^{Z+1,2b}$) of events containing one or two truly b-flavored

Table 3.3 – The data yields for the different selections, and a comparison with the expectation from different sources based on Monte Carlo simulation. The expectated yields are normalised with respect to the theoretical predictions, uncertainties are statistical only.

Selection	Data	MC-tot	Zb	Zc	Zl	tt	ZZ
Z($\mu\mu$)+2b-jets	522	480 ± 13	350 ± 12	34 ± 4	5 ± 1	80 ± 1	12 ± 1
Z(ee)+2b-jets	362	357 ± 11	258 ± 10	27 ± 3	2 ± 1	62 ± 1	8 ± 1

jets and the $t\bar{t}$ fraction respectively. However this work focuses only on the $t\bar{t}$ fraction estimation.

Despite a general good agreement between data and simulated events, tension in the shape of the distribution of the p_T of the vector boson has been observed.The spectrum is harder for the data than what is predicted by the simulation as illustrated in Fig. 3.5. This might come from a mis-modeling of the kinematic of the $Zb\bar{b}$ events selected from a Drell-Yan+jets sample generated by MadGraph [79] with a five flavor scheme [115] assuming massless b-quark.

Figure 3.5 – Discrepancy in the P_{tZ} spectrum of Z+b events at 'Z+HEHE+METsig' selection working point of the Z+2b cross section measuremnt analysis according to selection [110]. The spectrum is harder for data than for the M.C.

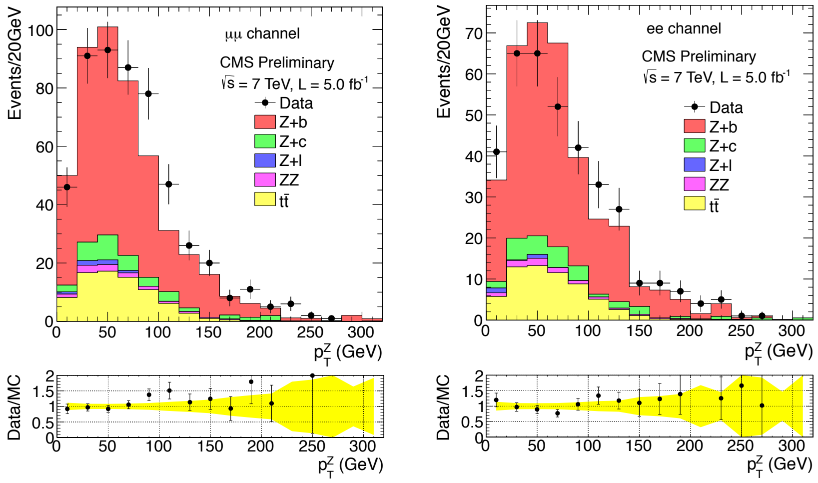

Next to leading order Monte-Carlo prediction obtained with aMC@NLO [116] show indeed a harder spectrum than the LO prediction [117].

3.1.2 Discrimination with Matrix element method

A technique to discriminate signal and background processes consists to use the Matrix Element method. This approach is able to provide a per event probability of arising from a particular process. The most common technique used in searches consists of looking at the ratio [118]: $\frac{\mathcal{P}_{S+B}}{\mathcal{P}_B}$ where P_S represent the probability for the signal hypothesis while P_B the probability for the background hypothesis [5].

This work presents an alternative approach in which the normalization to get a probability is not required. this quantity is then called weight in this presentation,

$$W = \sigma.\mathcal{P}. \tag{3.1}$$

Where σ and $\mathcal{P}$ are defined by Eq. 1.35. The discrimination between signal and background is then based on the shape of the weight distribution.

After the selection criteria, described Sec (3.1.1), the $t\bar{t}$ production decaying in the fully leptonic channel remains the most important background for a Z+bb signal search. In order to estimate this background, the probabilities that an event is produced according to $t\bar{t}$ or Z+bb leading order matrix element is evaluated.

The $Z(ll)b\bar{b}$ topology has as particularity that all the final state particles are observable in the detector. The evaluation of the Matrix Element weights according to such an hypothesis leads to solve an over-constraint system. This is not the case in the $t\bar{t}$ hypothesis where neutrinos are not detected. The assumption that a Z boson decays into two leptons is an important constraint on the dilepton system. Due to the not ideal reconstruction of the leptons, it implies that δ function can not be assumed as transfer function.

As the $Z(ll)b\bar{b}$ hypothesis is over-constrained there is not freedom to absorb a possible violation of the energy momentum conservation principle. This implies that the correction for the transverse boost due to the presence of initial state radiation is mandatory. It has been checked that without considering any ISR correction, the computation of the Matrix Element weights sometimes failed. It is due to the not convergence of the numerical integration. However the numerical integration converges for all events that are tested with the correct Matrix Element hypothesis, e.g. for Drell-Yan events under the Drell-Yan hypothesis or for $t\bar{t}$ events under the $t\bar{t}$ hypothesis.

As no neutrino leading to real missing energy is involved at leading order, it is assumed that the transverse momentum of the potential extra radiation has to be deduced from the visible final state only. This assumption implies that the observe transverse missing energy results from the energy resolution on the measured particles. So the ISR transverse boost discussed in previous chapter and expressed by Eq. 2.21 can be simplified to become

$$\vec{P}t_{boost} = -\sum_{ISR} \vec{P}t = \sum_{reducedFinalState} \vec{P}t. \tag{3.2}$$

3.1.3 Transfer function

As discussed in Sec.(2.2.1) transfer functions constitute an important input in the weights computation. For the 2011 data analysis the jet energy transfer function have been updated from what has been presented in the previous chapter. While transfer functions for the lepton energy have also been estimated. Concerning the direction variables (η and ϕ), perfect measurement has been assumed for both jets and leptons, implying the use of δ function as transfer function for these quantities.

Jets energy transfer function: The jets energy transfer function is estimated from a high statistic sample consisting of pairs of b-parton, b-jets extracted from $t\bar{t}$ and Drell-yan $+b$. The parton-jet pairing is obtained by requiring that the maximal distance in the $\eta - \phi$ plane (Δ_R) between the parton and the reconstructed jet be less than 0.3.

The jet energy reconstruction resolution is not uniform on all the pseudo-rapidity range covered by the CMS detector. Therefore, the energy transfer function has been divided into two. The "central" region $0 > |\eta|_{jet} < 1.6$ and the "forward" region which covers $1.6 > |\eta|_{jet} < 2.4$. Both transfer functions are parametrized as double gaussian (Eq 2.6). The five parameters a_i depend on the b-parton energy follow

$$a_i = a_{i,0} + a_{i,1}E + a_{i,2}\sqrt(E), \tag{3.3}$$

up to fifteen parameters for both transfer functions are being adjusted by the fitting program. This parametric form is motivated by the calorimeter energy resolution formula, Eq. 1.28. They are estimated by an un-binned likelihood fit as presented in the Sec.(2.2.1). The extracted values of the parameters are presented in Table 3.4 for the jets in the central region and in Table 3.5 for the jets reconstructed in the forward-backward (FB) region. The transfer functions have been estimated only for b-jets. A quality check of the parameters is done comparing the projections of $\delta E = E - E^{vis}$ for four different ranges of b parton energy, which are shown in Fig. 3.6.

Electron energy transfer function: Dielectron final states are considered and energy transfer functions for both leptons have been estimated. As for the b-jets, the electron energy transfer function have been also parametrized by a double gaussian. Two regions in η have also been defined for the electron-energy transfer functions. Fitted parameters are summarized in Table 3.6 for the electrons in the central region and in Table 3.7 for the electrons reconstructed in the FB region. Transfer functions for electrons are shown in Fig.3.7 for different energy ranges (at generator level).

Muon transfer function has been parametrized as function of $\frac{1}{p_T}$ instead of the energy. It is motivated by the fact that muons reconstruction is driven by the tracking and muons chamber systems in contrast to the jets or electron for which the measurement of the energy is driven by the deposits in the calorimeters.Therefore, the transverse momentum resolution mainly comes from the uncertainty on the Sagitta of the muon track. However the parametrization remains the same such that Eq. (2.6) becomes

$$W^{\frac{1}{p_T}}(\frac{1}{p_T}, \frac{1}{p_T^{vis}}) = \frac{1}{\sqrt{2\pi}(a_2 + a_3 a_5)}[e^{-\frac{(\frac{1}{p_T} - \frac{1}{p_T^{vis}} - a1)^2}{2a_2^2}} + a_3 e^{\frac{(\frac{1}{p_T} - \frac{1}{p_T^{vis}} - a4)^2}{2a_5^2}}].(3.4)$$

Unlike the jets and electrons, the muon transfer function has not been divided into several pseudo-rapidity region. Up to fifteen parameters have been extracted using the same approach as for electrons and b-jets. These parameters are presented in Table 3.8 while the control plots for four different windows in p_T presented in Fig. 3.8, show an acceptable level of agreement.

Table 3.4 – Parameters of the jet-energy transfer functions extracted by maximizing unbinned likelihood fits for jets in the central region, $0 < |\eta| < 1.6$. The jet-parton pairs have been associated by a matching in $\Delta R < 0.3$. Particle flow jets reconstructed with the anti-Kt 5 algorithm are used.

Type	independent term	E	$\sqrt(E)$
μ first gaussian	$a_{10} = 1.05 \pm 0.01$	$a_{11} = -0.021 \pm 0.001$	$a_{12} = 0.0$
σ first gaussian	$a_{20} = 0.0$	$a_{21} = 0.037 \pm 0.003$	$a_{22} = 0.83 \pm 0.02$
ratio	$a_{30} = 0.0$	$a_{31} = 1.23 \times 10^{-3} \pm 3 \times 10^{-5}$	$a_{32} = 1.0 \times 10^{-3} \pm 2. \times 10^{-4}$
μ second gaussian	$a_{40} = 5.02 \pm 0.04$	$a_{41} = 0.0$	$a_{42} = 2.4 \pm 0.34$
σ second gaussian	$a_{50} = 0.0$	$a_{51} = 0.05 \pm 0.01$	$a_{50} = 0.93 \pm 0.03$

Table 3.5 – Parameters of the jet-energy transfer functions extracted by maximizing unbinned likelihood fits for jets in the central region, $1.6 < |\eta| < 2.4$. The jet-parton pairs have been associated by a matching in $\Delta R < 0.3$. Particle flow jets reconstructed with the anti-Kt 5 algorithm are used.

Type	independent term	E	$\sqrt(E)$
μ first gaussian	$a_{10} = 3.4 \pm 0.01$	$a_{11} = -0.021 \pm 0.002$	$a_{12} = 0.0$
σ first gaussian	$a_{20} = 0.0$	$a_{21} = 0.04 \pm 0.01$	$a_{22} = 0.88 \pm 0.03$
ratio	$a_{30} = 0.0$	$a_{31} = 3.9 \times 10^{-4} \pm 5 \times 10^{-5}$	$a_{32} = 3.0 \times 10^{-3} \pm 4. \times 10^{-4}$
μ second gaussian	$a_{40} = 5.01 \pm 0.05$	$a_{41} = 2.9 \pm 0.2$	$a_{42} = 0.0$
σ second gaussian	$a_{50} = 0.0$	$a_{51} = 0.15 \pm 0.03$	$a_{50} = 0.91 \pm 0.04$

Figure 3.6 – Projection of $\delta E = E - E^{vis}$ for different ranges in energy for jets. The black curve represents the distribution obtained by associating the generated partons with the reconstructed jets for events simulated using MadGraph. The blue (continuous) curve corresponds to the transfer function. The curves are normalized to unity. The four plots on the top have been obtained for central jets, $|\eta| < 1.6$, while the four plots on the bottom have been obtained for jets in the forward-backward region, $|\eta| > 1.6$.

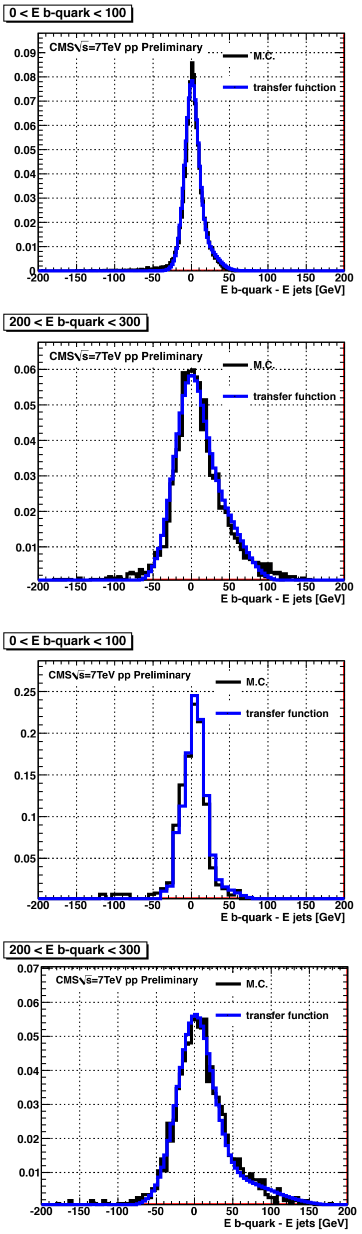

Table 3.6 – Parameters of the electron-energy transfer function extracted by maximizing an unbinned likelihood fit for electrons in the central region, $0 < |\eta| < 1.5$.

Type	independent term	E	$\sqrt(E)$
μ first gaussian	$a_{10} = -0.2 \pm 0.04$	$a_{11} = 1.05 \times 10^{-3} \pm 4 \times 10^{-5}$	$a_{12} = 0.0$
σ first gaussian	$a_{20} = 0.3 \pm 0.02$	$a_{21} = 5.1 \times 10^{-4} \pm 2 \times 10^{-5}$	$a_{22} = 0.12 \pm 0.02$
ratio	$a_{30} = 0.0$	$a_{31} = 0.0012 \pm 0.0003$	$a_{32} = 0.018 \pm 0.001$
μ second gaussian	$a_{40} = 2.0 \pm 0.34$	$a_{41} = 0.013 \pm 0.002$	$a_{42} = 0.01 \pm 0.003$
σ second gaussian	$a_{50} = 0.0$	$a_{51} = 0.032 \pm 0.0045$	$a_{50} = 0.0$

Table 3.7 – Parameters of the electron-energy transfer function extracted by maximizing an unbinned likelihood fit for electrons in the forward-backward region, $1.5 < |\eta| < 2.4$.

Type	independent term	E	$\sqrt(E)$
μ first gaussian	$a_{10} = -1.9 \pm 0.01$	$a_{11} = 0.0011 \pm 0.0001$	$a_{12} = 0.0$
σ first gaussian	$a_{20} = 2.3 \pm 0.04$	$a_{21} = 0.0066 \pm 0.0003$	$a_{22} = 0.055 \pm 0.002$
ratio	$a_{30} = 0.0$	$a_{31} = 8.9 \times 10^{-4} \pm 6 \times 10^{-5}$	$a_{32} = 0.014 \pm 0.003$
μ second gaussian	$a_{40} = 5 \pm 0.5$	$a_{41} = 0.013 \pm 0.003$	$a_{42} = 0.11 \pm 0.02$
σ second gaussian	$a_{50} = 0.0$	$a_{51} = 0.035 \pm 0.004$	$a_{50} = 0.032 \pm 0.004$

Figure 3.7 – Projection of $\delta E = E - E^{vis}$ for different ranges in energy for electrons. The black curve represents the difference between the generated and reconstructed energy. The blue curve corresponds to the transfer function. Both are normalized to unity. The four top plots represent the central region $|\eta| < 1.5$ and the four bottom plots are for the forward-backward region $|\eta| > 1.5$.

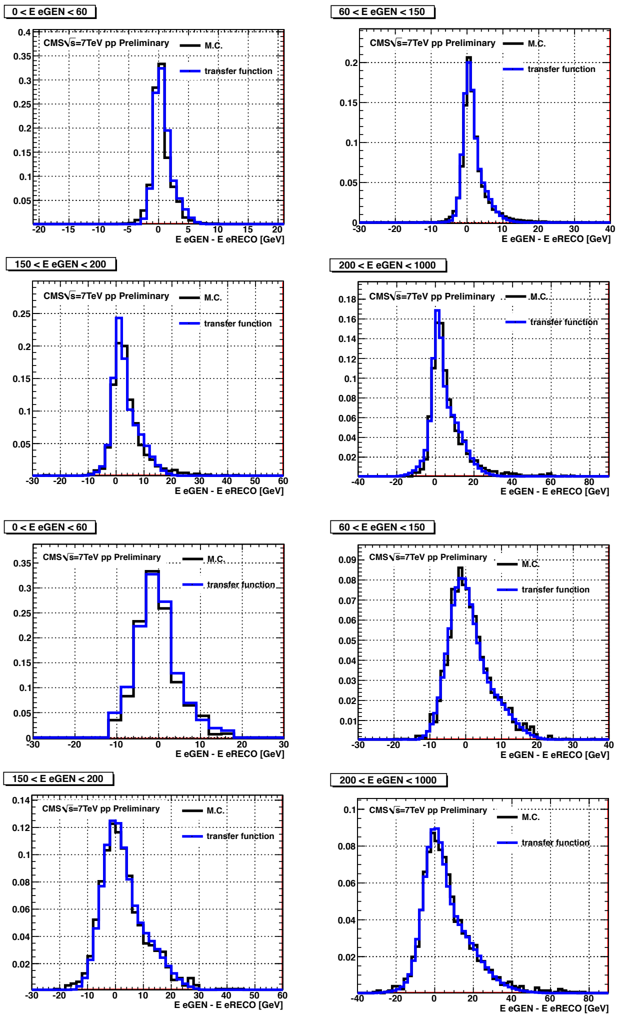

Table 3.8 – Parameters of the muon transfer function extracted by maximizing an unbinned likelihood fit for muons in the acceptance. A double gaussia parametrization is assumed as for the electron energy and jet energy transfer function. However muon tranfer function is parametrized in term of $\frac{1}{P_t}$ instead of energy since the muon reconstruction is driven its full track reconstruction providing information on the transverse momentum.

Type	independent term	$1/p_T$	$\sqrt(p_T)$
μ first gaussian	$a_{10} = -1.89e-04 \pm 1.0e-06$	$a_{11} = 1.87e-06 \pm 8.3e-07$	$a_{12} = 0.0$
σ first gaussian	$a_{20} = 0.0$	$a_{21} = 0.0$	$a_{22} = 2.9995e-03 \pm 7.52e-08$
ratio	$a_{30} = 0.0$	$a_{31} = 4.9e-02 \pm 1.38e-03$	$a_{32} = 0.0$
μ second gaussian	$a_{40} = -1.09e-03 \pm 1.49e-04$	$a_{41} = 0.0$	$a_{42} = 4.9888e-01 \pm 1.02e-04$
σ second gaussian	$a_{50} = 1.69e-03 \pm 1.49e-04$	$a_{51} = 0.0$	$a_{50} = 0.0$

Figure 3.8 – Projection of $\delta\frac{1}{Pt} = \frac{1}{Pt} - \frac{1}{Pt^{vis}}$ for different range in Pt for muons. The black curve shows the distribution obtained from the difference between the generated and the reconstructed inverse transverse momenta. The blue (continuous) curve corresponds to the transfer function. The curves are normalized to unity.

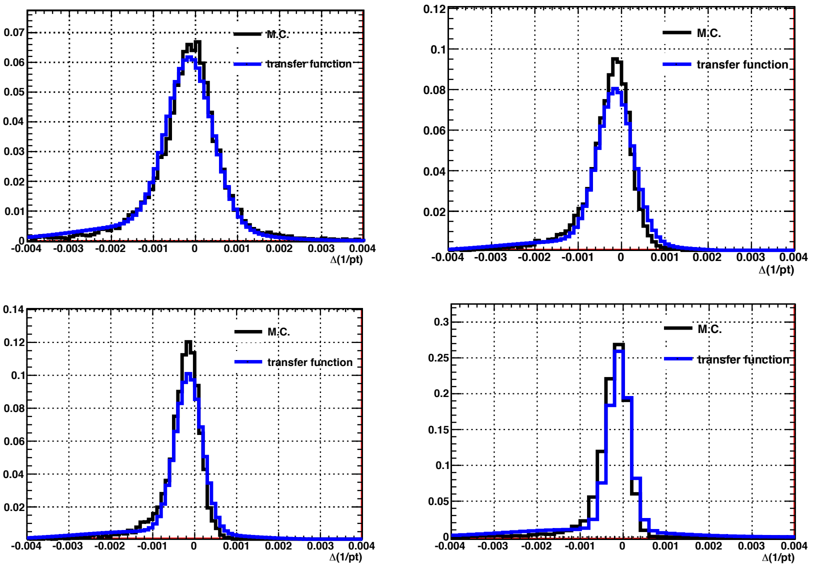

3.1.4 Discriminant variables for $Z(ll)$+$b\bar{b}$ vs $t\bar{t}$.

There are two obvious quantities generally considered to discriminate $t\bar{t}$ and DY events: the dileptonic invariant mass and the transverse missing energy or its significance.

In the context of the $Z(ll) + bb$ cross-section measurement, the MEM is used to provide a discriminant variable between the signal and the $t\bar{t}$ contamination. This method is used as a cross check analysis of the estimation of the $t\bar{t}$ contamination.

Considering the full selection of the Z(ll)bb analysis, for all the simulated datasets and for the data, weights have been evaluated according to hypothesis: Z(ll)b$\bar{b}$, or $t\bar{t}$ decaying in the fully leptonic channel. Concerning the Z(ll)$b\bar{b}$ hypothesis, two weights have been computed. Indeed the tree-level Matrix Element allows to evaluate the weights independently for the non interfering processes at leading order. One weight is computed according to the

$q\bar{q}$ production channel while a second weight assume two gluons as incoming partons. Figure 3.9 represents the weight distributions for $t\bar{t}$ dileptonic event and Z$b\bar{b}$ event for both electrons and muons channel. As shown in Fig 3.9, these quantities can be used as discriminants variables.

Figure 3.9 – Distribution of the $-Log_{10}$ of the weights for Drell-Yan and $t\bar{t}$ events in the dielectron channel. - Top Left: $gg \to Z(e^+e^-)b\bar{b}$ hypothesis. - Middle top: $qq \to Z(e^+e^-)b\bar{b}$ hypothesis. For theses two matrix elements the correction for the transverse boost is evaluated only with the visible particles. - Top Right : $t\bar{t}$ hypothesis, the boost correction uses the missing transverse energy information. Bottom plots represent the same discrimination in the dimuon channel.

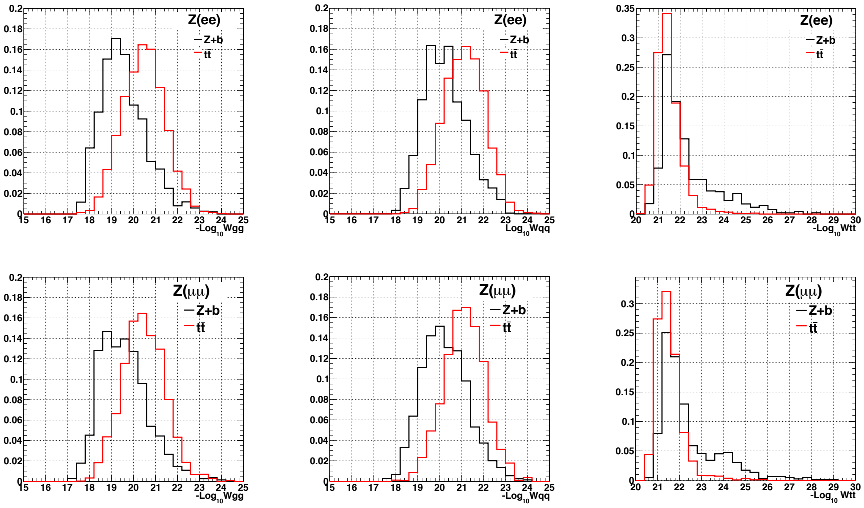

Since Fig 3.9 shows $-Log_{10}$ of the weight, higher Matrix Element weights correspond to lower value of the x-axis. As expected, $t\bar{t}$ events have lower weights than the Drell-Yan+jets ones for the $Z(ll) + bb$ hypothesis, and they present higher weights with the $t\bar{t}$ hypothesis. Moreover, signal and background distributions don't peak at the same place for the two Zbb hypothesis, there is therefore a small added value by using them both. There is also a difference of shape of the $t\bar{t}$ weight distribution between $t\bar{t}$ and Drell-Yan+jets which presents a larger tail. All these weights have been used in order to built a discriminant quantity between signal and background.

These three Matrix Element hypothesis have also been tested on the ZZ events and on all the selected data events. The agreement between Data and Monte-Carlo is represented in Fig 3.10.

Figure 3.10 – Distribution of the Log_{10} of the Matrix Element weights evaluated according to $q\bar{q} \rightarrow Zb\bar{b}$, $gg \rightarrow Zb\bar{b}$ and $t\bar{t}$ hypothesis for the 5 fb^{-1} of events selected according to the selection of the $Zb\bar{b}$ cross-section measurement [110]. Top: Dielectron channel, bottom: dimuon channel.

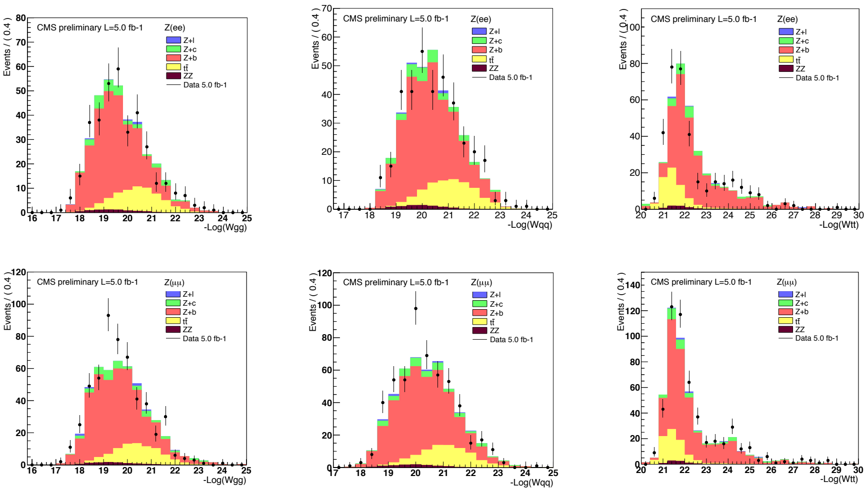

Stability with respect to transfer function: In order to see the impact of the quality of the fit of the various parameters used in the transfer functions, we have varied the width of the main narrow gaussian by a factor of two. All weights have then been recalculated with theses degraded transfer functions and the ratio between the new and old weights has been calculated on an event by event basis for both $t\bar{t}$ and Drell-Yan+jets samples.

The central values are all compatible with one while the root mean square of the distribution stays below 1%. The table 3.9 summarized the RMS of the obtained results for the jet energy and lepton energy transfer function. The stability obtained with such a drastic modifications has a relatively small impact on the $-Log_{10}$ of the Matrix Element weights. This study does not allow to precisely impact the systematic uncertainties related to jet energy scale or even jet energy resolution on the final discriminant used to discriminate the two processes. It is however very encouraging and it shows that the goodness of the fit of parameters used in the transfer function is not critical.

Table 3.9 – Peak position and RMS of distribution of the ratio $Log_{10}(W)/Log_{10}(W*)$ where W and $W*$ are the Matrix Element weight estimated with the nominal set of transfer function and with the modified ($a_2 \rightarrow 2 \times a_2$) one respectively. The are the quantities considered in the analysis. Variation done for the different M.E. hypothesis for both $t\bar{t}$ and $Zb\bar{b}$ sample.

Sample		$t\bar{t}$	qqToZ(ee)bb	ggToZ(ee)bb
Jet energy TF variations				
$t\bar{t}$	RMS	$8.8\ 10^{-3} \pm 2\ 10^{-4}$	$5.2\ 10^{-4} \pm 1.2\ 10^{-5}$	$5.8\ 10^{-4} \pm 1.3\ 10^{-5}$
	peak	1.00	0.99	1.00
Z(ee)$b\bar{b}$	RMS	$1.153\ 10^{-4} \pm 3\ 10^{-4}$	$5.1\ 10^{-4} \pm 1.5\ 10^{-5}$	$6.4\ 10^{-4} \pm 1.8\ 10^{-5}$
	peak	1.004	0.99	0.99
Electron energy TF variations				
$t\bar{t}$	RMS	$7.6\ 10^{-4} \pm 2\ 10^{-5}$	$6.8\ 10^{-3} \pm 1\ 10^{-4}$	$7.3\ 10^{-3} \pm 2\ 10^{-4}$
	peak	1.001	1.003	1.004
Z(ee)$b\bar{b}$	RMS	$1.310{-}3 \pm 1\ 10{-}4$	$6.4\ 10^{-3} \pm 510^{-5}$	$6.7\ 10^{-3} \pm 2\ 10^{-4}$
	peak	1.00	0.99	0.99

3.1.5 Final $t\bar{t}$ vs Zbb discriminant.

The weights presented in the previous section constitute a set of variables that can be used to distinguish between different processes. In this section, these weights are used as inputs to a multivariate discriminator to separate Z$b\bar{b}$ and $t\bar{t}$ events. A multilayer perceptron artificial neural network is used for this purpose. Additional kinematical variables can also be used as inputs, concretely the possibility of including the E_T^{miss} as an input variable is explored. This method requires a relatively large amount of simulated events in order to train correctly the neural network. Neural networks discriminants presented in this analysis are probably not the optimal results that can be obtained with this method due to the limited available statistics. Moreover, the training is performed using only simulated events in the ee channel, while the obtained discriminator is used both for the ee and $\mu\mu$ channels. A similar discrimination is expected in both cases, as the shapes of the the considered weights are very similar for the two channels.

The multilayer perceptron: The multilayer perceptron is a simple feed-forward network with a structure as represented in Fig 3.11. Each layer ”l” is composed of N_l nodes linked to the previous layer by $N_l \times N_{l-1}$ connections called synapses. The purpose consist to define a non linear discriminative function. The perceptron can be trained on a set of examples using a special learning rule. The perceptron weights are changed in proportion to the difference (error) between the target (correct) output, Y, and the perceptron solution, y, for each example.

Figure 3.11 – Schematic representaion of the structure of a multilayer perceptron. There are n input variables (x_i), several layer composed of various number of nodes characterized by a sigmoid function applied on its input. Each of the node is linked to all the node of the previous and the following layer and each link is characterized by a weight. Finaly that converge to the output variable.

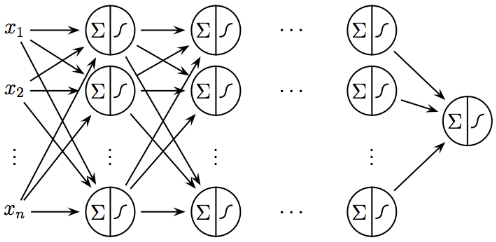

Synapse between the node j of layer l and the node i of the layer $(l-1)$ corresponds to a weight w_{ij}^{l}. Denoting x_i^{l-1} the output of a node i associated to layer $(l-1)$, ξ_j^l is expressed as $\xi_j^l = \sum_{i=l}^{N_{l-1}} w_{ij}^l x_i^{l-1}$. The transformation associated to each node j, $x_i^l = \sigma(\xi_i^l)$ is a sigmoid function,

$$\sigma(\xi) = \frac{1}{1+e^{-\xi}}, \tag{3.5}$$

acting on the set of nodes input ξ_j.

A learning rule defines how exactly the network weights should be adjusted (updated) between successive training cycles called epochs. The aim of the learning methods is to minimize the total error on a set of weighted examples. The set of input variables is denoted $\vec{x}$. The error is estimated according to

$$\epsilon^2 = \int (N(\vec{x}) - T_B(\vec{x}))^2 P_B(\vec{x}) d\vec{x} + \int (N(\vec{x}) - T_S(\vec{x}))^2 P_S(\vec{x}) d\vec{x}, \tag{3.6}$$

where $N(\vec{x})$ represents the neural network value, $T(\vec{x})$ is the target value (0 for the background and 1 for the background) and $P_{S(B)}(\vec{x})d\vec{x}$ represents the *pdf* for the signal (background).

$$\epsilon^2 = \frac{\sum_{i=1}^{N}(N(x_i) - T(x_i))^2}{N} \tag{3.7}$$

The learning method is based on the back-propagation of the errors principle. A loop over all examples is called an epoch. The weights are updated after each example according to the formula:

$$w_{ij}(t+1) = w_{ij}(t) + \Delta w_{ij}(t) \tag{3.8}$$

where $\Delta w_{ij}(t)$ can be estimated by several techniques. The Broyden-Fletcher-Goldfarb-Shanno (BFGS) algorithm [119] is the one used in the considered multilayer perceptron (MLP). All these techniques have the same purpose of minimizing the error Eq. 3.7.

The Drell-Yan+jet - $t\bar{t}$ discriminant: The output of the the neural network is fixed to 0 for tt events and 1 for Zbb during the training. For both processes, the simulated events are divided to define training and test samples, containing each of them 50% of the events of the available samples. Both dataset are used with an equivalent weight. A structure of the multilayer perceptron and an example of learning are represented in Fig 3.12. The width of the link between the different nodes represent the weight associated to the corresponding synapse.

The transverse missing energy is used only to compute the ISR transverse boost correction in the context of the Matrix Element testing the $t\bar{t}$ hypothesis. The E_T^{miss} is not directly used in the Matrix Element weight estimation. Because of that, in order to verify if this variable brings some discrimination, two neural networks discriminant have been trained. The first one used as input the three Matrix Element weights corresponding to each process hypothesis only while the second neural network consider the transverse missing energy as an input as well.

The use of the E_T^{miss} modify the separation power of the neural network improving the performances. This is illustrated in Fig 3.13(a), which is obtained scanning the cut on the neural network outputs. The efficiency selecting $Z(ll)b\bar{b}$ events versus the one selecting $t\bar{t}$ events is shown there for both neural networks. The separation between the two considered processes is illustrated in

Figure 3.12 – Left: Learning curve of a neural network trained to discriminate $t\bar{t}$ and $Zb\bar{b}$ events. For both processes, the training and test samples contain approximately the same numbe events. - Right: Structure of the neural network used to discriminate $t\bar{t}$ and $Zb\bar{b}$ events.

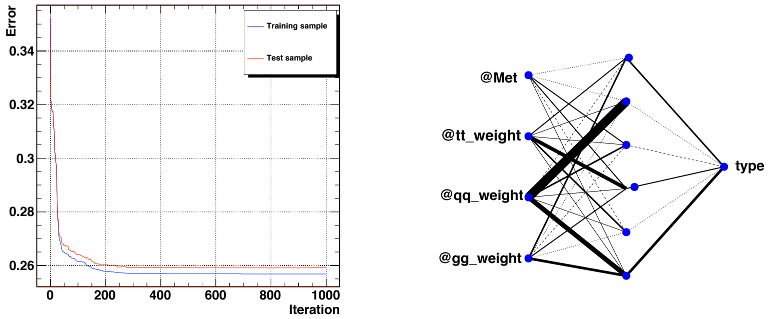

(a) (b)

Figure 3.13 – Left: $Z(ll)b\bar{b}$ versus $t\bar{t}$ selection efficiencies estimated acording to three quantities which are: the E_T^{miss} distribution, a neural network that uses the matrix element weights and the E_T^{miss} and one NN based on the matrix element weights only. - Right: Neural network discriminant, using the matrix element weight, for $t\bar{t}$ and D-Y sample. Both sample are normalized to 1.

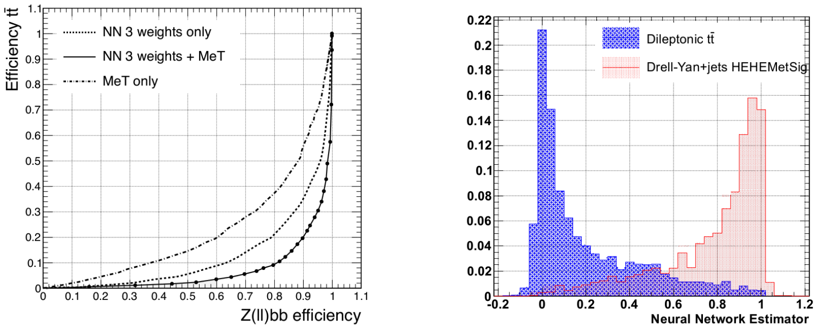

(a) (b)

Fig 3.13(b). Fig 3.13(a) also shows the discrimination power between Drell-Yan+jets and $t\bar{t}$ base on the E_T^{miss} distribution.

The shape of the Matrix Element weight distributions are similar between the dielectron channel and the dimuon channel as shown in Fig. 3.14. It motivates a simplified approach consisting to consider only the dielectron channel sample to build the neural network discriminant. So this sample is divided in the so called test and training samples. This methodology has been chosen in order to avoid any bias due to the fact that the learning and test sample, considered to fix the neural network discriminant, are used to validate the comparison between data and simulated event. Finally, the obtained discriminator is applied for both the ee and the $\mu\mu$ channels.

Figure 3.14 – Comparison of the distribution of the weights between the ee and the $\mu\mu$ channels. - Left: $gg \to Z(l^+l^-)b\bar{b}$ hypothesis. - Middle: $qq \to Z(l+l^-)b\bar{b}$. For theses two matrix elements the correction for the transverse boost is evaluated only with the visible particles. - Left $t\bar{t}$ hypothesis, the boost correction uses the missing transverse energy information.The top plots represents the DY sample while the bottom plots the $t\bar{t}$ sample

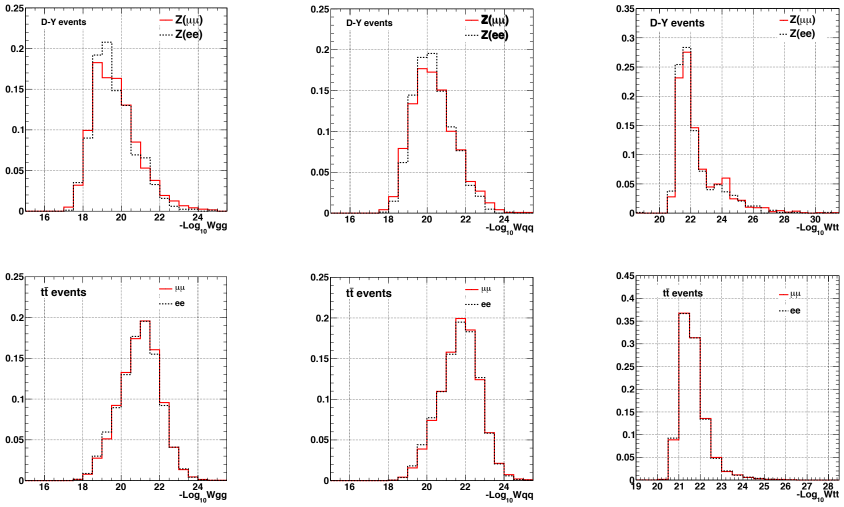

Since the signal to background ratio can be slighly different for both channels, neural network discriminants are evaluated separately for the dimuon and the dielectron channels. In both cases there is a good agreement between simulation and data, as illustrated in Fig. 3.15(a), and in Fig. 3.15(c). The discrimination power of the neural network is evaluated by calculating the signal significance, defined as $\frac{S}{\sqrt{S+B}}$, where $S = Z + b$, and $B = t\bar{t}$, $Z + c$, $Z + l$, ZZ, as a function of the selection cut applied on the neural network output. This is shown in Fig 3.15(b), and byFig 3.15(d).

Figure 3.15 – Left: Comparison of the distribution of the neural network output for data and simulated events using 5.0 fb^{-1} of data. - Right: Evolution of the signal significance as a function of the cut applied on the neural network discriminator output. The plots are obtained for the neural network based on the matrix element weights and E_T^{miss} for the dielectron channel (top plots) and dimuon channel (bottom plots).

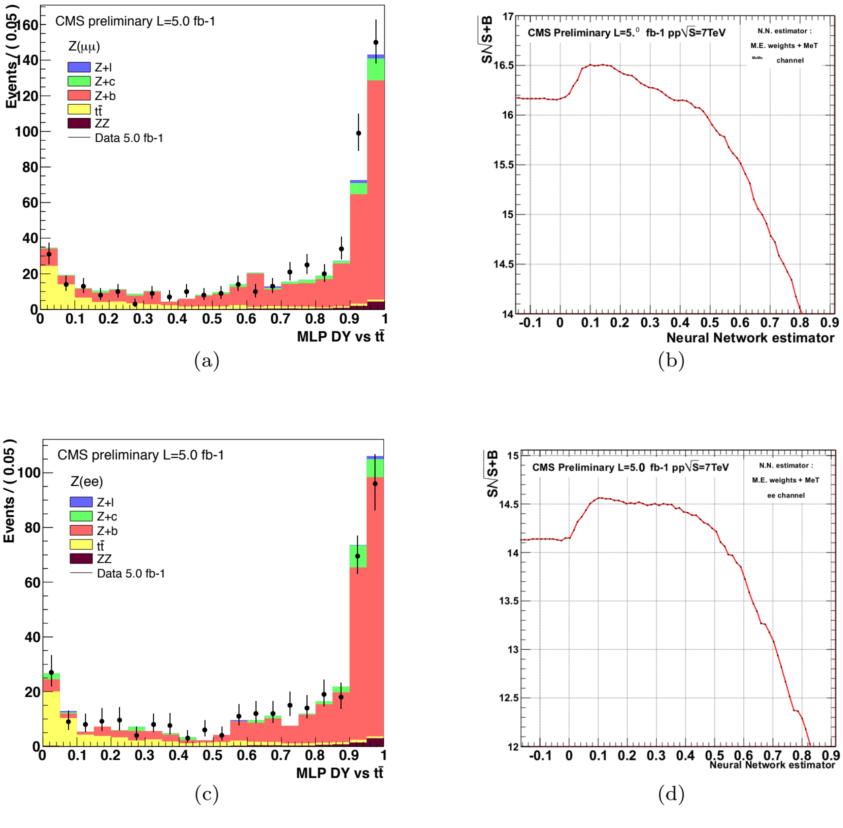

(a) (b)

(c) (d)

It was shown that the purity of the dataset can be slightly improved by looking at the a Neural Network discriminator based on the Matrix Element weights. From the Fig. 3.15 b and Fig. 3.15 d, it is observed that the signal significance $\frac{S}{\sqrt{S+B}}$, could indeed improve by $2-3\%$. However, it has not been used for the cross-section measurement since systematic uncertainties have not been taken into account.

3.1.6 $t\bar{t}$ fraction estimation for $Z(ll)+b\bar{b}$ cross-section measurement

The background due to $t\bar{t}$ is the largest with the working points used to select two b-jets because the Drell-Yan + light flavor jet background are reduced to a negligible level.

Generally the $t\bar{t}$ fraction is estimated from the dilepton invariant mass distribution, where the mass window is slightly enlarged ($60 < M_{ll} < 120$ GeV) to better constraint the $t\bar{t}$ fraction in a narrower mass window used for the $Z+bb$ cross section measurement. It is also assumed that the relative fractions of $Z+l$, $Z+c$ and $Z+b$ are correctly extracted from the fit of the normalisation factors of these contributions to data by using the secondary vertex mass distribution for the leading and sub-leading b-jet. In addition, the ZZ contribution is obtained by normalizing the simulation to the CMS measured ZZ cross section [114].

Although the fit to the dilepton mass distribution using narrow dilepton invariant mass window is also possible in the at $5.0fb^{-1}$ sample, the resulting error is almost a factor of two larger.

The neural network discriminant presented in the previous section also allows to extract the fraction of $t\bar{t}$ events remaining after applying the final selection requirement. Considering both neural networks, trained with and without the E_T^{miss} , a fit of the $t\bar{t}$ and the Drell-Yan Monte-Carlo template to the shape of the data provides an estimation of the $t\bar{t}$ fraction. The results from this fit are summarized in Table 3.10 while the distributions of the neural network after fit are illustrated in Fig 3.16.

The $t\bar{t}$ fraction estimated using the neural network discriminant, considering the Matrix Element weights and the E_T^{miss} , is compatible with what has been measured in the $Z+bb$ cross section measurement analysis [110], where the fraction has been extracted by a fit of the dilepton mass spectrum on wide mass window ($60-120$ GeV) and extrapolated to the narrow region ($76-106$ GeV).

Table 3.10 – $t\bar{t}$ fraction estimated from a template fit of four discriminants. The invariant mass of the dileptonic system, and the two Neural Network discriminants described Sec.(3.1.5). These fractions are extracted after the full selection criteria. The $t\bar{t}$ fraction obtained using a wide dilpeton mass window ($60GeV < M_{ll} < 120GeV$) extrapolated to the narrow mass window is also presented. The uncertainties are statistical only.

Variable	ee channel	$\mu\mu$ channel
M.C. expectation	17%	15.8%
M_{ll} $(76 - 106)$	$17.0 \pm 3.9\%$	$12.0 \pm 3.1\%$
N.N. M.E. Weights only	$17.0 \pm 3.1\%$	$11.0 \pm 2.3\%$
N.N M.E. Weights + E_T^{miss}	$19.0 \pm 3.0\%$	$12.0 \pm 2.0\%$
M_{ll} wide mass window	$14.0\% \pm 2.5\%$	$13.0\% \pm 1.9\%$

The numbers presented in Table 3.10 show also that both neural network discriminant (using or not the E_T^{miss}) provide similar estimation of the $t\bar{t}$ fraction within their uncertainties. Furthermore, it has to be noticed that the estimation of the $t\bar{t}$ fraction in the narrow dileptonic mass window is slightly more precise extracted with the use of the neural network discriminant than considering the shape of the invariant mass of the leptonic system.

Finally, in the context of search for new physics, the distribution of neural network discriminant between Drell-Yan+jets and $t\bar{t}$, shown in Fig 3.16, do not present any excess of data in a phase space region not $t\bar{t}$ or Zbb like.

3.2 Search for associated production of Z and Higgs boson decaying to bottom quarks.

This section presents an analysis searching for the Standard Model Higgs boson decaying in $b\bar{b}$ and produced in association with a Z^0 boson. As already said previously, the search for such a process is motivated by the observation of the fermionic decay of the S.M. Higgs boson.

The analysis discussed in this thesis makes use of the various aspect of the Matrix Element method presented previously. It consists in a totally different approach to what is done by the main analysis performed by the CMS collaboration [37]. Indeed, like for the $Z + bb$ cross section measurement analysis, the Matrix Element method is used in association with multilayer perceptron

Figure 3.16 – Template fit for $t\bar{t}$ fraction estimation using the Discriminant variable build from the ME weights only (top) and adding the transverse missing energy information in the training (bottom). Left: dielectron channel. Right: dimuon channel .

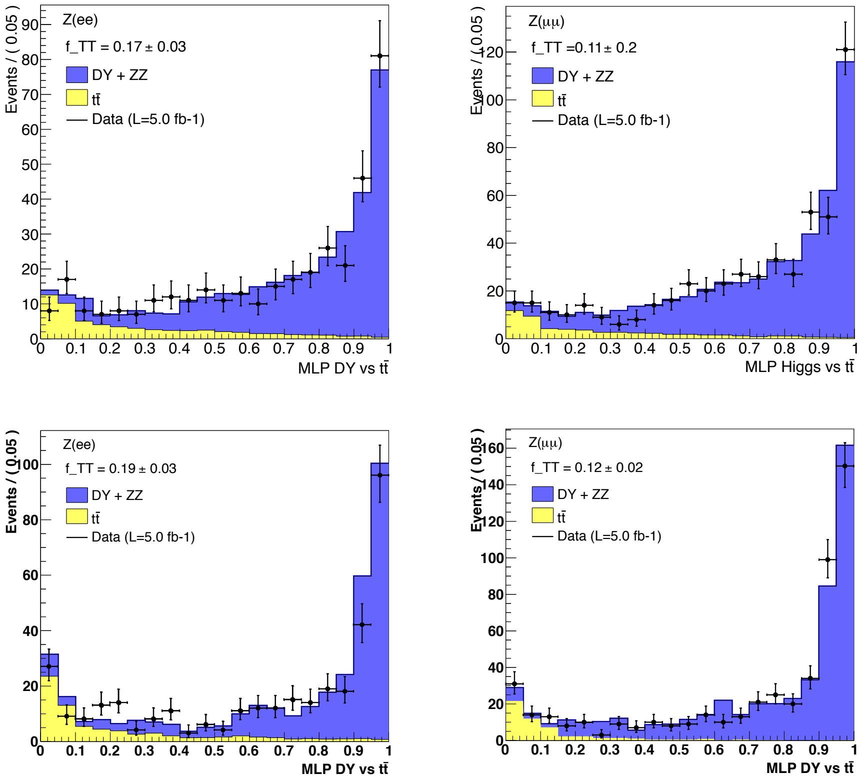

in order to discriminate our signal from the background, which are Drell-Yan+ jets, , $t\bar{t}$ in dileptonic channel and ZZ production.

The Drell-Yan + jets events selected with two b-tagged jet are categorized differently with respect to the $Z + bb$ analysis. Three categories are defined as follow:

- **Z+bb**: The two b-tagged jets correspond to a real b-parton using the Monte-Carlo truth.

- **Z+bx**: One mistag case. One b-tagged jet correspond to a real b-parton, the other one is matched with udsc or g parton.
- **Z+xx**: Two mistags case. Both of the selected b-jets matched with udsc or g parton.

Concerning the signal, the production cross section for each of the signal channel considered have been estimated at next to next leading order [108] and listed in table 3.11. However, the analysis presented in this thesis is optimized for a search of a Standard Model Higgs boson wit a mass of 125 GeV.

Table 3.11 – Cross section for ZH production at $\sqrt{s} = 7$ TeV for Higgs masses between 110 GeV and 135 GeV

ZH $\sqrt{s} = 7$ TeV		
M_H (GeV)	σ (pb)	± (%)
115	0.4107	+5.5, −5.4
120	0.3598	+5.0, −4.7
125	0.3158	+4.9, −5.1
130	0.2778	+5.2, −5.1
135	0.2453	+5.3, −5.0

This section presents first the event selection requirements, then the Matrix Element weights computation and the signal versus background discrimination will be discussed. The background description, the considered sources of systematic uncertainty and an estimation of the exclusion at 95% of the presence of a Standard Model Higgs boson are presented as well.

3.2.1 Event selection

The Higgs search analysis is mainly based on the events selection defined at Sec(3.1.1). Although the b-jets requirements are slightly different. The b-jets are identified using the combine secondary vertex (CSV) algorithm introduced in Sec (1.4.6). The CSV b-tagger is chosen because it is most signal efficient, for a given mistag fraction. The use of the CSV discriminant also allows to enlarge the pseudo-rapidity range up to $\mid \eta \mid < 2.4$. Moreover in order to reduce the contribution of the Z+light jet asymmetric requirements on the jet p_T spectrum have been applied. The p_T spectrum of the leading and subleading b-jets are represented in Fig. 3.17(a) and Fig. 3.17(b) respectively. From these distributions a minimal transverse momentum of 40 GeV for the leading b-jet is required while the cut is p_T > 25 GeV for the subleading. The same motivation, the reduction of Z+light contribution, motivates also to require a minimal transverse momentum for the vector boson candidate of 20 GeV. These additional kinematic criteria highly suppress the DY plus jet background while the efficiency is above 80% for a $Z(ll)H(b\bar{b})$ signal with $m_H = 125$ GeV/c^2 as shown by the yield presented in Table 3.12.

Table 3.12 – Expected events yields predicted by theory for the various background processes at three different selection working points. The expected total number of simulated event is compared to the number of observed event. It shows the efficiency on signal and background of the tighter requirement on b-jet and vecto boson p_T .

Cuts	Zbb	Zbx	Zxx	TT	ZZ	ZH125	SM MC	DATA
Z+bb+MetSig	2039	1973	3052	294	85	$\underline{10}$	$\underline{7443}$	7075
$+p_T(b_1) > 40$ $+p_T(b_1) > 25$ GeV	1167	835	1043	256	55	8.5	3356	3213
$+p_T(Z) > 20$ GeV	1060	767	886	231	49	$\underline{8.0}$	$\underline{2994}$	2866

Figure 3.17 – Transverse momentum distribution for the leading (a) and subleading (b) b-jet for events selected satisfying the leptons requirement and with two jet with p_T > 20 GeV identified as b according to CSV algorithm for Medium-Loose working point.

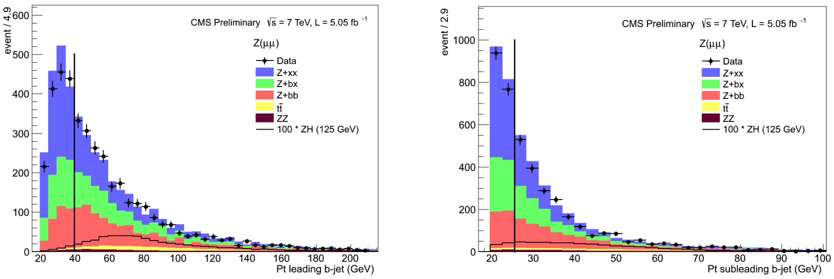

(a) (b)

Of course the correction for b-tag efficiency have been adapted to the recommendation of the b-tag working group. The correction scale factor are available for three different working points that are function of the b identification efficiency. The three working points are the Loose, the Medium and the Tight. They are defined according to the mistag rate 10%, 1% and 0.1% respectively [72]. The two b-jets required in this analysis have to satisfy the Medium and the Loose (ML) working point criteria respectively. This work presents results for events with at least two b-jets selected at Medium-Loose working point. The distribution of the CSV b-tag discriminant represented in Fig 3.18, show that Monte-Carlo prediction reproduce well the data shape. The various background contribution are here normalized to the theoretical prediction.

Figure 3.18 – Distributions of the CSV discriminant for the leading b-jet(left) and the subleaing b-jet(right) at Medium-Loose working point.

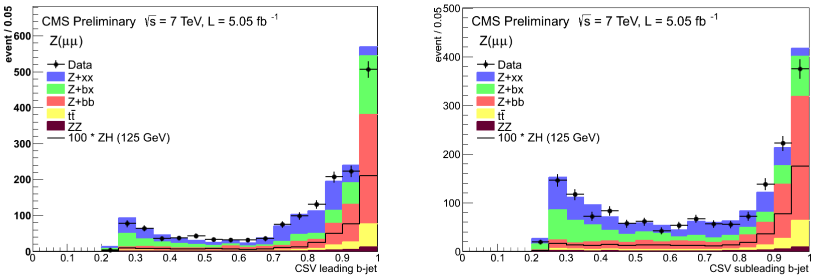

The Matrix Element weights according to signal and background hypothesis have been estimated for each event satisfying these requirements.

3.2.2 M.E. for over constraint system (ZZ,ZH)

The process discrimination technique based on the use of the Matrix Element weights and presented for the $Z(ll)b\bar{b}$ analysis has been generalized in order to discriminate more than two processes, in particular the $Z(ll)H(b\bar{b}\ )$ from its backgrounds. The Higgs search requires the evaluation of the Matrix Element weights under the signal hypothesis as well as under all the background hypothesis. The $t\bar{t}$ and $Z(ll)b\bar{b}$ hypothesis have already been presented, the two other hypothesis to consider are the diboson production and the signal, $Z(ll)H(b\bar{b}\ )$.

The latter two processes present a fully observable final state at detector level. For both cases the leading order dileptonic system and the hadronic system have to satisfy the kinematic constraints related to the Z^0/H Breit-Wigner. Technically, there are 14 quantities to fix. p_T , η and ϕ of the four final state particles in addition to the fraction of longitudinal momentum x_1 and x_2 of the two incoming partons.

In order to fix them, there are constraints from experimental observation and from the theoretical point of view. The 12 experimental constraints result, via the transfer function, from the measurement of the kinematic of the two leptons and the two b-jets. The theory imposes to the ll/bb system to satisfy the Z^0/H Breit-Wigner, it means two additional constraints. Moreover, the conservation of the total Energy and Momentum (E-P) brings four other equations to satisfy, ending with a total of 18 constraints.

In this context, the Monte-Carlo integration computing the Matrix Element weights is not able to probe the full phase space covered by the transfer function. In practice, the integration is done on the lepton TF with the Z^0 Breit-Wigner constraints. Then by assuming the conservation of E-P, the total energy and momentum of the hadronic system is fixed. As the transfer function on the jet direction are modeled by δ functions the energy of the b-partons is fixed as well, the jet energy transfer function and the Z^0/H Breit-Wigner are evaluated and not integrated.

Obviously, the weight estimation approach requires the use of the ISR boost correction. Any extra-radiation with a non negligible transverse momentum that is not considered in the ISR correction induces a violation of the E-P conservation and can lead to the non-convergence of the Matrix Element integration formula or to a non optimal weight.

In order to maximize the use of the transfer function in the numerical integration, a solution consists to relax some constraints. Searching for Standard Model Higgs boson at low mass, around 125 GeV, implies a narrow width of the resonance (Γ_H) of the order of 5.10^{-3} GeV. In this context the $-Log_{10}$ of the Matrix Element weight evaluated on a Z(ll)H($b\bar{b}$) sample with the corresponding hypothesis, presents a sensitivity to the lepton transfer function as show in Fig. 3.19(top). The black curve shows a double peak structure which appear for the dielectron events while the weight distribution is spread on a large spectrum for the dimuon events. The weights evaluation for this two channels differ by the use of different lepton transfer function. This effect has been studied by increasing the Higgs boson width up to be similar to the Z^0 width.

Relax constraints: There are different ways to relax the constraints like assuming a more realistic transfer function on particle direction than δ functions. However, the approach chosen for this analysis consists on relaxing the theoretical conservation of the total energy when evaluating the ME weights. In this condition, the leptonic system does not fix the hadronic one and the MC integration is performed on both lepton and b-jet energy transfer functions. However, a limit on the probe energy spectrum is imposed in order to technically perform the integration on a finite range. For each transfer function, an integration range is associated, ϖ. Considering double gaussian parametrization for the transfer function, ϖ is define as a function of the maximum between the first gaussian width and the second gaussian width evaluated with the reconstructed quantities.

$$\varpi = 5 \times \mathrm{Max}(\sigma_{g1}, \sigma_{g2}) \tag{3.9}$$

The weights evaluated according the prescription relaxing the energy momenta conservation in the transverse plan will be denoted $W(NoE - P)$.

Increase of the Higgs width: Assuming the fully constrained Matrix Element weight computation, the increase of the Higgs boson width in the model parametrization makes the double peak structure disappear in the shape of the weight for the electron channel. This effect is presented in Fig. 3.19(top) which illustrates the evolution of the shape of the $-Log_{10}$ of the Matrix Element weights with respect to the evolution of the Γ_H up to 2.5 GeV. It also shows that the dielectron and dimuon channels become similar. This evolution of the weights goes as $\frac{1}{\Gamma_H^2}$. In fact, the weights decrease with the increase of the Higgs boson width.

It has been observed that this increase of the Higgs boson width in the model parametrization improves the numerical uncertainty on the Matrix Element weights, as illustrated in Fig 3.19(bottom), i.e. the numerical relative uncertainty decrease with respect to the Γ_H increase.

In this work, the Higgs width is choose to be 2.5 GeV, close to the Z^0 width. This explains why these effects were not observed for the $Z(ll)Zb\bar{b}$ hypothesis. This choice is more robust against the transfer function modelization and provides a better numerical precision. Moreover the discrimination between the signal, the $Z(ll)H(b\bar{b}$ and the most important background $Z(ll)b\bar{b}$ is not dramatically affected as illustrated in Fig 3.20.

The Higgs width is also enlarged to 0.16 GeV, for the estimation of $W(NoE - P)$ weights to keep a reasonable numerical precision ($\approx 1\%$). Despite the fact that weights estimated with or without assuming the energy momentum conservation are correlated, both bring information and are considered in this analysis.

Another approach consists on keeping the Higgs boson width narrow, as predicted by the Standard Model. This approach provides more freedom to the Matrix Element integration by assuming a more realistic transfer function of the jet direction variables (η and ϕ). A preliminary study has been done following this prescription. Simple gaussian transfer function on η and ϕ of the b-jets are considered and shown in Fig. 3.21 while their parameters are presented in Table 3.13. These transfer function have been estimated from a $t\bar{t}$ and a

Figure 3.19 – Considering the Higgs Matrix Element weight evaluated assuming the E-P conservation. Top: Shape evolution of the weight distribution with respect to the increase of the Higgs width (Γ_H). - Bottom: Evolution of the numerial uncertainty on the weight. Left for the dielectron channel and right for the dimuon channel.

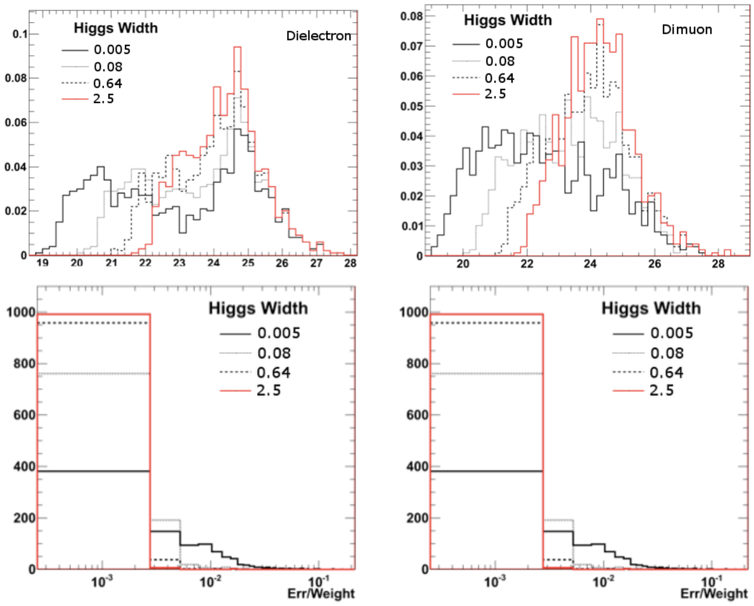

Drell-Yan+ jet sample, a pairing between the selected b-jet and b-partons has been obtained by requiring that $\Delta R < 0.3$.

Table 3.13 – Mean value and width of the gaussian paramerization of the transfer function on η (top) and ϕ of the b-jets.

	transfer fucntion on η b-jet
μ	0
σ	$1.98\ 10^{-2} \pm 2.5\ 10^{-4}$
	transfer fucntion on ϕ b-jet
μ	$2.7\ 10^{-4} \pm 2.1\ 10^{-4}$
σ	$2.06\ 10^{-2} \pm 2.0\ 10^{-4}$

The first results show indeed that the double peak structure tends to disappear as shown in Fig. 3.22. However no complete study of the impact of this approach

Figure 3.20 – Comparison between the Zbb vs ZH efficiency curves for the Matrix Element Higgs weight estimated assuming the E-P conservation and two different Higgs width. Similar performances are observed.

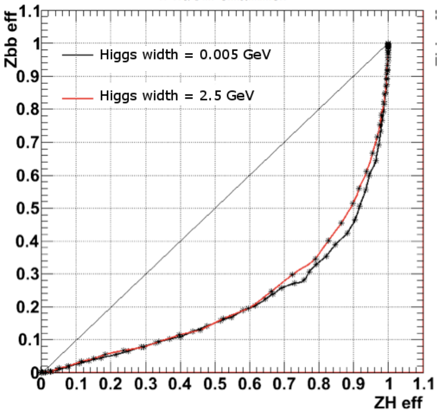

Figure 3.21 – Representation of the considered transfer function on η (left) and ϕ (right) of the b-jets.

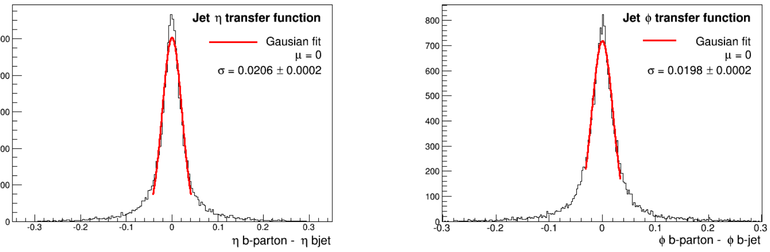

on the discrimination power of the Higgs weight has been performed. So the analysis presented in this thesis has been performed assuming the Higgs boson width increase.

Figure 3.22 – $-Log_10$ of the Matrix Element weight evaluated for a sample of $Z(ll)H(b\bar{b}\ )$ events under the $Z(ll)H(b\bar{b}\ )$ hypothesis. It assumes the Standard Model predicted narrow Higgs boson width and use the transfer function on jet direction presented in Fig. 3.21

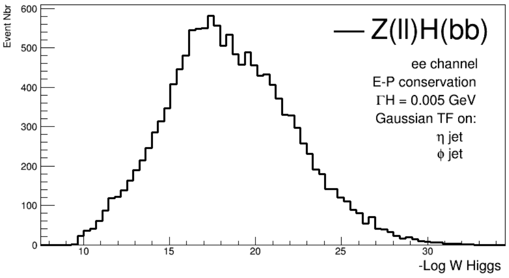

3.2.3 Discrimination ZH vs Background

The Matrix Element weights are considered instead of using a large set of kinematic variables to separate ZH events from background processes. The Matrix Element weights evaluated according to the $t\bar{t}$, $Z(ll)b\bar{b}$, $Z(ll)Z(b\bar{b}\ )$ and $Z(ll)H(b\bar{b}\ )$ provide seven quantities to discriminate signal and background as summarized by table 3.14.

Table 3.14 – List of the different Matrix Element weights estimated for each events in order to perform the H($b\bar{b}$) search analysis.

Process	Hypothesis	ISR correction	E-P conservation
Higgs	$qq \to ZH \to l^-l+\ b\bar{b}$	without MeT	conserved
Higgs	$qq \to ZH \to l^-l+\ b\bar{b}$	without MeT	Not conserved
$t\bar{t}$	$pp \to t\bar{t}\ \to l^-l + \nu\bar{\nu}\ b\bar{b}$	with MeT	conserved
Z$b\bar{b}$	$gg \to l^-l+\ b\bar{b}$	without MeT	conserved
Z$b\bar{b}$	$qq \to l^-l+\ b\bar{b}$	without MeT	conserved
ZZ	$qq \to ZZ \to l^-l+\ b\bar{b}$	without MeT	conserved
ZZ	$qq \to ZZ \to l^-l+\ b\bar{b}$	without MeT	Not conserved

The distributions of $-Log_{10}$ of these seven Matrix Element weights are represented in Fig 3.23, for the dimuon channel exclusively, on a phase space region defined by the selection requirements of Sec (3.2.1), and called full region. The equivalent control plots for electrons are presented in the appendix B.1 . The normalization of each background in these figures is extracted from a data driven technique detailed later at Sec (3.2.4) (as for all the plots in the rest of this chapter), while the normalization of the expected signal corresponds to the theory prediction multiplied by a factor 100.

Distributions of Fig 3.23 show the agreement between Data and Monte-Carlo. The shape differences between signal and background show the discrimination power of the Matrix Element weights, especially looking at the two distributions of the two Higgs hypotheses. The $Z + bb$ hypothesis is represented by the two Matrix Element weights distributions, the $gg \to Zbb$ and $q\bar{q} \to Zbb$.

Figure 3.23 – Comparison of Data-MC at 4.5.0 fb^{-1} of the Matrix Element weights distribution for the seven hypotheses of the ZH analysis. dimuon channel at Z(ll)H($b\bar{b}$) Medium-Loose working point.

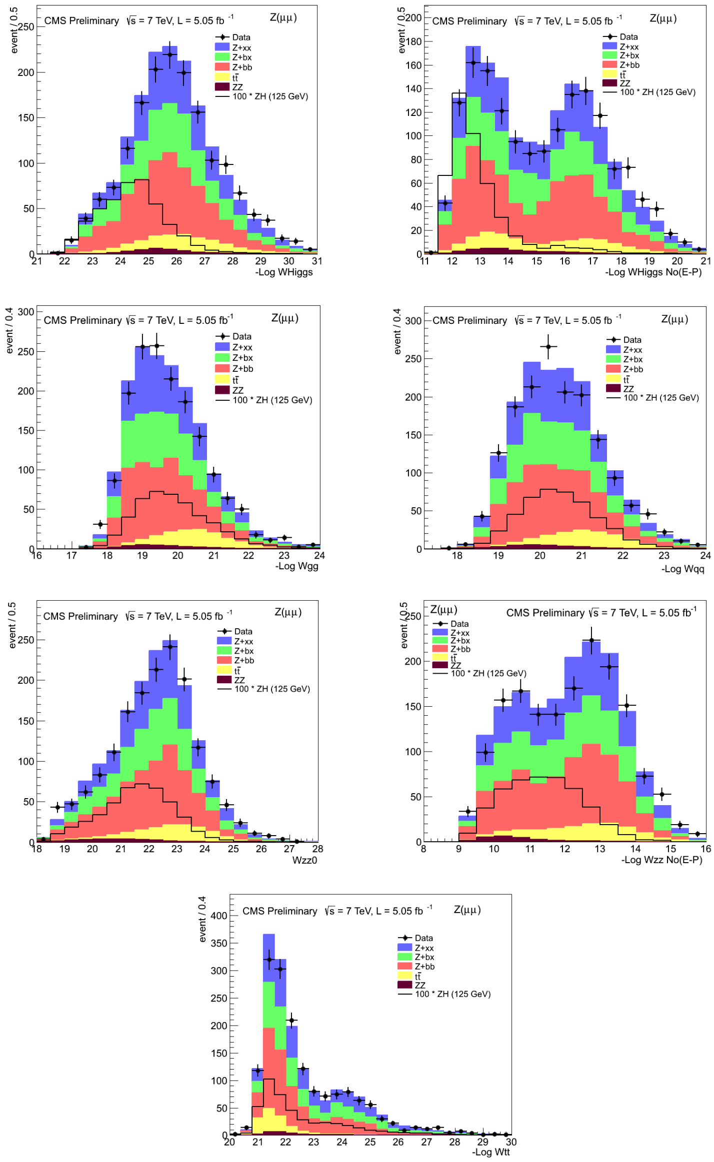

In order to build a final single discriminant to distinguish between the Higgs signal and the background processes, the Matrix Element weights are combined using MLP's as presented Sec (3.1.5). The Neural network training procedure consists to defined two levels of multilayer perceptron. The first step consists to train three independent neural networks which discriminate the $Z(ll)H(b\bar{b})$ process from Drell-Yan + jets, $t\bar{t}$ and ZZ respectively. These three intermediates neural networks use as input the Matrix Element weights which correspond to the processes of interest. Afterwards, a final discriminant quantity is defined as a neural network considering as input the three intermediates ones. In order to bring also information about the jet flavor this final neural network uses as input the the product of the two CSV discriminants.

The analysis is optimized for events with exactly two reconstructed b-jets because of the use of a leading order Matrix Element. It is therefore natural to split the analysis in two categories based on the jet multiplicity. On the one hand the events with exactly two b-jets and on the other hand the events with at least three jets among them two are identified as b's. This categorization is also motivated because looking at $Z(ll)H(b\bar{b})$ simulated events, the $b\bar{b}$ invariant mass spectrum is wider for the category with at least three jets than for the category with exactly two jets as represented in Fig 3.24(right) and Fig 3.24(left) respectively.

The dijet invariant mass distribution peaks at M_H for the signal, at M_Z for the diboson events, decrease for the Z+jets events, and peaks broadly between 100 GeV and 160 GeV for the $t\bar{t}$ events. In the more than two jets category, the larger tails observed on the shape of the M_{bb} distribution for $Z(ll)H(b\bar{b})$ events is related to the presence of final state radiations.

Reduced analysis phase space regions have been defined for both of the categories in order to increase the sensitivity to the signal. These analysis regions are defined by cutting on the dijet invariant mass spectrum around the expected Higgs boson mass. The neural network training, as well as the final measurement, are performed on these reduced phase space regions.

Figure 3.24 – $b\bar{b}$ invariant mass spectrum for both 2-jets(left) and more than two jets (right) categories. Top for the dimuon channel and bottom for the dielectron channel.

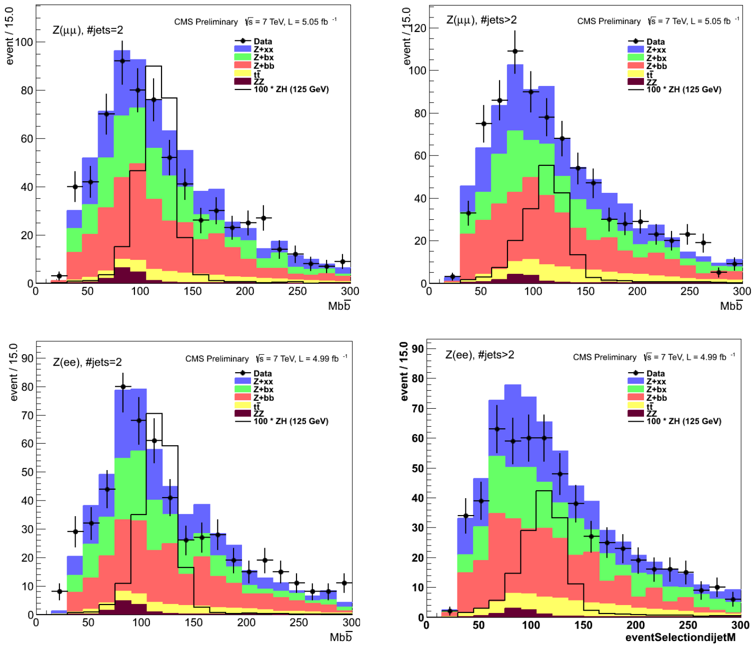

Two jets events analysis

In this first category, after selecting events with a jet multiplicity equal to two and according to the requirement described in Sec.(3.2.1), the analysis region is defined by the dijet invariant mass window $80 < M_{b\bar{b}} < 150$ GeV.

The shapes of the Matrix Element weights distribution are similar between the dielectron and the dimuon channel. Therefore the multilayer perceptron are trained from a ee-$\mu\mu$ merged sample. The following neural networks have been trained:

- **ZH vs DY**: based on the two $Zb\bar{b}$ and on the two ZH weights.
- **ZH vs $t\bar{t}$** : based on the $t\bar{t}$ and on the two ZH weights.
- **ZH vs ZZ**: based on the two ZZ and on the two ZH weights.

- **ZH vs backgrounds**: based on the three previous neural networks and on the product of the CSV discriminants leading and subleading b-jets.

Due to the tight selection requirements the limited statistic of the simulated sample is one of the main difficulty in this analysis. In order to handle this problem additional samples of $Zb\bar{b}$ events have been considered. In addition to inclusive one, a Drell-Yan sample, generated with p_{TZ} above 100 GeV and an exclusive sample of $Zb\bar{b}$+jets generated with MadGraph (in the four flavor scheme [115]) have been considered to trained the different neural networks presented in this section. The number of selected events in each sample used for the neural network training are presented in the Table 3.15. These numbers show how much the exclusive $Zb\bar{b}$ sample increase the statistic. Then the ZZ simulated events is the sample with the smallest number of events. In order to reduce possible bias induced by the NN training procedure, the MadGraph Zbb four flavor sample has not been used in the final sensitivity study of this analysis.

Table 3.15 – Number of events per category in jets multiplicity for the different sample considered in the neural networks training. In the more than two jets category, the training has been performed with a looser cut on p_T jets at 20 GeV.

Sample	2jets events	$>$ 2 jets events
Drell-Yan inclusive	1663	5530
DY $P_{tZ} > 100$ GeV	511	2386
$Zb\bar{b}$ (4F)	5561	16800
$t\bar{t}$	3834	9969
Z(ll)Z($b\bar{b}$)	3098	4927
Z(ll)H($b\bar{b}$) ($m_H = 125$ GeV)	12914	11481

Moreover, the simulated event samples used for the optimisation of the final discriminant, has been divided into two parts in order to define a test and a training sample. The control plots of the intermediate neural networks are presented in the appendix (B.2) for the dielectron and dimuon channel. Fig. 3.25 shows the final neural network between ZH and its background in the two jet category for dielectron and dimuon respectively.

This discriminant show an agreement between the data and the Monte-Carlo predictions in the background region, < 0.5. The $Z(ll)H(b\bar{b}\ )$ contribution is scaled up by a factor 100 and, as expected, it is mainly located at higher values of the discriminant.

Figure 3.25 – Multilayer perceptron ZH-background trained in the two jets category. Left Dimuon channel, right: Dielectron channel.

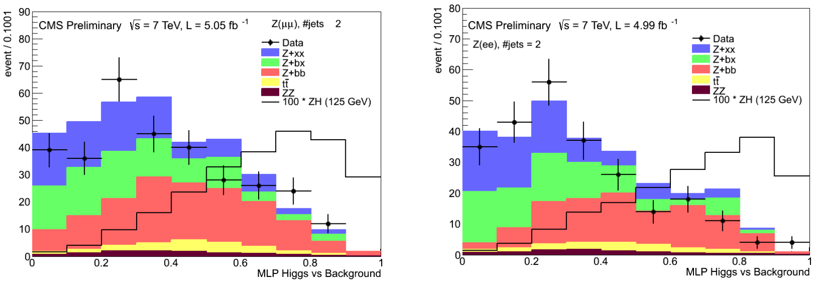

More than two jets events analysis

This second category contains events with more than two jets. In the same way as for the two jets category, an analysis region based on the dijet mass spectrum is defined by requiring $50 < M_{b\bar{b}} < 150$ GeV. In this category, the use of a leading order Matrix Element method is not optimal to study events with extra-radiation. Despite the use of initial state corrections the discrimination based on Matrix Element weights is less powerful in the more than 2jets category.

The degradation is due to the presence of final state radiations that have to be considered as well. Indeed, the final state radiations (FSR) degrade the resolution on the mass of the Higgs candidate reconstructed from the $b\bar{b}$ system. Furthermore as the Matrix Element weights evaluated according to the Higgs hypothesis are highly correlated with the $b\bar{b}$ invariant mass, the discrimination is therefore degraded as well. A possibility would consist to apply a Matrix Element at α_s order. However, the method is then limited by the computing time necessary to perform the numerical evaluation of the matrix element weights.

In order to handle this difficulty, a set of additional variables sensitive to final state radiations and bringing some discrimination between ZH and the main background is used. Denoting j the closest extra-radiation in the $\eta - \phi$ plan with respect to one of the b-jets, this set of new variable contains: the invariant mass of the $b\bar{b}$ +jet system (m_{bbj}), the distance ΔR_{bj} defined as $min(\Delta R(j, b_1), \Delta R(j, b_2))$, and finally the $\eta - \phi$ distance between the two b-jets. These three extra-variables have been considered in addition to the Matrix Element weights as input to trained the MLP discriminant. It has been shown that the use of these additional variables improves the neural network performances similarly to the use of Matrix Element weights computed at higher QCD order [120].

The low value of $M_{b\bar{b}}$ ($M_{b\bar{b}} < 95$ GeV) defines the FSR region in which the ΔR_{bj} and the m_{bbj} variables have some discrimination, while the $\Delta R(b\bar{b})$ does not, as illustrated in Fig. 3.26.

Figure 3.26 – Distributions of three variables used in addition to the Matrix Element weights to improve the discrimination between ZH and $Zb\bar{b}$ for events with extra-radiations. These quantities are showned in a final state radiation region like defined from the invariant mass of the $b\bar{b}$ system $50 < M_{bb} < 95$ GeV.

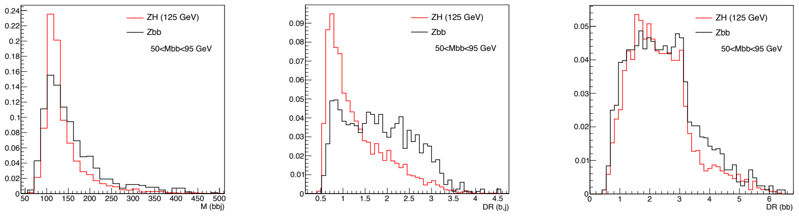

Contrary to what has been said for the FSR region, in the complementary region, at larger values of $M_{b\bar{b}}$ ($\mathrm{M}_{b\bar{b}} > 95$ GeV), the m_{bbj} and $\Delta R(b\bar{b})$ do not show any discrimination between signal and Drell-Yan+jets as shown in Fig. 3.27. However, this figure shows different shape of the $\Delta R(b\bar{b})$ spectrum between both processes.

Figure 3.27 – Distributions of three variables used in addition to the Matrix Element weights to improve the discrimination between ZH and $Zb\bar{b}$ for events with extra-radiation. These quantities are showned in an intitial state radiation region like, $95 < M_{bb} < 150$ GeV.

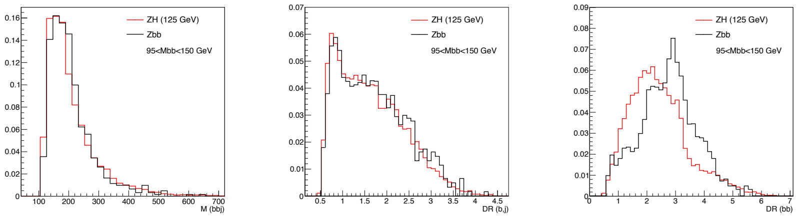

Therefore, the three extra variables are used in addition to the Matrix Element weight as input variables of the various neural networks. Due to the small number of events available in the ZZ sample, the neural network which distinguish ZZ from ZH remains based on the Matrix Element weights only. In the more than two jets category the four following neural networks have been trained on an extended phase space region. Indeed, the training has been performed with a looser cut on p_T jets at 20 GeV. It has been motivated to maximize the number of simulated event used to train the different neural networks with the additional variables.

- **ZH vs DY**: based on the two $Zb\bar{b}$, the two ZH weights, the m_{bbj}, the $\Delta R(b\bar{b})$ and the ΔR_{bj}.
- **ZH vs** $t\bar{t}$: based on the $t\bar{t}$ and the two ZH weights, the m_{bbj}, the $\Delta R(b\bar{b})$ and the ΔR_{bj}.
- **ZH vs ZZ**: based on the two ZZ and on the two ZH weights. Due to the lack of Monte-Carlo statistic, the additional variables have not been included.
- **ZH vs backgrounds**: based on the three previous neural networks and on the product of the CSV discriminants leading and subleading b-jets.

The final discriminants in the more than two jets category are shown in Fig. 3.28 for the dimuon and the dielectron channel respectively. Like for the two jet category, the control plots of the intermediate neural networks are presented in the appendix (B.2).

Figure 3.28 – Multilayer perceptron ZH-background trained in the more two jets category. Left Dimuon channel, right: Dielectron channel. The signal contribution has been increased by a factor 100

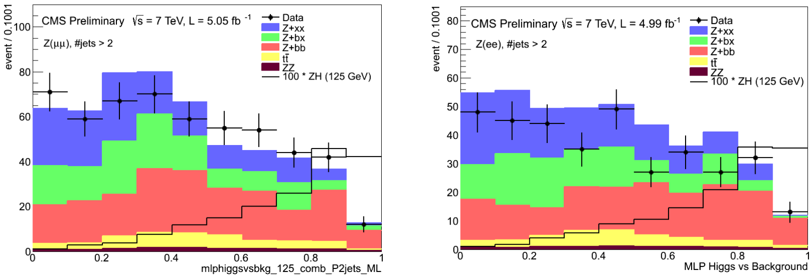

These distributions clearly show that the signal is located at higher values of the discriminant as expected. No discrepancy is observed between data and the Monte-Carlo prediction in background region defined by the low values of the neural network (< 0.5).

3.2.4 Background description

This section discusses the normalization of the various background contributions. In order to better quantify the background yields, they are adjusted using a similar data driven technique as the one presented in Sec.(3.1.6) for the $t\bar{t}$ fraction estimation. It consists into a template fit of the shape of specific variables of the Monte-Carlo to the data. Moreover, the background normalization uncertainties obtained using such a data driven approach includes the uncertainties due to the lepton and b-tag efficiencies for the concern processes.

In order to avoid being affected by the presence of $Z(ll)H(bb)$ events, signal depleted regions for both two jets and more than two jets categories are defined based on the final neural network discriminants which are trained to separate the signal from the different background, see Sec.(3.2.3). These two variables are required to satisfy $MLP < 0.5$. Moreover, in order to have a region with enough simulated events of the $t\bar{t}$ process, the control region has been extended to a wider mass window on the invariant mass of the dileptonic system, $60 < M_{ll} < 120$ GeV.

The impact of the mis-modeling of the p_T of the vector boson observed by the $Z(ll) + bb$ analysis will be discussed as well in this section.

Background normalization

The background normalization is corrected from the theoretical prediction for the different background processes. This is performed by introducing data-driven scale factors for each of these processes with the exception of the ZZ production which is normalized according to the CMS cross-section Measurement [114]. These scale factors are applied in addition to the theoretical predicted normalization.

The same scale factors are assumed for both dielectron and dimuon channels. This reduces the number of scale factors to four: **SF_Zbb**, **SF_Zbx**, **SF_Zxx**, and **SF_**$t\bar{t}$ . . These scale factors allow to adjust the overall yields of different background contributions namely: **Z+bb**, **Z+bx**, **Z+xx** and $t\bar{t}$ samples respectively.

This fit has been performed from two discriminant variables which separate either the jet flavor or the Drell-Yan+jet from the $t\bar{t}$ process have been considered. The first discriminant is a neural network built to distinguish $t\bar{t}$ from Drell-Yan, as presented previously in the Sec (3.1.5). The second variable of interest is the product of the b-tag discriminants for leading and subleading b-jet.

Based on these two variables, the scale factors have been estimated performing two 2-dimensional fits simultaneously for the dielectron and the dimuon channels. Denoting with "+jets" the processes with extra radiations and assuming the independence between the 2jets and the more than 2jets category, eights scale factors can be estimated. However, it is further assumed that the scale factors for the processes **Z+bx**, **Z+bx**+jets and the **Z+bb**+jets are the same in both cathegories.

This assumption is motivated by the fact that the theory that describes **Z+bx**, **Z+bx**+jets and **Z+bb**+jets processes is dominated by processes at next to leading order in α_s with respect to the LO **Z+bb** process, as shown in Fig 3.29 (right) and Fig 3.29 (left) respectively. The two processes, **Z+bx** and **Z+bx**+jets, are indeed similar to **Z+bb**+jets where one of the jet is not observed or not selected or badly reconstructed.

Figure 3.29 – Representation on one of the production modes of $Zb\bar{b}$ events with or without extra-radiations. Left: Production diagram for the selected $Zb\bar{b}$ final state without extra jets. Right: Production diagram for the selected $Zb\bar{b}$ final state with extra jets, Zbx and Zbx+jets final states.

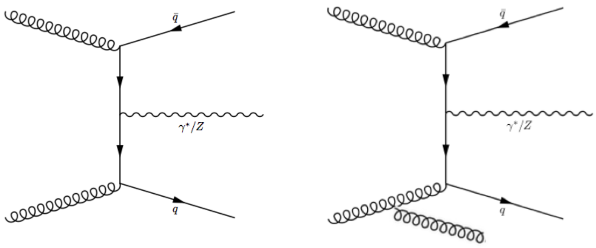

As well, the scale factors related to **Z+xx** and **Z+xx**+jets are also assumed to be the same. Therefore assuming a good modelization of the b-tag and mistag efficiencies. The number of scale factors has been reduced to four:

- **SF_Zbb**: It represents the scale factor to apply to the **Z+bb** events in the 2 jets category.
- **SF_Zbx**: It is the common scale factor acting on the normalization of the **Z+bb**+jets, **Z+bx**+jets and **Z+bx** processes.

- **SF_Zxx**: This is the scale factor to adjust the normalization of the **Z+xx** and **Z+xx**+jets processes.
- **SF_$t\bar{t}$** : This scale factor adjusts the normalization of the $t\bar{t}$ and $t\bar{t}$ +jets processes.

The scale factors are extracted from two 2D simultaneous fit of two variables between both categories and between electron and muons samples. The numerical values of these scale factors are summarized in the Table 3.16.

Table 3.16 – Scale factor estimated from two 2D simultaneous fit of shape of a neural network which separate Drell-Yan from $t\bar{t}$ and the product of the CSV discriminant of the two selected b-jet. It fit the sumulated background shape of these variables to the data one in a control region.

SF	$\#jets\ = 2$	$\#jets\ \geq 3$
SF_Zbb	0.98 ± 0.07	1.14 ± 0.08
SF_Zbx	1.14 ± 0.08	1.14 ± 0.08
SF_Zxx	0.87 ± 0.08	0.87 ± 0.08
SF_TT	0.90 ± 0.07	0.90 ± 0.07

Fig. 3.30 shows the agreement between data and Monte-Carlo predictions normalized using the scale factors of the Table 3.16. The four top plots present, for the 2 jets category, the distribution of the b-tag CSV product discriminant and the neural network which distinguish $t\bar{t}$ from Drell-Yan induced events respectively. The two distributions on the left are for the dielectron channel while the two on right for the dimuon one. The four bottom distributions illustrate the same agreement in the case of the more than two jets category.

Considering this data driven background normalization, the expected yields for the various background and signal processes have been computed and compared to the number of observed data. The Table 3.17 summarized the yields separately for the control and the analysis regions, in both cases results are shown for the two categories in jets multiplicity in dielectron or dimuon channel. The use of normalization scale factors extracted from events in the control region present a good agreement between data and Monte-Carlo yields in the same region, while a small deficit of data is observed in the analysis region.

Figure 3.30 – Distributions of the variable of interest used to extract the background normalization scale factors and normalized according to them (the MLP DY vs $t\bar{t}$ and the product of the CSV discriminnat value for the leading and the subleading b-jet). The top plots represents the 2 jets category while the bottom plots show the more than two jets category .

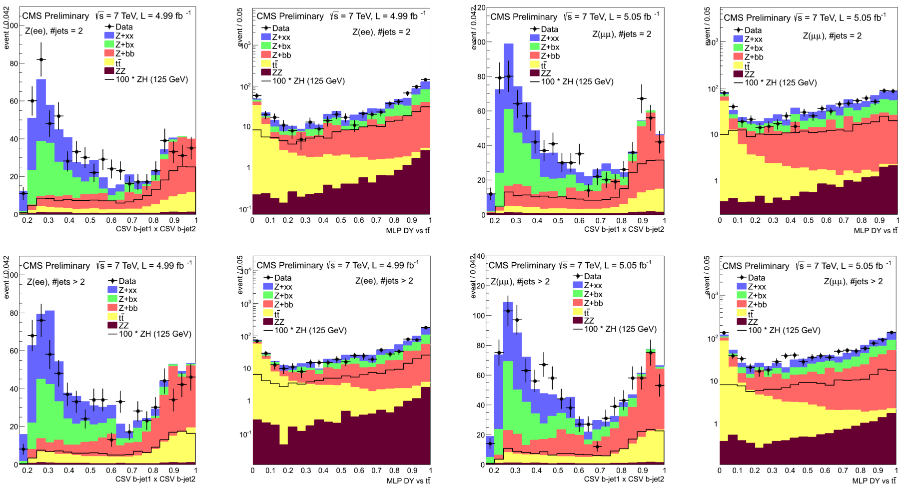

Pt Z reweighting

The kinematic tension that have been observed in the $Z(ll)$+bb cross section measurement analysis [110] and shown at Fig. 3.5 have to be study as well in the context of the Higgs boson search analysis. The spectrum mis-modeling of the p_T of the vector boson for the $Z + b's$ simulated event is study by looking at the following variable,

$$R_i = \frac{(Data - t\bar{t} - ZZ - Zxx)_i}{(Zbx + Zbb)_i}. \tag{3.10}$$

It consists into a per bin (i) ratio between the observed number of data events, from which the $t\bar{t}$, ZZ and **Z+xx** expected yields are subtracted, by the **Z+bx** and **Z+bb** expected yields.

Considering the categorization defined by the jet multiplicity, the tighter cut on the p_T of the jet than the one considered in the previous analysis, and

Table 3.17 – Summary of yields after normalization based on the scale factors fitted differently for the 2 jets and More than 2 jets categories. The ZH sample has been generated with $m_H = 125$ GeV.

Channel	Data	Tot MC	Zbb	Zbx	Zxx	$t\bar{t}$	ZZ	ZH
Control region								
ee 2 jets	566	522.6	154.3	139.4	163.3	62.1	8.4	0.4
ee $>$ 2 jets	594	634.4	160.7	156.6	201.9	108.9	6.3	0.3
ee total	1160	1157	315	296	365.2	171	14.7	0.7
$\mu\mu$ 2 jets	683	707.2	226.2	184.1	208.2	77.4	11.3	0.5
$\mu\mu$ $>$ 2 jets	822	836.2	254.2	199.1	242.4	131.8	8.7	0.4
$\mu\mu$ total	1505	1543.5	480.4	383.2	450.6	209.2	20	0.9
Analysis region								
ee 2 jets	248	271.8	94.1	78.1	75.9	15.4	8.3	1.9
ee $>$ 2 jets	354	420	145.6	104.3	129.8	33.0	8.0	1.4
ee total	602	691.8	239.7	182.4	205.7	48.4	16.3	3.3
$\mu\mu$ 2 jets	315	353.4	136.0	93.9	92.8	20.1	10.6	2.4
$\mu\mu$ $>$ 2 jets	533	534	197.6	123.3	151.7	41.6	11.2	1.8
$\mu\mu$ total	848	887.4	333.6	217.2	244.5	61.7	21.8	4.2

the data driven normalization of the various background processes, the mismodeling observed in the previous analysis tends to disappear as illustrated by the Fig. 3.31. Indeed, these two plots present that the ratios (R_i) can be described by a constant term, meaning that the no global shape discrepancy is observed. The agreement between data and MC is also presented in Fig 3.32 which illustrates the distributions of the p_{TZ} spectrum in the control region, separately in the dimuon and the dielectron channels and for both categories in jet multiplicity.

In conclusion, in the phase space defined by the selection requirement described at Sec.(3.2.1) applying the data-driven background normalization as defined previously, the modeling of the p_{TZ} is considered as a negligible effect.

Figure 3.31 – Ratio $(Data - t\bar{t} - ZZ - Zxx)/(Zbx + Zbb)$ fitted by a constant term. Both categories show an agrrement with 1.

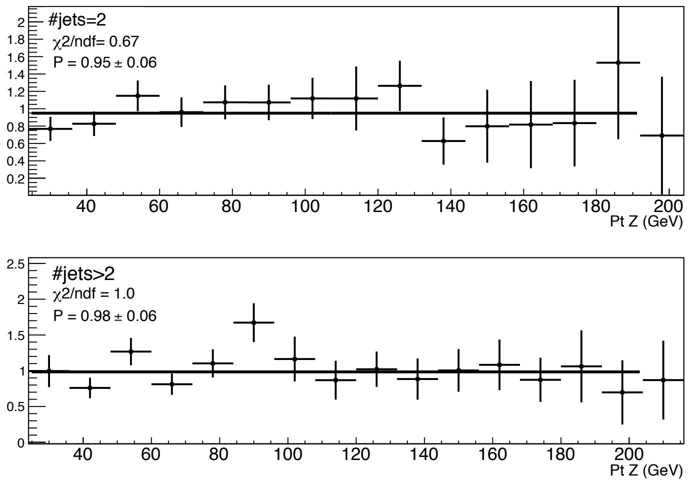

3.2.5 Expected sensitivity including systematic uncertainties.

The search for Standard Model Higgs boson is based on the shape of the final MLP discriminants of the Fig 3.25 and Fig 3.28 for both categories respectively and correctly normalized according the prescription of the Sec.(3.2.4) .

Upper limit calculation

It is useful to characterize the sensitivity of an experiment by reporting the expected significance that one would obtain for a variety of signal hypotheses.

The statistical significance of an observed signal can be quantified by means of a p-value.

In particle physics one usually converts the p-value into an equivalent significance, S, defined such that a Gaussian distributed variable found S standard deviations above its mean has an upper-tail probability equal to p [121]. That is,

Figure 3.32 – Distribution of the p_T of the Z boson candidate in the control region merging togheter 2jets and more than 2jets categories and assuming their onwn normalization. Left: Dimuon events. Right: dielectron events.

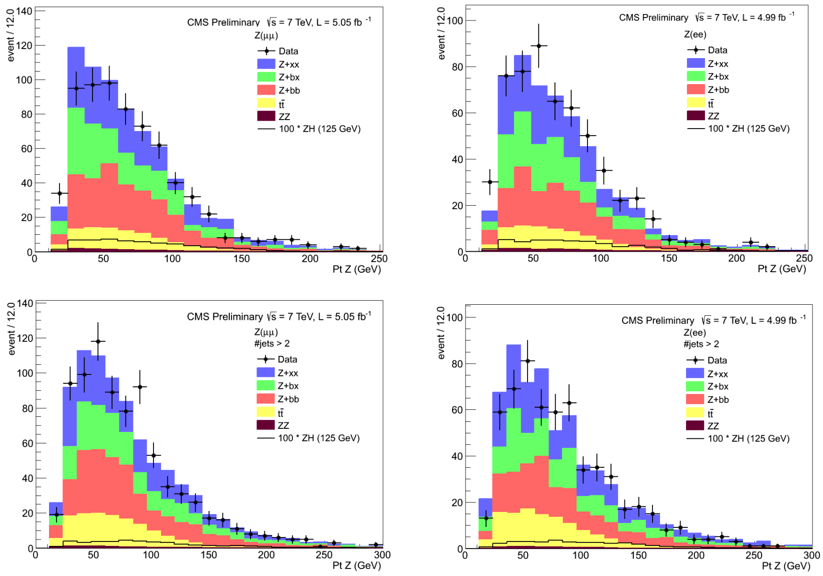

$$S = \Phi^{-1}(1-p) \tag{3.11}$$

where Φ^{-1} is the quantile (inverse of the cumulative distribution) of the standard Gaussian. The appropriate level of significance to claim a discovery is for $S = 5$ that correspond to p-value of $p = 2.87 \times 10^{-7}$.

The purpose of this analysis is the to perform the exclusion of a signal hypothesis. In this context a threshold p-value of 0.05 (i.e., 95% confidence level) is often used, that threshold corresponds to $S = 1.64$.

In particle physics the procedure to establish discovery (or exclusion) is based on a frequentist significance test using a likelihood ratio as a test statistic, $\tilde{q}_\mu$ [121]. It can be applied either for a cut and count analysis with a single likelihood or for an analysis in which the full shape of a discriminant variable have sensitivity. In that case, the likelihood function is the product of Poisson probabilities on all the bins (N):

$$\mathcal{L}(\mu,\theta) = \prod_{i=1}^{N} \frac{(\mu.s_j + b_j)^{n_j}}{n_j!} e^{-\mu.s_j - b_j} p(\tilde{\theta}|\theta) \tag{3.12}$$

The n_j, s_j and b_j represents in the bin j the observed, the signal expected and the background expected rates. The parameter μ represent the signal strength modifier ($\frac{\sigma}{\sigma_{SM}}$) and θ contains all the nuisance parameter terms, e.g. the the uncertainty on the predicted event yields. $\tilde{\theta}$ are the expected values of the nuisance parameters. The tested hypothesis is not signal only but signal and background expressed as $\mu.s + b$. The probability of interest consist into the log-likelihood ratio as expressed by

$$\tilde{q}_\mu = -2ln \frac{\mathcal{L}(data|\mu, \widehat{\theta_\mu})}{\mathcal{L}(data|\widehat{\mu}, \widehat{\theta})}. \tag{3.13}$$

where $\tilde{\mu}$ and $\tilde{\theta}$ maximize the likelihood given the observed data while $\tilde{\theta_\mu}$ maximize the likelihood for a given value of μ with a constraint $0 \leq \tilde{\mu} \leq \mu$.

According to the definition of the likelihood ratio definition, q_μ represents the incompatibility between the data and the hypothesized value of μ and the higher is q_μ the greater is the inconsistency. The p-value that quantifies the level of agreement between the data and hypothesized μ for a an observed $q_{\mu,obs}$ is expressed as

$$p_\mu = \int_{q_{\mu,obs}}^{\infty} f(q_\mu|\mu) dq_\mu, \tag{3.14}$$

where $f(q_\mu|\mu)$ represent the *pdf* of q_μ assuming the hypothesis μ. This *pdf* is built by generation of toy experiments. The confidence level is then constructed as

$$CL_s(\mu) = \frac{p_\mu}{p_0} \tag{3.15}$$

If for $\mu = 1$, CLs < 0.05, the SM Higgs boson with a nominal production rate is said to be excluded at 95% Confidence Level (C.L.).

Systematic uncertainties.

Systematic uncertainties affecting the estimated rates of signal and background processes, as well as the shape of the final discriminator, can bias the outcome of this Higgs-boson search. The most important uncertainties that affect the normalization of the signal are the ones related to the uncertainty on the theoretical cross section, the b-tagging efficiency and the jet energy scale. Most of these uncertainties, like the b-tagging efficiency one, do not affect directly the normalization of the main backgrounds, as they are determined by performing a fit to the data. They would only affect the background normalization if the uncertainty has an effect on the shape of the variables used in the final discriminant.

For these reasons only the statistical uncertainty of the fit is considered as a systematic on the global yields for the $t\bar{t}$, $Z + bb$, $Z + bx$, and $Z + xx$ processes. The normalization of the ZZ process is based on a CMS measurement, the uncertainty of this measurement [114], is considered as a rate systematic uncertainty. For the jet energy scale, also the effect on the shape of the discriminator for the different processes is taken into account. The limited size of the used Monte Carlo samples is also considered. A detailed list of the systematic uncertainties considered is given below:

The Background normalization: The uncertainties on the four scale factors extracted from the fit of the background estimation have been considered taking into account their correlations. This concerns the DY+jets and the $t\bar{t}$ contribution. The sources of uncertainties have been un-correlated according to a procedure detailed in the appendix B.1. About the diboson background the normalization uncertainty comes from the uncertainties on the CMS cross-section measurement.

Lepton Reconstruction and Trigger Efficiency: These efficiencies are measured using $Z \to ll$ decays in data using the Tag and Probe technique. A flat uncertainty of 2% is associated to the total trigger and lepton reconstruction efficiency both for electrons and muons. Uncertainties between electrons and muons are assumed to be uncorrelated. This uncertainty is only applied to the signal process.

b-tag reweighting: The scale factors associated to b-jet tagging are variated up and down according to their uncertainties. This results in a variation in the number of selected signal events of 6%. The background fit has to be repeated using the same variations of the b-tag scale factors. However, this source of systematic has not been considered in the final result presented in this thesis.

The luminosity uncertainty: An uncertainty of 2.3% is assumed for the 2011 luminosity. As the background normalization is Data driven, this uncertainty is applied for the signal normalization only.

Signal coss section: The assumed total signal cross section of production and decay have been computed at next-to-next-to-leading order. The considered uncertainty is about 4%.

The Monte-Carlo statistic uncertainty: The limited size of the generated Monte Carlo samples implies a non-negligible source of uncertainty. The Monte Carlo statistic uncertainty is considered as a shape fluctuation. For each bin of the final discriminator, alternative shapes are defined by varying exclusively that bin. The corresponding up and down fluctuation are obtained by looking at $+/-$ one standard deviation of a poisson law distribution centered on the number of Monte Carlo events that populate that bin. Fig. 3.33 illustrates it for the **Z+bb** process with the bin $(0.9 - 0.95)$. It shows the asymmetry between the up and down fluctuation due to the poisson statistic consideration.

Figure 3.33 – Illustration of a the shape fluctuation considered to take into account the statistic uncertainty due to the available number of simulated event. It shows the asymmetric up and down fluctuation for the bin $(0.9 - 0.95)$ for the **Z+bb** processes. The distribution stay un-changed for the other bin.

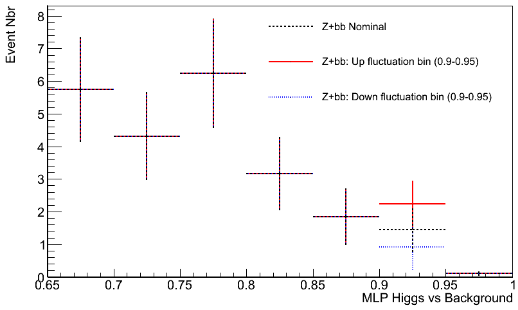

These variations have been considered as independent nuisance parameters in the CL_s estimation.

Jet energy scale uncertainty: The jet-energy-scale uncertainty is evaluated by applying jet-energy corrections that describe one standard deviation variations with respect to the default correction factor. The event selection and the evaluation of the Matrix Element weights is performed again after applying the jet-energy shifts. This allows to obtain two alternative shapes (corresponding to the $+1\sigma$ and -1σ shifts) of the final neural network, in order to study the systematic effect of the jet-energy-scale uncertainty in the shape of the discriminator. Despite the fact that the procedure has been established, the systematics due to jet energy scale uncertainty has not been included in the estimation of the confidence level limits.

others: Additional sources of systematic uncertainties exist but have not been considered for the results presented in this work. This category includes the jet energy resolution uncertainty, the uncertainty on the E_T^{miss} that is used to defined the transverse boost correction for the $t\bar{t}$ hypothesis or the Monte-Carlo generator effect.

3.2.6 Results

The shape of the Neural network discriminants presented at Sec.(3.2.3) in Fig. 3.25 and Fig. 3.28 and normalized according to the prescriptions of Sec. (3.2.4) allow to evaluate an exclusion limit at 95% of the presence of a Standard Model Higgs boson, CL$_s$. It has been estimated using the LHC CL$_s$ method briefly introduced is Sec. (3.2.5).

Despite the fact that the analysis has been optimized only for a Higgs with a mass of 125 GeV, the limits for four other mass working points have been computed as well. The hypothesis of Standard Model Higgs with mass of 115, 120, 130, 135 GeV have been tested as well. $Z(ll)H(b\bar{b})$ Monte-Carlo sample generated with these four Higgs masses have been considered. For all the simulated and data events the Matrix Element weights have been estimated according to all the Higgs mass hypotheses. The neural network discriminants have not been retrained, however the MLP function trained with the $m_H =$ 125 GeV hypothesis has been used to defined discriminant for each mass point evaluating it with the corresponding Matrix Element Higgs weights as input.

The Expected and observed limits have been estimated separately for the two jets, more than two jets categories and for the dielectron and dimuon channels. The systematic uncertainties are partially considered. Indeed the Monte-Carlo statistic uncertainty, the background normalization, the luminosity uncertainty and the signal normalization uncertainty only have been considered. However, we believe that the most important have been included.

The obtained results are summarized in the table 3.18 for a Standard Model Higgs boson with a mass of 125 GeV and the mass scan is represented in Fig 3.34.

Table 3.18 – Expected and observed 95% confidence level upper limit on the ratio of the Standard Model production of $Z(ll)H(b\bar{b})$ with a Higgs boson mass of 125 GeV. Limits estimated separately for four analysis channels defined according to the jet multiplicity and the lepton flavor.

$Z(ll)Hb\bar{b}$ $\sqrt{s} = 7$ TeV - $m_H = 125$ GeV		
Channel	Expected	Observed
$\mu\mu$ 2 jets	$8.1^{+4.0}_{-2.5}$	7.3
ee 2 jets	$9.8^{+4.5}_{-3.0}$	8.4
$\mu\mu$ >2 jets	$15.9^{+6.8}_{-4.7}$	21.7
ee >2 jets	$16.8^{+7.6}_{-5.1}$	17.3

Figure 3.34 – Expected and observed 95% upper limits on the ratio of Standard Model production of $Z(ll)Hb\bar{b}$ for the Matrix Element method analysis. (a) $Z(\mu\mu)$ in the two jet category. (b) $Z(ee)$ in the two jet category. (c) $Z(\mu\mu)$ in the more than two jet category. (d) $Z(ee)$ in the more than two jet category.

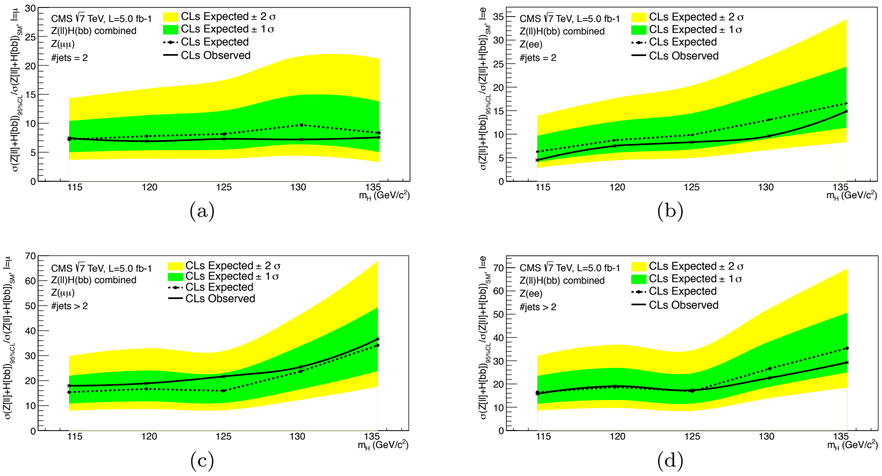

(a) (b) (c) (d)

The four channels have been combined to provide the $Z(ll)H(b\bar{b})$ limits for the considered Higgs mass points. As far as the hypothesis of a Higgs boson with a mass of 125 GeV/c^2 is concerned the observed upper limit at 95% confidence level is 5.7 times the standard model prediction while the expected one is $5.2^{+2.4}_{-1.6}$. In order to compare with the official analysis, the limit has been computed blinding the signal shape that is $4.8^{+2.3}_{-1.5}$ and compare to limit based on the V(ll)Hbb channel from [122] that is $4.5^{+2.8}_{-1.5}$.

The expected and blind estimated upper limit are suppose to be the same, since in the LHC prescription, the expected limit does depend a bit on the data in the signal region while the "blind" estimation not. On the one hand, in the case of "expected" limit estimation, the "background" model is taken as a fit to the data with signal fixed to zero. On the other hand, concerning the "blind" calculation, the data shape is replaced by the sum of all the background shape.

Table 3.19 – Expected and observed 95% confidence level upper limit on the ratio of the Standard Model production of $Z(ll)Hb\bar{b}$ with a Higgs boson mass of 125 GeV.

$Z(ll)Hb\bar{b}$	$\sqrt{s} = 7$ TeV - $m_H = 125$ GeV		
	Blind	Expected	Observed
Z(ll)H($b\bar{b}$)	$4.8^{+2.3}_{-1.5}$	$5.2^{+2.4}_{-1.6}$	5.7

A mass scan has been performed as well as represented in Fig. 3.35.

Figure 3.35 – Observed and Expected at 95% confidence level upper limit on the ratio of Z(ll)H($b\bar{b}$) production at 7 TeV. The median expected limit and the 1 and 2 σ band are obtained with the LHC CL$_s$ method.

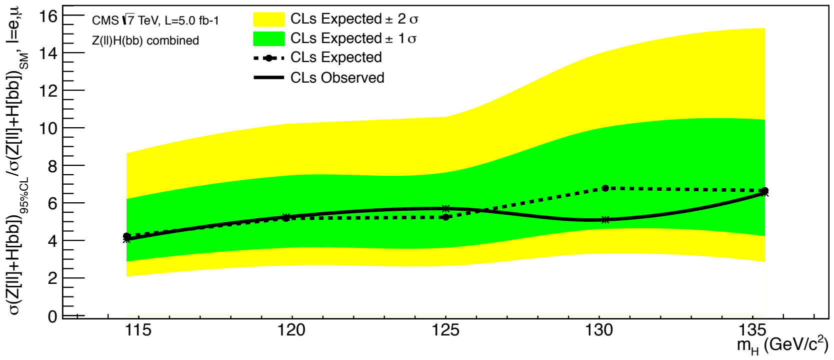

Morever, the observed upper limits are also compared to the median limit expected in the presence of a Standard Model Higgs boson, using a Monte Carlo "signal injection" technique. This result showned in Fig. 3.36, presents a statistical compatibility with the presence or absence of a SM Higgs boson. This results are obtained with asymptotic CLs approximation. Injection of Standard Model Higgs signal at 125 GeV/c^2 provides a very similar shape to the observed one.

Figure 3.36 – Signal injection expected at 95% confidence level upper limit, compared to the upper limit on the ratio of Z(ll)H($b\bar{b}$) production at 7 TeV assuming SM background only.

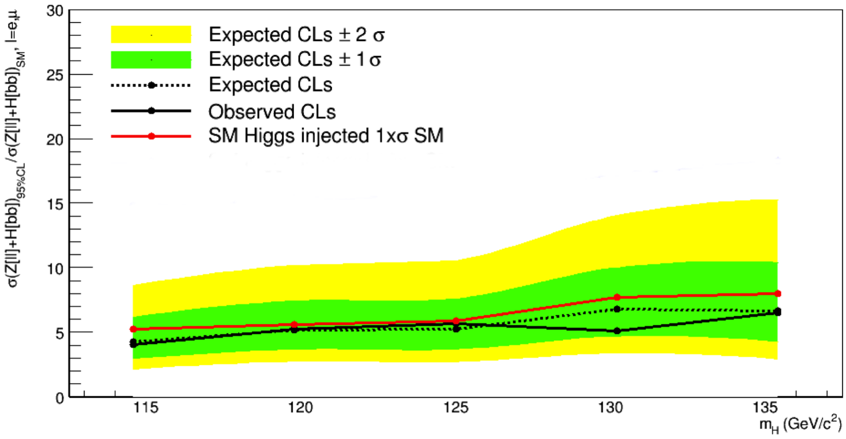

It has been shown that the Matrix Element method can be applied in order to discriminate several processes with a same final state observed in the detector by using a multivariate analysis based on the Matrix Element weights. More over the discriminant has been used in order to estimate an upper limit at 95% confidence level of 5.7 times the standard model prediction for a Higgs boson mass of 125 GeV.

The obtained results using the Matrix Element method are in agreement with the 2011 CMS measurement performed on the same channels [122] with a different approach. Indeed the main differences happen at the level of the selection requirements, the event categorization that depends on the p_T of the vector boson in the main analysis and not on the jet multiplicity.

Conclusion

The Matrix Element Method (MEM) is an advanced analysis technique that optimally exploits the underlying dynamics of possible physics processes responsible of a given final state. Applied for the first time for a precise top quark mass measurement at the Tevatron, its usage at the Large Hadron Collider (LHC) is more challenging due to the complexity of modeling all possible interactions responsible for a given observed final state together with the determination of phase-space integrals taking into account proper transfer functions parameterizing the detector response. This thesis shows for the first time that this method can effectively be applied at the LHC for the final state involving a pair of high energetic lepton anti-lepton and a pair of energetic b and anti-b quarks (llbb), with or without significant missing transverse energy.

For events with a large missing transverse energy, it is shown that a top quark mass measurement can be performed assuming that the dominant process is the top quark pair production followed by their leptonic decay. This study showed that the assumption that a leading order Matrix Element is a good approximation assuming that corrections for the initial state radiation effect be taken into account. Despite the fact that the systematic uncertainties have not been evaluated, the results obtained with the first 36 pb^{-1} recorder during the 2010 campaign is m_{top} = 173.1 GeV $\pm 5.8_{stat}$ GeV is in agreement with the official CMS measurements obtained with the same integrated luminosity as well as with the best current measurement performed at Tevatron which is m_{top} = 173.2 GeV $\pm$0.87 GeV.

An original approach for performing a model independent search of heavy resonances decaying into a top quark pair is also addressed by using a variant of the usual MEM. This study showed that it is possible to obtained a direct measurement of the differential cross sections in the selected phase space region defined by the selection criteria of the considered llbb+MET final state. In particular, differential cross sections with respect to the $t\bar{t}$ invariant mass and the angle between the top quarks in the $t\bar{t}$ rest are shown to be different according to the presence or not of a new resonance.

For a large dileptonic invariant masses, the llbb final state without a large missing transverse energy is dominated by the associated production of a Z boson and a pair of b and anti-b quarks, the production of top quark pair and the production of two Z bosons. This final state can also be populate by the associated production of a Z and the Standard Model Higgs bosons ($Z(ll)H(b\bar{b}$)) . A Matrix Element Method based study has been first tested in the frame of the $Z(ll)(b\bar{b}$) cross section measurement and has been used in association with a multivariate analysis in order to distinguish between the Drell-Yan plus jets and the $t\bar{t}$ processes. This study required to apply the transverse boost correction and was more stable and accurate when using a transfer function for leptons in addition to the b-jets. The obtained results on the estimated $t\bar{t}$ fraction are compatible with the other method presented in the cross section measurement paper.

Finally, dedicated search for a SM Higgs boson based on the MEM has been successfully performed for the first time, using 5 fb^{-1} data recorded by the CMS experiment during the 2010 or 2011 data taking periods. The methodology to discriminate signal and background is similar to the one has been used for the $t\bar{t}$ fraction estimation in the context of the $Z(ll)(b\bar{b}$) analysis . The obtained observed upper limit on the ZH production cross section times the $H \to b\bar{b}$ branching ratio is 5.7 times the standard model prediction while the expected upper limit is $5.2^{+2.4}_{-1.6}$, for a Higgs boson mass of 125 GeV/c^2. The search for a Standard Model Higgs boson actually covered a mass range from 115 GeV/c^2 to 135 GeV/c^2. These results confirm that the Matrix Element based search analysis provides as good measurements as the ones obtained with another technique used by the CMS collaboration with an equivalent luminosity.

Appendix

Appendix **A**

Appendix to the top quark mass analysis

A.1 Error calculation on top quark mass measurement

The statistical uncertainty on the top quark mass estimated using the matrix element method is computed as details in this section. Each event weight carry a numerical uncertainty coming from the MadWeight integration and from the cross-section normalization (computed with MadEvent) . As the events are combined such as Eq A.1,

$$-\ln L(\vec{\alpha}) = -\sum_{events} \ln(\int d\phi |M_\alpha|^2 W(p, p^{vis})) + N\ln(\frac{1}{\sigma_\alpha}) + N\ln(\frac{1}{Acc(p)}) \tag{A.1}$$

the propagation and combination of the uncertainties have to be computed with respect to

$$\delta \ln L(\vec{\alpha}) = \sum_{events} \frac{\delta(\int d\phi |M_\alpha|^2 W(p, p^{vis}))}{\int d\phi |M_\alpha|^2 W(p, p^{vis}))} + N(\frac{\delta\sigma_\alpha}{\sigma_\alpha}). \tag{A.2}$$

Moreover the acceptance correction factor induces also an uncertainty on the final result. It is a global correction 100% correlated between the different top mass hypothesis. This systematic uncertainty can be reduced according to a better description of the acceptance and the error component related to the acceptance is not represented on the various likelihood plots. However the effect can be computed varying the acceptance fit parameters in the range fixed by the error on these parameters with respect to the correlation between them.

As far as the top quark mass estimation is concerned, a parametrization has been chosen to fit the likelihood.

$$-ln(L) = \frac{(M_{top} - a)^2}{2b^2} + c \tag{A.3}$$

where a is the top mass at the minimum, b is the width at $min+0.5$ and c is the offset. The estimated top quark mass correspond to a and the error is computed as a quadratic sum of $\sigma_M = \sqrt{\sigma_a^2 + b^2 + \sigma_b^2}$. The table A.1 summarized how the statistical uncertainty vary when the statistic increase.

Table A.1 – Error evolution with increasing of event number. The input value for the top mass is 175 GeV .

Event number	central value	error
50	174.1	3.47
100	174.3	2.6
250	176.05	1.5
500	176.06	1.15

Appendix **B**

Appendix to the Higgs search analysis

B.1 Background normalization

A data driven technique has been used in order to estimate the background contamination. Background normalization is corrected from the theoretical prediction applying a scale factor for each of the Datasets. The ZZ contribution is normalized according to the CMS cross-section Measurement [].

This Background estimation method provides four scales factors that are not independent that means thaht their uncertainties are correlated. This information is contained in the correlation matrix ($\mathcal{C}$) and the covariance matrix ($\mathcal{C}$ov). The covariance matrix informs about how much two random variable change together. Assuming a set of l random variables (x_l), the covariance between two of them Cov_{ik} can be written as:

$$Cov_{ik} = \frac{1}{N}\sum_{j=1}^{N}(x_{ji} - E(x_i))(x_{jk} - E(x_k)) \tag{B.1}$$

and the correlation as:

$$C_{ik} = \frac{\sum_{j=1}^{N}(x_{ji} - E(x_i))(x_{jk} - E(x_k))}{\sqrt{\sum_{j=1}^{N}(x_{ji} - E(x_i))^2}\sqrt{\sum_{j=1}^{N}(x_{jk} - E(x_k))^2}} \tag{B.2}$$

According to the prescription of Sec. (3.2.4) that imposes the same scale factor for both categories for the $t\bar{t}$, Zbx and Zxx processes. Moreover the $Zb\bar{b}$ normalization for events in the more than two jets category is supposed to be the same as for the Zbx.

The uncertainties on the scale factors extracted from the background fit provide a set of four random variables SF_{tt}, SF_{Zbb2}, SF_{Zbx} and SF_{Zxx} that define a not orthogonal basis. Each of theses uncertainties affects the various considered processes. Their relative uncertainties are considered as nuisance parameters; σ_{tt} , σ_{Zbb2}, σ_{Zbx}, σ_{xx}.

In this base the uncertainty can be written using the error operator, $\mathcal{E}$, as:

$$\epsilon_i = \sum_{j=1}^{N} \mathcal{E}_{ij}.SF_j \tag{B.3}$$

$$\begin{pmatrix} \vec{\epsilon_1} & \vec{\epsilon_2} & \vec{\epsilon_3} & \vec{\epsilon_4} \end{pmatrix} = \begin{pmatrix} \sigma_{tt} & 0 & 0 & 0 \\ 0 & \sigma_{Zbb2} & 0 & 0 \\ 0 & 0 & \sigma_{Zbx} & 0 \\ 0 & 0 & 0 & \sigma_{Zxx} \end{pmatrix} \cdot \begin{pmatrix} \vec{SF_{tt}} & \vec{SF_{Zbb2}} & \vec{SF_{Zbx}} & \vec{SF_{Zxx}} \end{pmatrix} \tag{B.4}$$

$\mathcal{E}$ is diagonal, it means that the each uncertainty act only "in a direction" of one SF_j. Although diagonal in a frame where the base vector are not independent. So there are four correlated sources of uncertainties that must be considered, each of them affecting only one process, tt, Zbb_2, Zbx and Zxx.

Uncorrelated uncertainties sources can be obtained by a transformation to get independent error vectors. This transformation must produce a diagonal covariance matrix. The transformation matrix ($\mathcal{T}$) diagonalize the covariance matrix ($\mathcal{C}ov$),

$$\mathcal{C}ov = \left(\begin{array}{ccccc} & \epsilon_1 & \epsilon_2 & \epsilon_3 & \epsilon_4 \\ \epsilon_1 & 0.00570025 & -0.000989216 & -0.00124505 & 0.000599395 \\ \epsilon_2 & -0.000989216 & 0.00567009 & 0.00567009 & -0.00149803 \\ \epsilon_3 & -0.00124505 & 0.00567009 & 0.00567009 & -0.00550685 \\ \epsilon_4 & 0.000599395 & -0.00149803 & -0.00550685 & 0.00872356 \end{array}\right) \tag{B.5}$$

$\mathcal{T}^{-1}\mathcal{C}ov\mathcal{T} = \mathcal{D}$. Where $\mathcal{D}$ is a diagonal matrix with eigenvalues of $\mathcal{C}ov$ on the diagonal.

$$\mathcal{D} = \begin{pmatrix} 0.0150755 & 0 & 0 & 0 \\ 0 & 0.00609784 & 0 & 0 \\ 0 & 0 & 0.00506176 & 0 \\ 0 & 0 & 0 & -0.000985979 \end{pmatrix}. \tag{B.6}$$

The matrix $\mathcal{T}$ is defined as

$$\mathcal{T} = \begin{pmatrix} \vec{E_1} & \vec{E_2} & \vec{E_3} & \vec{E_4} \end{pmatrix} = \begin{pmatrix} 0.161102 & -0.586571 & 0.793239 & 0.0274363 \\ -0.462439 & 0.494196 & 0.478701 & -0.559254 \\ -0.621913 & 0.10289 & 0.176241 & 0.756027 \\ 0.611081 & 0.633339 & 0.3325 & 0.338976 \end{pmatrix}. \tag{B.7}$$

Where $\vec{E_i}$ are the eigenvectors of the covariance matrix. This transformation provide a new basis with the variables $(A; B; C; D)$.

In this new base the error operator $\mathcal{E}$ transforms as $\mathcal{E}' = \mathcal{T}^{-1}\mathcal{E}\mathcal{T}$. And the matrix of the error vectors $(\epsilon' = \epsilon_{\vec{A}}, \epsilon_{\vec{B}}, \epsilon_{\vec{C}}, \epsilon_{\vec{D}})$in the new base are:

$$\epsilon' = \mathcal{E}'. \begin{pmatrix} \vec{A} & \vec{B} & \vec{C} & \vec{D} \end{pmatrix} = \mathcal{T}^{-1}\mathcal{E}\mathcal{T} \begin{pmatrix} \vec{A} & \vec{B} & \vec{C} & \vec{D} \end{pmatrix} \tag{B.8}$$

$$\sigma' = \mathcal{T}^{-1}\mathcal{E}\mathcal{T}\mathcal{T}^{-1}. \begin{pmatrix} S\vec{F}_{tt} & S\vec{F}_{Zbb2} & S\vec{F}_{Zbx} & S\vec{F}_{Zxx} \end{pmatrix} \tag{B.9}$$

$$\sigma' = \mathcal{T}^{-1}\mathcal{E}. \begin{pmatrix} S\vec{F}_{tt} & S\vec{F}_{Zbb2} & S\vec{F}_{Zbx} & S\vec{F}_{Zxx} \end{pmatrix} \tag{B.10}$$

The σ'_i affects the different processes tt, $Zbb2$, Zbx and Zxx according to:

$$\begin{pmatrix} \begin{array}{ccccc} & tt & Zbb2 & Zbx & Zxx \\ UC1 & 0.0125001 & -0.0333795 & -0.0434374 & 0.0584548 \\ UC2 & 0.0450039 & -0.0355122 & -0.00740349 & -0.0583422 \\ UC3 & 0.0592869 & 0.0352985 & 0.012943 & 0.0309364 \\ UC4 & 0.00196901 & -0.039263 & 0.0552606 & 0.030886 \end{array} \end{pmatrix} \tag{B.11}$$

These four uncorrelated sources of uncertainties have been implemented in the different configuration cards used to estimate the confidence level limit. As in the category of events with more than two jets, the process $Zbb2$ does not appear the equivalent process $Zbb3$ is subject to the same fluctuation as the Zbx process.

B.2 Monte-Carlo sample and dataset

The sets of data used in this analysis are

- **ElA**: /DoubleElectron/Run2011A-08Nov2011-v1/AOD
- **ElB**: /DoubleElectron/Run2011B-19Nov2011-v1/AOD
- **MuA**: /DoubleMu/Run2011A-08Nov2011-v1/AOD
- **MuB**: /DoubleMu/Run2011B-19Nov2011-v1/AOD

The MC samples that are used are in Table B.1

Table B.1 – Simulated events samples with their corresponding number of events and cross section.

Process	Dataset	Cross-section	Evt Nbr
$Z \rightarrow ll$ ($M_{ll} > 50$)	`/DYJetsToLL_TuneZ2_M-50_7TeV-madgraph-tauola/` `Fall11-PU_S6_START44_V9B-v1/`	3048	36264432
$Z \rightarrow ll$ ($Pt_{ll} > 100$)	`/DYJetsToLL_pt100_7TeV-madgraph-tauola`	25.1	1137280
$t\bar{t}$	`/TTJets_TuneZ2_7TeV-madgraph-tauola/` Fall11-PU_S6$_{S}TART44_{V}9B - v1/$	157.5	59244088
ZZ	/ZZTuneZ2$_{7}TeV_{p}ythia6tauola/$ `Fall11-PU_S6_START44_V9B-v1/`	6.206	4191045
ZH 115 GeV	`/ZH_ZToLL_HToBB_M-115_7TeV-powheg_herwigpp`	0.0300	1090000
ZH 120 GeV	`/ZH_ZToLL_HToBB_M-120_7TeV-powheg_herwigpp`	0.0242	1090000
ZH 125 GeV	`/ZH_ZToLL_HToBB_M-125_7TeV-powheg_herwigpp`	0.0189	1100000
ZH 130 GeV	`/ZH_ZToLL_HToBB_M-130_7TeV-powheg_herwigpp`	0.0143	1100000
ZH 135 GeV	`/ZH_ZToLL_HToBB_M-135_7TeV-powheg_herwigpp`	0.0103	1096956

B.3 Additional control distributions

This section presents illustrates some results of the chapter 3. First the distribution of the intermediate neural network (MLP), Higgs vs $t\bar{t}$, Higgs vs ZZ and Higgs vs DY, in the region defined to estimate the upper limits. These discriminants have been built using the seven Matrix Element weight of the table 3.14 according to the description of Sec.(3.2.3). The Fig. B.1 B.2 and B.3 represent the intermediate multilayer perceptron. Both category in jet multiplicity and both dielectron and dimuon channels are presented.

Figure B.1 – Comparison of Data-MC at 5.0 fb^{-1} of the neural network discriminant between Z(ll)H($b\bar{b}$) and Drell-Yan+jets. Top: 2 jets category, Bottom: More than 2 jets category. Left: Dielectron channel, Right: Dimuon channel.

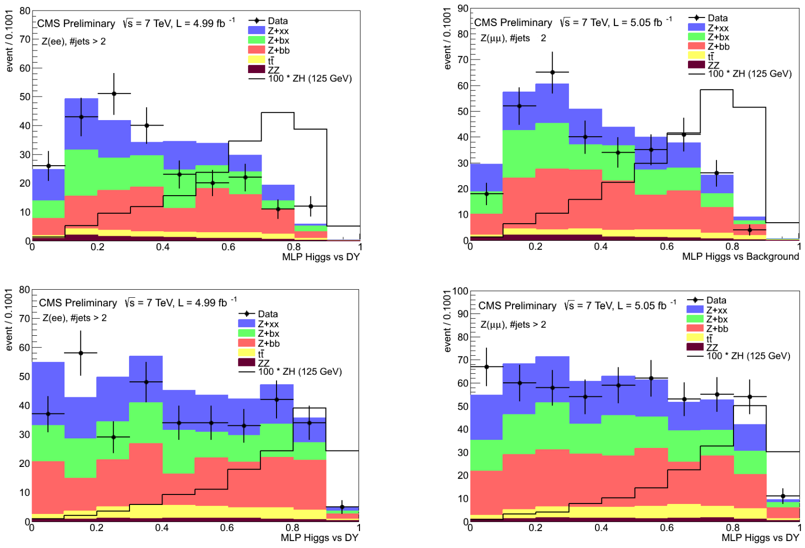

The distributions of the Matrix Element weights estimated according to the seven hypothesis listed in table 3.14 are presented by Fig. B.4 for the dielectron channel.

Figure B.2 – Comparison of Data-MC at 5.0 fb^{-1} of the neural network discriminant between Z(ll)H($b\bar{b}$) and $t\bar{t}$. Top: 2 jets category, Bottom: More than 2 jets category. Left: Dielectron channel, Right: Dimuon channel.

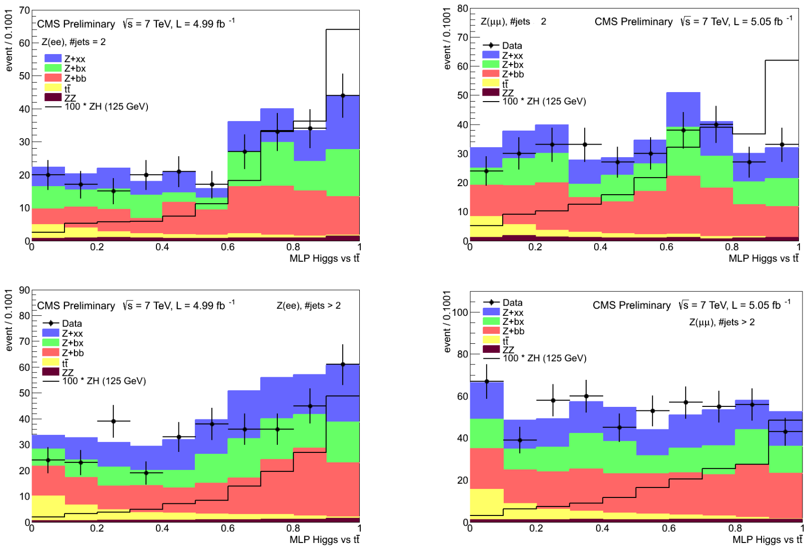

Figure B.3 – Comparison of Data-MC at 5.0 fb^{-1} of the neural network discriminant between Z(ll)H($b\bar{b}$) and Z(ll)Z($b\bar{b}$). Top: 2 jets category, Bottom: More than 2 jets category. Left: Dielectron channel, Right: Dimuon channel.

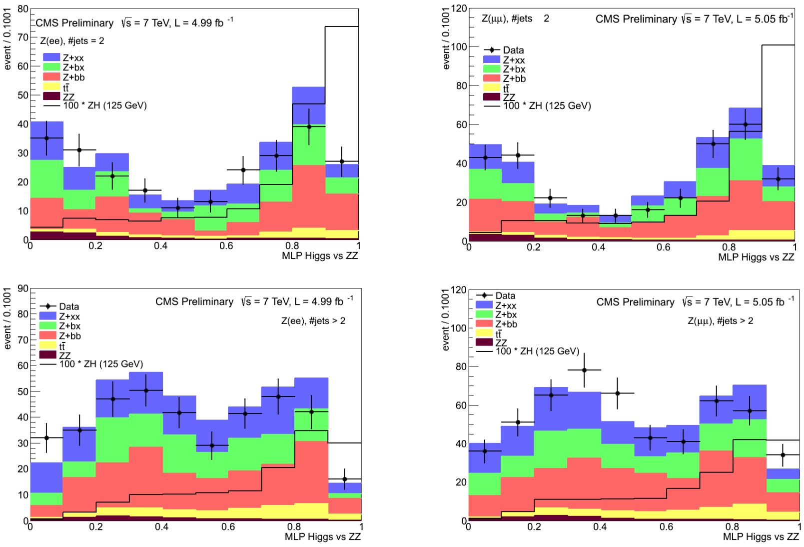

Figure B.4 – Comparison of Data-MC at 5.0 fb^{-1} of the Matrix Element weights distribution for the seven hypothesis of the ZH analysis. Dielectron channel at Z(ll)H($b\bar{b}$) Medium-Loose working point.

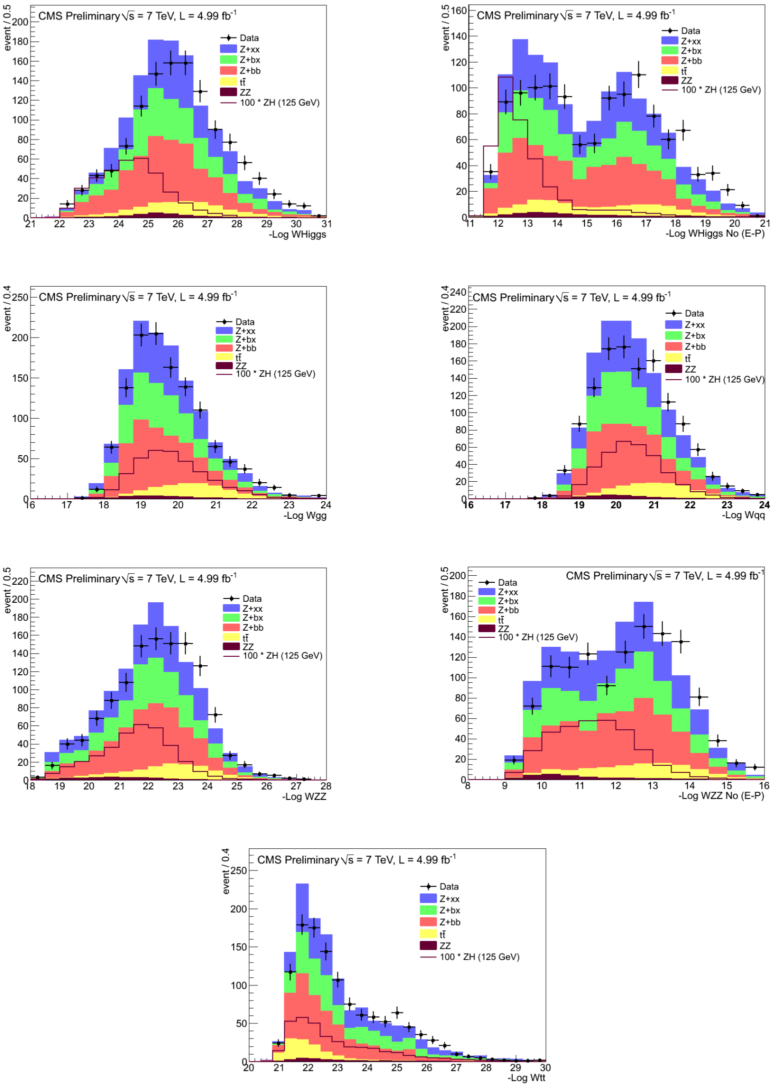

Bibliography

[1] CDF Collaboration. Observation of top quark production in $\bar{p}p$ collisions. *Phys.Rev.Lett.*, 74:2626–2631, 1995.

[2] D0 Collaboration. Observation of the top quark. *Phys.Rev.Lett.*, 74:2632–2637, 1995.

[3] Jyothsna Rani Komaragiri. Measurement of single top production in pp collisions at 7 tev with the cms detector. Technical Report CMS-CR-2011-320. CERN-CMS-CR-2011-320, CERN, Geneva, Nov 2011.

[4] Steven Weinberg. What is an elementary particle? *SLAC Beam Line*, 27N1:17–21, 1999.

[5] K. Kondo. Dynamical likelihood method for recontruction of events with missing momentum. 1: Method and toy models. *J.Phys.Soc.Jap.*, 57:4126–4140, 1988.

[6] CMS Collaboration. The CMS experiment at the CERN LHC. *JINST*, 3:S08004, 2008.

[7] CERN. *ATLAS detector and physics performance: Technical Design Report, 2.* Technical Design Report ATLAS. Geneva, 1999. Electronic version not available.

[8] LHCb Collaboration. Performance of the lhcb detector during the lhc proton runs.

[9] P Cortese, Christian Wolfgang Fabjan, Lodovico Riccati, Karel Safarík, and Hans de Groot. *ALICE physics performance: Technical Design Report.* Technical Design Report ALICE. CERN, Geneva, 2005. revised version submitted on 2006-05-29 15:15:40.

[10] Cottingham W.N. and Greenwood D.A. An introduction to the standard model of particle physics.

[11] Particle Data Group. Review of particle physics. *J.Phys.*, G37:075021, 2010.

[12] R. Keith Ellis, W. James Stirling, and B.R. Webber. QCD and collider physics. *Camb.Monogr.Part.Phys.Nucl.Phys.Cosmol.*, 8:1–435, 1996.

[13] John C. Collins, Davison E. Soper, and George F. Sterman. Factorization of Hard Processes in QCD. *Adv.Ser.Direct.High Energy Phys.*, 5:1–91, 1988.

[14] John C. Collins, Davison E. Soper, and George F. Sterman. Factorization of Hard Processes in QCD. *Adv.Ser.Direct.High Energy Phys.*, 5:1–91, 1988.

[15] Daniel Stump, Joey Huston, Jon Pumplin, Wu-Ki Tung, H.L. Lai, et al. Inclusive jet production, parton distributions, and the search for new physics. *JHEP*, 0310:046, 2003.

[16] Amanda M. Cooper-Sarkar. ZEUS NLO QCD fits. page hep2001/009, 2001.

[17] H1 Collaboration. Measurement of neutral and charged current cross-sections in electron - proton collisions at high Q^2. *Eur.Phys.J.*, C19:269–288, 2001.

[18] D0 Collaboration. High-p_T jets in $\bar{p}p$ collisions at $\sqrt{s} = 630$ GeV and 1800 GeV. *Phys.Rev.*, D64:032003, 2001.

[19] CDF Collaboration. Measurement of the inclusive jet cross section in $\bar{p}p$ collisions at $\sqrt{s} = 1.8$ TeV. *Phys.Rev.*, D64:032001, 2001.

[20] J. Pumplin, D.R. Stump, J. Huston, H.L. Lai, Pavel M. Nadolsky, et al. New generation of parton distributions with uncertainties from global QCD analysis. *JHEP*, 0207:012, 2002.

[21] S.L. Glashow. Partial Symmetries of Weak Interactions. *Nucl.Phys.*, 22:579–588, 1961.

[22] Abdus Salam. Weak and Electromagnetic Interactions. *Conf.Proc.*, C680519:367–377, 1968.

[23] Steven Weinberg. A Model of Leptons. *Phys.Rev.Lett.*, 19:1264–1266, 1967.

[24] Gargamelle Neutrino Collaboration. Observation of Neutrino Like Interactions without Muon or Electron in the Gargamelle Neutrino Experiment. *Nucl.Phys.*, B73:1–22, 1974.

[25] Jeffrey Goldstone, Abdus Salam, and Steven Weinberg. Broken Symmetries. *Phys.Rev.*, 127:965–970, 1962.

[26] UA2 Collaboration. Evidence for Z0 —gt; e+ e- at the CERN anti-p p Collider. *Phys.Lett.*, B129:130–140, 1983.

[27] F. Halzen, Alan D. Martin, and D.M. Scott. IDENTIFICATION OF W BOSONS IN anti-p p COLLISIONS: A DETAILED STUDY. *Phys.Rev.*, D25:754, 1982.

[28] F. Englert and R. Brout. Broken Symmetry and the Mass of Gauge Vector Mesons. *Phys.Rev.Lett.*, 13:321–323, 1964.

[29] Peter W. Higgs. Spontaneous Symmetry Breakdown without Massless Bosons. *Phys.Rev.*, 145:1156–1163, 1966.

[30] G.S. Guralnik, C.R. Hagen, and T.W.B. Kibble. Global Conservation Laws and Massless Particles. *Phys.Rev.Lett.*, 13:585–587, 1964.

[31] DELPHI Collaboration L3 Collaboration OPAL Collaboration LEP Working Group for Higgs boson searches, ALEPH Collaboration. Search for the standard model Higgs boson at LEP. *Phys.Lett.*, B565:61–75, 2003.

[32] D0 Collaboration Tevatron New Physics Higgs Working Group, CDF Collaboration. Updated Combination of CDF and D0 Searches for Standard Model Higgs Boson Production with up to 10.0 fb^{-1} of Data. 2012.

[33] LEP electroweak group. http://lepwwg.web.web.cern.ch/lepewwg.

[34] CMS Collaboration. Observation of a new boson at a mass of 125 GeV with the CMS experiment at the LHC. *Phys.Lett.*, B716:30–61, 2012.

[35] CMS Collaboration. Properties of the higgs-like boson in the decay h to zz to 4l in pp collisions at sqrt s =7 and 8 tev. Technical Report CMS-PAS-HIG-13-002, CERN, Geneva, 2013.

[36] CMS Collaboration. On the mass and spin-parity of the Higgs boson candidate via its decays to Z boson pairs. *Phys.Rev.Lett.*, 110:081803, 2013.

[37] CMS Collaboration. Search for the standard model higgs boson produced in association with w or z bosons, and decaying to bottom quarks. Technical Report CMS-PAS-HIG-13-012, CERN, Geneva, 2013.

[38] LHC Higgs Cross Section Working Group, A. David, A. Denner, M. Duehrssen, M. Grazzini, et al. LHC HXSWG interim recommendations to explore the coupling structure of a Higgs-like particle. 2012.

[39] CMS Collaboration. Combination of standard model higgs boson searches and measurements of the properties of the new boson with a mass near 125 gev. Technical Report CMS-PAS-HIG-13-005, Geneva, 2013.

[40] CMS Collaboration. Search for the standard model Higgs boson produced in association with a top-quark pair in pp collisions at the LHC. *JHEP*, 1305:145, 2013.

[41] CMS Collaboration. Higgs to bb in the vbf channel. Technical Report CMS-PAS-HIG-13-011, Geneva, 2013.

[42] CDF Collaboration. Observation of top quark production in $\bar{p}p$ collisions. *Phys.Rev.Lett.*, 74:2626–2631, 1995.

[43] D0 Collaboration. Observation of the top quark. *Phys.Rev.Lett.*, 74:2632–2637, 1995.

[44] CMS Collaboration. Combination of atlas and cms top-quark pair cross section measurements using proton-proton collisions at sqrt(s) = 7 tev. Technical Report CMS-PAS-TOP-12-003, Geneva, 2013.

[45] CMS Collaboration. First measurement of b(t -> wb)/b(t -> wq) in the dilepton channel in pp collisions at sqrt(s)=7 tev. Technical Report CMS-PAS-TOP-11-029, CERN, Geneva, 2012.

[46] L3 Collaboration OPAL Collaboration LEP Electroweak Working Group ALEPH Collaboration, DELPHI Collaboration. Electroweak Measurements in Electron-Positron Collisions at W-Boson-Pair Energies at LEP. 2013.

[47] Henning Flacher, Martin Goebel, Johannes Haller, Andreas Hocker, Klaus Monig, et al. Revisiting the Global Electroweak Fit of the Standard Model and Beyond with Gfitter. *Eur.Phys.J.*, C60:543–583, 2009.

[48] CMS Collaboration. Measurement of the top-quark mass in $t\bar{t}$ events with lepton+jets final states in pp collisions at $\sqrt{s} = 7$ TeV. *JHEP*, 1212:105, 2012.

[49] CMS Collaboration. Measurement of the top - antitop mass difference in pp collisions at sqrt(s) = 8 tev. Technical Report CMS-PAS-TOP-12-031, Geneva, 2013.

[50] CDF and D0 Collaboration. Combination of CDF and DO results on the mass of the top quark using up to 8.7 $\mathrm{fb}^{-1} at the Tevatron.$ 2013.

[51] CMS Collaboration. *The CMS magnet project: Technical Design Report*. Technical Design Report CMS. CERN, Geneva, 1997.

[52] CMS Collaboration. *The CMS tracker: addendum to the Technical Design Report*. Technical Design Report CMS. CERN, Geneva, 2000.

[53] CMS Collaboration. Tracking and vertexing results from first collisions. Technical Report CMS-PAS-TRK-10-001, CERN, 2010. Geneva, 2010.

[54] Wolfgang Adam, Boris Mangano, Thomas Speer, and Teddy Todorov. Track reconstruction in the cms tracker. Technical Report CMS-NOTE-2006-041, CERN, Geneva, Dec 2006.

[55] CMS Collaboration. Adaptive vertex fitting. Technical Report CMS note 2007/008, R. Fru ¨hwirth, W. Waltenberger, P. Vanlaer, 2008. Geneva, 2008.

[56] Ludwik Dobrzynski. Cms status. Technical Report CMS-CR-2006-044. 2, CERN, Geneva, Aug 2006.

[57] W. Adam, R. Frühwirth, A. Strandlie, and T. Todorov. Reconstruction of Electron Tracks With the Gaussian-Sum Filter. 2003.

[58] CMS Collaboration. Energy calibration and resolution of the cms electromagnetic calorimeter in pp collisions at $\sqrt{s} = 7$ tev. Technical Report arXiv:1306.2016. CMS-EGM-11-001. CERN-PH-EP-2013-097, CERN, Geneva, Jun 2013. Comments: Submitted to JINST.

[59] CMS Collaboration. *The CMS hadron calorimeter project: Technical Design Report*. Technical Design Report CMS. CERN, Geneva, 1997. The following files are from <a href=.

[60] M. Cacciari and G.P. Salam. Pileup subtraction using jet areas. *Physics Letters B*, 659:119–126, 2008.

[61] M. Cacciari, G. Salam, and G. Soyez. The anti-kt jet clustering algorithm. *JHEP*, 04:119–126, 2008.

[62] Esen et. all. Plans for jet energy corrections at cms. Technical Report CMS AN-2007/055, CERN, 2007.

[63] CMS Collaboration. *The CMS muon project: Technical Design Report*. Technical Design Report CMS. CERN, Geneva, 1997.

[64] G. Abbiendi et. all. Muon reconstruction in the cms detector. Technical Report CMS AN-2008/097, CERN, Geneva, Jul 2009.

[65] CMS Collaboration. Performance of CMS muon reconstruction in pp collision events at $\sqrt{s} = 7$ TeV. *JINST*, 7:P10002, 2012.

[66] CMS Collaboration. Particle-flow event reconstruction in cms and performance for jets, taus, and missing et. *CMS Physics Analysis Summary CMS-PAS-PFT-09-001*.

[67] L. Gibbons A. Khukhunaishvilli J.Alexander, F.Blekman. Met significance performance on early cms collision data. Technical Report CMS AN-2010/133, CERN, May 2010.

[68] CMS Collaboration. Algorithms for b jet identification in cms. Technical Report CMS-PAS-BTV-09-001, CERN, 2009. Geneva, Jul 2009.

[69] CMS Collaboration. Commissioning of b-jet identification with pp collisions at sqrt(s) = 7 tev. Technical Report CMS-PAS-BTV-10-001, CERN, 2010. Geneva, 2010.

[70] Bo Li, Keisuke Fujii, and Yuanning Gao. Kalman-filter-based track fitting in non-uniform magnetic field with segment-wise helical track model. 2013.

[71] CMS Collaboration. b-jet identification in the cms experiment. *CMS Physics Analysis Summary CMS-PAS-BTV-11-004*, 2011.

[72] CMS Collaboration. Identification of b-quark jets with the cms experiment. *J. Instrum.*, 8 P04013(arXiv:1211.4462. CMS-BTV-12-001. CERN-PH-EP-2012-262):P04013. 67 p, Nov 2012. Comments: Submitted to the Journal of Instrumentation.

[73] Bayatyan et. all. Cms tridas project: Technical design report, vol 1: The trigger systems. Technical report.

[74] Stephanie Beauceron. The cms high level trigger. Technical Report CMS-CR-2012-355. CERN-CMS-CR-2012-355, CERN, Geneva, Nov 2012.

[75] John Allison, K. Amako, J. Apostolakis, H. Araujo, P.A. Dubois, et al. Geant4 developments and applications. *IEEE Trans.Nucl.Sci.*, 53:270, 2006.

[76]

[77]

[78] Johan Alwall et. all. Madgraph/madevent v4: the new web generation. *Journal of High Energy Physics*, 2007(09):028, 2007.

[79] Johan Alwall, Michel Herquet, Fabio Maltoni, Olivier Mattelaer, and Tim Stelzer. MadGraph 5 : Going Beyond. *JHEP*, 1106:128, 2011.

[80] Michelangelo L. Mangano, Mauro Moretti, Fulvio Piccinini, Roberto Pittau, and Antonio D. Polosa. ALPGEN, a generator for hard multiparton processes in hadronic collisions. *JHEP*, 0307:001, 2003.

[81] T. Gleisberg, Stefan. Hoeche, F. Krauss, M. Schonherr, S. Schumann, et al. Event generation with SHERPA 1.1. *JHEP*, 0902:007, 2009.

[82] Paolo Nason. A New method for combining NLO QCD with shower Monte Carlo algorithms. *JHEP*, 0411:040, 2004.

[83] Johan Alwall, Simon de Visscher, and Fabio Maltoni. QCD radiation in the production of heavy colored particles at the LHC. *JHEP*, 0902:017, 2009.

[84] BrunoMansoulié Jérôme Schwindling. Mlpfit :a tool for designing and using multi-layer perceptrons. *http://schwind.web.cern.ch/schwind/MLPfit/doc/MLPfit.pdf.*

[85] Andreas Hocker, J. Stelzer, F. Tegenfeldt, H. Voss, K. Voss, et al. TMVA - Toolkit for Multivariate Data Analysis. *PoS*, ACAT:040, 2007.

[86] Kevin Alexander Kroeninger. A Measurement of the Top Quark Mass with the D0 Detector at $\sqrt{s} = 1.96$-TeV using the Matrix Element Method. 2004.

[87] T. Aaltonen et al. Combination of CDF and D0 measurements of the W boson helicity in top quark decays. *Phys.Rev.*, D85:071106, 2012.

[88] Paul Avery, Dimitri Bourilkov, Mingshui Chen, Tongguang Cheng, Alexey Drozdetskiy, et al. Precision Studies of the Higgs Golden Channel $H \to ZZ * 4l$. Part I. Kinematic discriminants from leading order matrix elements. *journal*, 2012.

[89] Fabio Maltoni Olivier Mattelaer Pierre Artoisenet, Vincent Lemaitre.

[90] G. P. Lepage. VEGAS : an adaptive multidimensional integration Program. 1980.

[91] CDF Collaboration. Top quark mass measurement from dilepton events at CDF II with the matrix-element method. *Phys. Rev. D*, 74:032009, Aug 2006.

[92] Tevatron Electroweak Working Group. Combination of cdf and do results on the mass of the top quark, 2006.

[93] Jorgen D'Hondt, Steven Lowette, O L Buchmüller, Susanna Cucciarelli, Frank-Peter Schilling, Maria Spiropulu, S Paktinat-Mehdiabadi, Daniele Benedetti, and Luc Pape. Fitting of Event Topologies with External Kinematic Constraints in CMS. Technical Report CMS-NOTE-2006-023, CERN, Geneva, Jan 2006.

[94] CMS Collaboration. Measurement of the $t\bar{t}$ production cross section and the top quark mass in the dilepton channel in pp collisions at $\sqrt{s}$ =7 tev. *J. High Energy Phys.*, 07(arXiv:1105.5661. CMS-TOP-11-002. CERN-PH-EP-2011-055):049. 44 p, May 2011.

[95] CMS Collaboration. First Measurement of the Cross Section for Top-Quark Pair Production in Proton-Proton Collisions at $\sqrt{s} = 7$ TeV. *Phys. Lett. B*, 695(arXiv:1010.5994. CERN-PH-EP-2010-039. CMS-TOP-10-001):424–443 . 26 p, Oct 2010.

[96]

[97] Tim Nelson Harry Nelson. A Guide to Unbinned Maximum Likelihood Fits. *CBX 98-61*, 1998.

[98] Fred JAMES and Matthias WINKLER. MINUIT User's Guide. 2004.

[99] Oram Gedalia, Gino Isidori, Fabio Maltoni, Gilad Perez, Michele Selvaggi, et al. Top B Physics at the LHC. 2012.

[100] J. Alwall, A. Freitas, and O. Mattelaer. The Matrix Element Method and QCD Radiation. *Phys. Rev.*, D83:074010, 2011.

[101] B. Abbott et al. Measurement of the top quark mass using dilepton events. *Phys.Rev.Lett.*, 80:2063–2068, 1998.

[102] A. Pin and O. Mattelaer. Determination of differential cross sections from $t\bar{t}$ fully leptonic, using the matrix element method. *Nuovo Cim.*, C035N3:229–232, 2012.

[103] CDF Collaboration. A Search for resonant production of $t\bar{t}$ pairs in4.8 fb^{-1} of integrated luminosity of $p\bar{p}$ collisions at $\sqrt{s} = 1.96$ TeV. *Phys.Rev.*, D84:072004, 2011.

[104] S. Ovyn, X. Rouby, and V. Lemaitre. DELPHES, a framework for fast simulation of a generic collider experiment. 2009.

[105] Rikkert Frederix and Fabio Maltoni. Top pair invariant mass distribution: A Window on new physics. *JHEP*, 0901:047, 2009.

[106] CMS Collaboration. Search for a standard model Higgs bosons decaying to tau pairs in pp collisions. Technical Report CMS-PAS-HIG-12-018, CERN, Geneva, 2012.

[107] CMS Collaboration. Higgs to bb in the vbf channel. Technical Report CMS-PAS-HIG-13-011, CERN, Geneva, 2013.

[108] CMS Collaboration. Standard model cross section. Technical report, 2012.

[109] S. Dittmaier et al. Handbook of LHC Higgs Cross Sections: 1. Inclusive Observables. 2011.

[110] Measurement of the Z/gamma* + bb-jets cross section in pp collisions at sqrt(s) = 7 TeV. Technical Report CMS-PAS-SMP-13-004, CERN, Geneva, 2013.

[111] Electron reconstruction and identification at sqrt(s) = 7 tev. Technical Report CMS-PAS-EGM-10-004, CERN, Geneva, 2010.

[112] CMS Collaboration. Measurements of Inclusive W and Z Cross Sections in pp Collisions at $\sqrt{s} = 7$ TeV. *JHEP*, 1101:080, 2011.

[113] CMS Collaboration. Performance of the b-jet identification in cms. Technical Report CMS-PAS-BTV-11-001, CERN, Geneva, 2011.

[114] CMS Collaboration. Measurement of the ZZ production cross section and search for anomalous couplings in 2 l2l ' final states in pp collisions at $\sqrt{s} = 7$ TeV. *JHEP*, 1301:063, 2013.

[115] Fabio Maltoni, Giovanni Ridolfi, and Maria Ubiali. b-initiated processes at the LHC: a reappraisal. *JHEP*, 1207:022, 2012.

[116] aMC@NLO project. `http://amcatnlo.web.cern.ch/amcatnlo/`.

[117] Rikkert Frederix, Stefano Frixione, Valentin Hirschi, Fabio Maltoni, Roberto Pittau, et al. W and $Z/\gamma*$ boson production in association with a bottom-antibottom pair. *JHEP*, 1109:061, 2011.

[118] Kyle Cranmer and Tilman Plehn. Maximum significance at the LHC and Higgs decays to muons. *Eur.Phys.J.*, C51:415–420, 2007.

[119] Stephen A. Vavasis. A New secant method for unconstrained optimization. 2008.

[120] Brieuc FRANCOIS. Méthode des éléments de matrice à l'ordre alpha$_{s}pourlarecherchedubosondeHiggsauLHC"institution = .Technicalreport.$

[121] Glen Cowan, Kyle Cranmer, Eilam Gross, and Ofer Vitells. Asymptotic formulae for likelihood-based tests of new physics. *Eur.Phys.J.*, C71:1554, 2011.

[122] CMS Collaboration. Search for the standard model higgs boson produced in association with w or z bosons, and decaying to bottom quarks for ichep 2012. Technical Report CMS-PAS-HIG-12-019, CERN, Geneva, 2012.